An investigation into the geomorphology of the Hebron Fault, Namibia, using a satellite-derived, high-resolution digital elevation model (DEM)

Guy Salomon

SLMGUY001

A dissertation submitted for the fulfilment of the degree of

Master of Science

Department of Geological Sciences

University of Cape Town

South Africa

August 2019

Supervisor: Alastair Sloan

Declaration

I, Guy Salomon (student number: SLMGUY001), know the meaning of plagiarism and declare that all of the work in this dissertation, save for that which is properly acknowledged, is my own. Furthermore, this work nor any part of it, has been, is being or will be submitted for another degree in this, or any other university.

I empower the university to reproduce for the purpose of research, either the whole or any portion of the contents.

Signature:

Date: 26 August 2019

Acknowledgements

I would like to acknowledge the funding received in support of this research from the National Research Foundation of South Africa (grant numbers: 110780 and 118831). Additionally, a small grant from the COMET group, funded by the Natural Environmental Research Council (NERC) made the acquisition of satellite imagery possible.

I would like to thank my research supervisor, Dr Alastair Sloan, for his constant encouragement, guidance and support. I am very grateful for his enthusiasm, constructive feedback and for the multiple opportunities that he made available to me. Thank you Alastair.

Additional thanks go to Julian Smit, who helped explain photogrammetric principles and standard practices. Finally, I would like to thank Robert Muir for having the foresight to bring reading material to the field, for the benefit of everyone.

Abstract

The Hebron fault scarp in southern Namibia is 45 km in length with an average height of 5.5 m and a maximum height of 8.9 m. Namibia is a Stable Continental Region (SCR) — a slowly deforming area within a continental plate. The country also has little recorded seismicity with the largest earthquake on the International Seismological Center (ISC) catalogue being M_W 5.4. If the Hebron fault scarp was formed in a single event, this would represent a M_W 7.3 earthquake. SCRs do occasionally experience large earthquakes, however, the recurrence intervals between these events is much larger than in rapidly deforming areas. Consequently, studying palaeo-earthquakes allows the record of seismicity to be extended and the characteristics of SCR events to be better understood. These studies may help refine the M_{max} estimates required for seismic hazard assessment. Previous work on Hebron has been limited to field descriptions and theodolite survey scarp heights. Furthermore, there have been several interpretations of the fault mechanism and number of rupture events. This study produces a high-resolution Digital Elevation Model (DEM) via stereophotogrammetry using pan-sharpened Worldview-3 satellite imagery (0.31 m resolution). The DEM was used for several geomorphological analyses. These included measuring the scarp height at 160 locations along its length, measuring river channel displacements and identifying knickpoints along river profiles. Results indicate that the scarp formed from a normal, dip-slip fault that ruptured in a single event. This scenario would imply a high slip-to-length ratio. A comparison of other SCR fault scarps in the literature was made which shows that Hebrons' slip-to-length ratio falls within the values found on other SCR faults. This study also discusses the implications of results for seismic hazard assessment in the region. Due a poor seismic record, probabilistic seismic hazard analysis (PSHA) will calculate a low seismic risk for Namibia. As large earthquakes can occur in SCRs, deterministic seismic hazard analysis (DSHA) can be used to inform policy makers of the worst case scenarios.

Contents

List of Figures

Introduction

1.1 Tectonic geomorphology

Tectonic geomorphology is the study of how the shape of the landscape is affected by tectonic processes. In regions of dip-slip faulting, tectonic movements usually work to increase relief, building topography, while surface processes such as weathering and erosion wear down the landscape (Burbank and Anderson, 2012). This can occur on several scales, both spatially and temporally. At the global scale, collision of tectonic plates build mountain ranges over millions of years. Conversely, a several-meter-high fault scarp may be formed as the result of a single earthquake in under a minute. New methods allow landscapes to be quantitatively studied. For example, sub-meter-scale DEMs allow fault scarps to be measured in greater detail than ever before (Bi et al., 2018). In addition, modern geodetic instruments can measure position to within a millimeter (Burbank and Anderson, 2012).

1.1.1 Increasing the seismic record

Earthquakes pose a significant risk to people and it is because of this that large earthquakes have been documented for a considerable portion of human history. The first seismograph, a device used to determine which direction seismic waves originated from, was made in China as early as 132 A.D.. The first compilation of earthquakes, analogous to modern day earthquake catalogs, was created circa 887 AD in Japan (Matsu'ura, 2017). The bulk of these records contain only descriptions of the damage caused. This description of damage led to the formation of the Rossi-Forel and ultimately the Mercalli scales (Wood and Neumann, 1931). However, the length of such historical catalogues varies considerably according to geographical

location. Highly populated areas with large amounts of seismicity, such as Japan, are the best documented while areas with lower populations or seismicity may have sparsely populated or even empty records. Namibia is one such place, with no systematic historical catalogue. Today, there are several compilations of earthquakes from different sources around the globe. Most of these began in the middle of the twentieth century. The International Seismological Center (ISC) has a record of earthquakes from 1964 until the present day International Seismological Centre (2016). These instrumental records provide much more detail into the characteristics of individual earthquakes, with information about earthquake parameters such as the depth of rupture and magnitude. Instrumental catalogs only cover about 50 years of global seismicity.

By studying and measuring the height and length of fault scarps in the landscape, looking for evidence of the size and number of ruptures that formed the fault scarp, the size of the events can be estimated. This is done according to the equation:

$$M_0 = \mu W L s \tag{1.1}$$

where μ is the shear modulus, W and L are the width and length of the rupture area and s is the average slip on that area. If a fault has ruptured to the surface, the slip can be estimated from both the height of the fault scarp as well as the displacement of features horizontally. The width can be calculated by making use of the seismic thickness in the area and an approximate value for the dip of the fault. This is particularly useful to investigate earthquakes for which we do not have an instrumental record (Abdrakhmatov et al., 2016; Bi et al., 2018). Studies of tectonic geomorphology can also investigate the timing of pre-historic earthquakes making use of the history of slip on a particular fault, thus increasing the record of seismicity in the area and constraining the recurrence rate of that fault (Ainscoe et al., 2019; Talebian et al., 2016). The ability to construct large-scale, high-resolution DEMs allows fault scarps to be measured in much greater detail than before. These types of studies also allow the seismic record to be extended to beyond the last 50 years for which we have an instrumental record, as well as beyond the last few hundred years of the historical record.

This is particularly useful in Stable Continental Regions (SCRs) as the faults in these areas tend to have recurrence intervals for large earthquakes of thousands to tens of thousands of years (Calais et al., 2016). Thus the instrumental record only covers a fraction of a single fault's recurrence period, as such, the maximum magnitude event predicted from the instrumental catalog would likely be significantly smaller than the largest possible earthquake that the region could produce.

1.1.2 DEMs in tectonic geomorphology

Satellite Photogrammetry

Satellite photogrammetry is well suited for studying large earthquake scarps. This is because of the scale of the areas of interest. Large faults can extend from 50 km to over 100 km (Abdrakhmatov et al., 2016). A single pass by a satellite can collect over 3000 km^2 of stereoscopic imagery. Thus data acquisition of large areas is highly efficient and, given the ability of a satellite to return to the same location in under a week and more recently a single day (Appendix A). There are several commercially available satellites that all can provide sub-meter resolution imagery (Tsanis et al., 2014). Ainscoe et al. (2019) used Pleiades imagery to map and measure the Suusamyr Fault in the Kyrgz Tien Shan in order to reconstruct the Holocene earthquake record and rupture behavior on the fault. Similarly, Bi et al. (2018) used GeoEye-1 imagery to produce a DEM in order to measure the height and provide insight into the recurrence rate of the South Heli Shan Fault in north eastern Tibet.

The launch of several satellites that are capable of capturing very high resolution (VHR), sub-meter pixel size imagery (Tsanis et al., 2014), has enabled the production of high-resolution DEMs on a regional scale. The first of these satellites was IKONOS which launched in 1999 with a panchromatic resolution of 0.82 m at nadir (Hashim and Deilami, 2011). There are now a range of other commercially available VHR satellites, including but not limited to: Quickbird, GeoEye-1, Worldview-3 and Worldview-4 (Bi et al., 2018). There is a large market for stereoscopic satellite

imagery which is now being used to produce DEMs and update maps (Hashim and Deilami, 2011). The quality of the DEMs produced increases with the resolution of the imagery. WorldView-3 was launched in late 2014, making it one of the more recent VHR satellites, with a panchromatic resolution of 0.31 m (Barazzetti et al., 2016).

Other methods of obtaining topography

Another commonly used method for digital topography is Light Detection and Ranging (LiDAR). LiDAR instruments send out a pulse of light using a laser, the time for the light to reach the target and return is measured. The travel time is then used to calculate the distance from the instrument to the object (Dubayah and Drake, 2000). This method can be done in a fixed place (terrestrial) or with the instrument mounted onto a plane or UAV (airborne). Airborne LiDAR surveys can produce point-clouds of >10 points per square meter (Johnson et al., 2014). However, there are significant expenses associated with LiDAR surveys . In particular, airborne surveys can cost several thousands of dollars per square kilometer (Johnson et al., 2014; Dubayah and Drake, 2000). An advantage offered by LiDAR is the ability to classify the returns of the laser pulse (Baltsavias, 1999). This allows for the identification of man-made features and vegetation. Furthermore, these features can be removed from the DEM such that the final DEM corresponds to only the surface of the ground as if the vegetation had been removed (Baltsavias, 1999). This function has led to LiDAR surveys being used in forestry applications, measuring the volume of the canopy as well as the biomass above the ground (Dubayah and Drake, 2000). LiDAR acquisitions are thus useful when studying faults in areas where vegetation may obscure parts of the fault scarp.

Digital cameras attached to UAVs such as drones and balloons have also been used to collect imagery for smaller scale DEMs (Johnson et al., 2014). In general, these photogrammetric techniques are significantly cheaper than LiDAR and can be scaled up to regional studies with significantly less cost. Furthermore, the quality and resolution of the DEMs obtained are on-par with those produced using LiDAR (Westoby et al., 2012). However, these techniques are not able to automatically

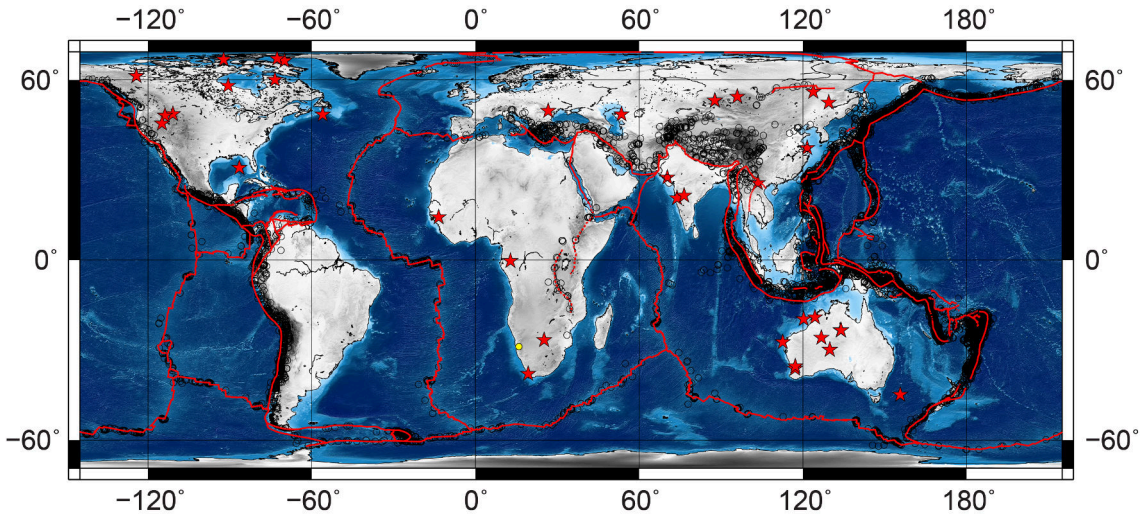

Figure 1.1: Global map of earthquakes of $M_W > 6$ between 1900 and 2016 from the ISC (International Seismological Centre, 2016). Note that the majority of global seismicity occurs near the tectonic plate boundaries (red lines). Red stars mark stable continental region earthquakes (Calais et al., 2016). The location of Hebron has been marked with a yellow circle.

classify and remove the vegetation on top of the ground surface like LiDAR.

1.2 Stable Continental Regions

The majority of seismic activity occurs at the boundaries of tectonic plates (Fig. 1.1). The earthquakes that occur in these areas are referred to as inter-plate earthquakes. However, earthquakes also occur within tectonic plates, these are referred to as intra-plate events. Inter-plate events occur more frequently and thus have been the focus of most research. Intra-plate events, while less frequent, can still represent large earthquakes which pose a direct risk to billions of people, particularly in densely populated countries, such as China and India.

The precise definition of an intra-plate event is somewhat debateable. There is a continuum between areas where a single fault system takes up virtually all the plate motion, as might be seen in a subduction zone, through to regions where relative plate motion is taken up by a number of faults over a broad area, as is often seen in many continental collision zones (Johnston and Kanter, 1990). Then there are the interiors of continental tectonic plates which experience very low strain rates, less than 10^{-9}, as a result of stress transmitted from plate boundaries (Johnston

and Kanter, 1990). These areas have been termed SCRs (Calais et al., 2016; Clark et al., 2012; Johnston and Kanter, 1990). Despite their low strain rates, large and potentially damaging earthquakes have been known to occur in SCRs. The 2001 Bhuj earthquake is one such example, a Mw 7.7 quake that killed 20 000 people, displaced 600 000 and caused 4 billion dollars in damages (Maurer and Oblitas, 2001; Singh et al., 2002).

The typical earthquake model involves elastic strain accumulating across the fault plane until the frictional stresses on the fault are overcome and the fault ruptures, causing an earthquake (Brace and Byerlee, 1966). The time that it takes for sufficient elastic strain to accumulate, and thus the time between earthquakes on that fault, is called the recurrence interval (Molnar, 1979). As such, this can be used to estimate when the next earthquake on a particular fault can be expected (although repeat time can vary significantly between successive events on the same fault segment). In rapidly deforming areas such as Japan, the recurrence intervals between large earthquakes are relatively well known, due to good instrumentation as well as a record that covers several of these cycles (Molnar, 1979). In the case of SCRs, the very slow strain accumulation rates mean that the recurrence period between large earthquakes is much longer than for inter-plate events, ranging from thousands to tens of thousands of years (Calais et al., 2016; Molnar, 1979). Furthermore, the seismic record for the area may only be on the order of a hundred years, meaning that the recurrence period of faults in the region may not be discernible from the record. Thus studying ancient fault scarps, such as Hebron, can be used to extend the seismic record in the area and determine the recurrence period of large earthquakes in order for better seismic hazard assessment.

1.3 The Hebron fault

The Hebron fault is marked by a 45 km long fault scarp, located SE of the small Namibian town of Sesriem. This is located centrally on the African tectonic plate in a region with very low strain rates with an upper bound on horizontal strain of 0.6 - 1 mm/yr determined by Saria et al. (2013). Thus Hebron, as well as Namibia and

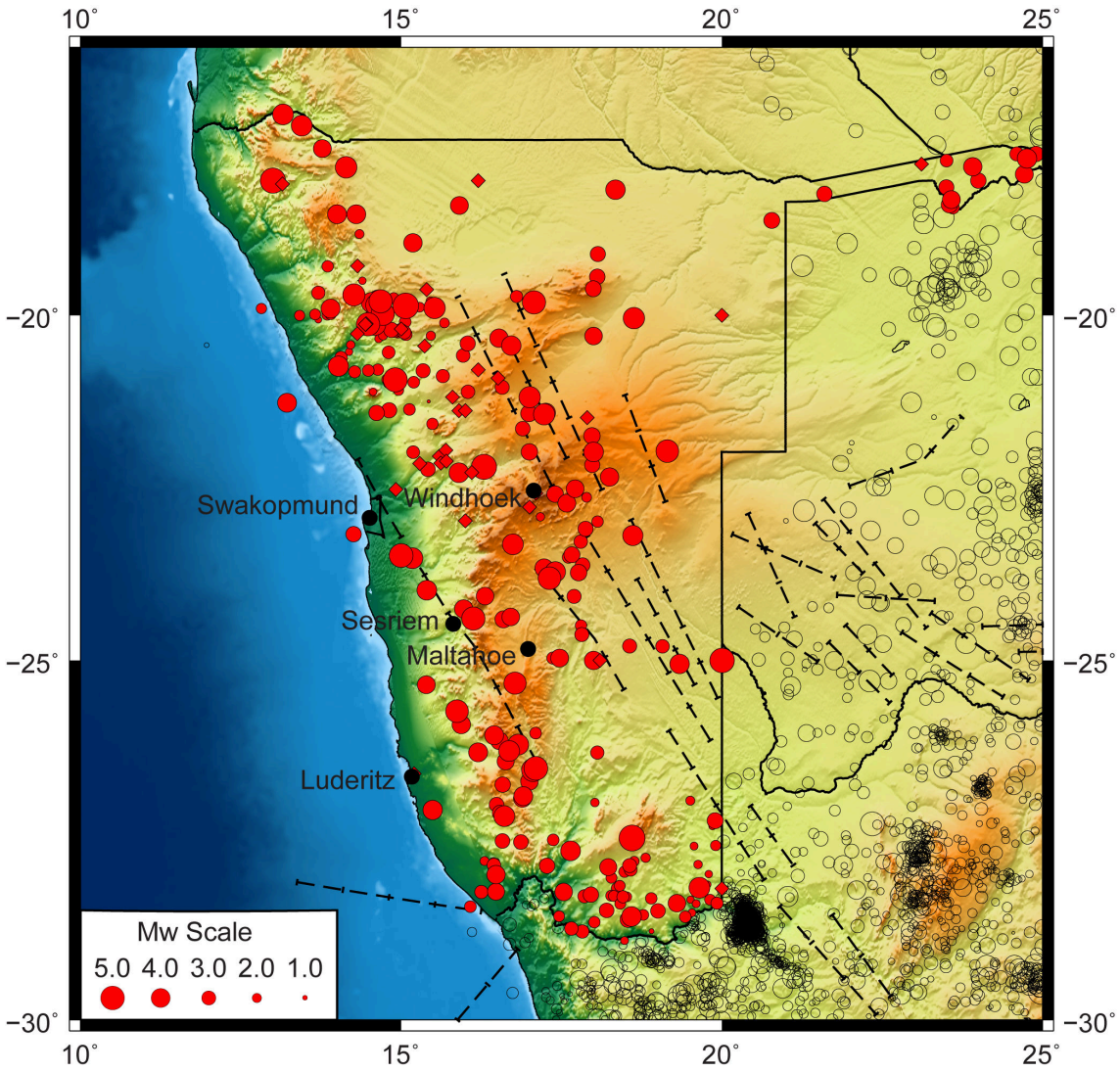

Figure 1.2: Seismicity in Namibia, the red circles represent earthquakes in Namibia from 1964 until present with known magnitudes and the diamonds are earthquakes without magnitudes (International Seismological Centre, 2016; Manzunzu et al., 2019). The dashed lines are lineaments and structures as per Andreoli et al. (1996). The Hebron fault is located along the lineament to the SE of the town of Sesriem. The empty circles represent southern African earthquakes outside of Namibia (International Seismological Centre, 2016). Note, the apparent increase in seismicity across the border may in part be due to better instrumentation (and a lower completeness threshold) in South Africa.

much of southern Africa, falls within a SCR (Manzunzu et al., 2019). The fault scarp trends NW-SE with heights reaching up to 8.9 m. The scarp runs parallel to the Great Escarpment as well as the coastline. This is in-line with structural lineaments mapped by Andreoli et al. (1996) that run through structures along the same trend (Fig. 1.2). In particular the Dreylingen fault is a 100 km fault located with the same strike to the SW of Hebron (Viola et al., 2005) and comprising the rest of the

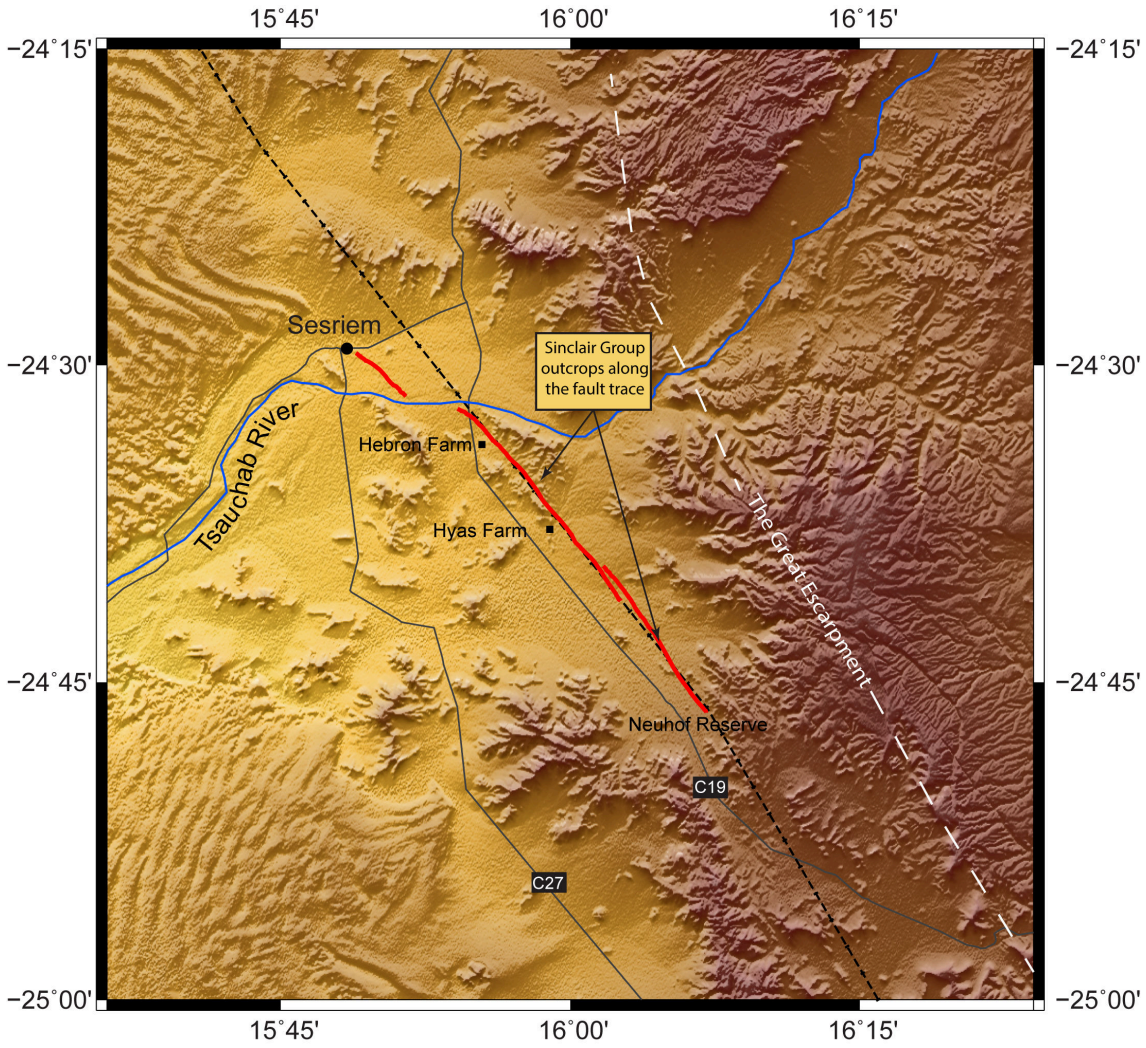

Figure 1.3: Map of the Hebron Fault, dashed lines are lineaments as mapped by (Andreoli et al., 1996). The fault is highlighted in red, is comprised of three segments with right-stepping geometry (Viola et al., 2005) and runs parallel to one of those lineaments.

Kuiseb-Hebron fault structure as described by Andreoli et al. (1996). North east of Sesriem, another fault has been mapped, the Elim Fault. However, our fieldwork suggests that Elim is a hydrological feature with no fault scarp. If the Hebron fault was formed during a single rupture, then it would represent an earthquake of M_w >7, this is significantly larger than the largest event on the instrumental record for Namibia of M_w 5.6. Constraining the maximum magnitude an area can experience is an important input for seismic hazard analysis. A difference of more than an order of magnitude would greatly affect any hazard map that may be produced.

1.3.1 Geological Setting

The predominant units that the fault runs through are the middle Pliocene Karpfenkliff Conglomerate Formation and the capping Kamberg Calcrete Formation (White et al., 2009). The lithology of the clasts within the Karpfenkliff include rounded cobbles of laminated dolerites, limestones and sandstones from the Kuibis and Schwarzrand subgroups of the Nama Group. The Nama Group is a Neoproterozoic to early Cambrian (570 - 543 Ma) foreland basin fill (Cohen et al., 2009) that is exposed on the nearby Great Escarpment. The Karpfenkliff also has clasts of the crystalline Sinclair Sequence (1216 Ma) which forms the basement rock in the area (Hoal and Heaman, 1995). This group is a volcanic-sedimentary succession comprised of rhyolites, quartz porphyry, granitoids and quartzites. The fault also runs through two outcrops of this basement, the first between the Hebron and Hyas farms and the second in the form of an inselberg on the Neuhof reserve (Fig. 1.3). The sands of the Namib Sand Sea, the Sossus Sand Formation, to the west of the Sesriem have been dated to be late Pleistocene in age (White et al., 2009).

1.3.2 Previous studies

The Hebron fault was first interpreted by Viola et al. (2005) as a 40 km long dextral transtensional fault which, included with the Dreylingen fault, forms an extensional structure running NW-SE across southern Namibia. The interpretation of the dextral transtensional mechanism of the fault was due to observed right-lateral offsets in alluvial fans crossing the fault and several scarp sections arranged in a right-stepping en-echelon geometry. Furthermore, due to good preservation of the scarp and the weathering characteristics of the alluvial and fluvial units that comprise it, a Pleistocene age was proposed.

More recently, White et al. (2009) conducted a field study of the Hebron scarp whereby the scarp height was measured using theodolite surveying techniques at 10 locations along its length and descriptions were made of the offset geological units. From their descriptions and measurements of the scarp heights, White et al. (2009) split the morphology of the scarp into three scarp types.

This scarp types include the "juvenile" scarp, with fresh sub-vertical faces (60-80°) in highly calcretized conglomerate with some boulder debris on the footwall, but not a significant wedge of debris material. The second scarp type,"intermediate" exhibits a rounded crest and more material accumulated at the base of the scarp. These segments have a lower slope angle of 20-50°. The third scarp, "mature", is much more diffuse with slope angles of 15± 2° (White et al., 2009). Additionally, the height of the scarp was calculated to be 4.5 m in average and no geomorphological evidence was found for horizontal movement on the fault plane (White et al., 2009).

The scarp was thus interpreted as a normal fault with no strike-slip component. Furthermore, the height of the scarp was interpreted to be the cumulative result of several earthquakes. This was because the slip-to-length ratio, $2x10^{-4}$, that would be implied for a single event is unusually high compared to the generally used slip-to-length ratio for fault ruptures of $5x10^{-5}$ (Wells and Coppersmith, 1994). White et al. (2009) further constrained the timing the most recent activation of the fault to be within the Late Pleistocene to modern era. This age was due to offsets visible in the dunes north of Sesriem, and in line with the fault lineation. These dunes are currently inactive and form a part of the Sossus Sand Formation which have been found to be covering Middle Stone Age artifacts (Vogelsang, 1998) thus post-dating the Middle Stone Age (White et al., 2009). The Middle Stone Age in Southern Africa is generally considered to be *c.* 40 - 200 ka (late Pleistocene) (Mitchell, 2002).

1.4 Aims and Objectives

The principle aims of this study was to measure the amount and distribution of slip on the fault, the mechanism and how many events were responsible for the formation of the fault scarp. This was achieved by producing a DEM upon which geomorphological measurements could be made, allowing the fault scarp to be measured in greater detail than before.

High-resolution stereoscopic Worldview-3 satellite imagery was acquired and was

used to produce a sub-1 m resolution DEM of the fault scarp. Using this DEM, the scarp height was measured at 160 locations along the scarp to determine the total amount of vertical offset on the fault. Offset in stream channels was measured for horizontal offsets and strike-slip motion, as observed by (Viola et al., 2005). The mechanism of the fault can thus be determined from the observed distribution and direction of slip.

Additionally, further geomorphological analyses are conducted in order to determine whether the fault scarp was generated in a single earthquake or as a result of multiple events. These analyses include knickpoint analysis along longitudinal profiles of rivers that cross the fault scarp as well as categorization of scarp morphologies in relation to lithology. The dip of the fault was also calculated using offsets visible in the imagery and field observations.

Furthermore, seismic data collected from a passive seismic deployment at the Hebron fault by Kahle (2017) was used in order to determine the dip of the fault below the surface. A scenario of the maximum magnitude earthquake that Hebron could support was modelled and used to update the seismic hazard for the region.

Methodology

2.1 Photogrammetry

Photogrammetry is defined as the science and art of measuring objects using photographs (Wolf et al., 2000; Methley, 1986). This is an old technique, with the term "Photogrammetry" being coined in 1867 by the German geographers, Otto Kersten and Albrecht Meydenbauer (Grimm, 2007). By the end of the 19th century, photogrammetry was an established technique, with Laussedat (1898) being one of the first works describing the method (Ghosh, 1981).

While photogrammetry is now used in a plethora of fields, the primary historical use of this method was for topographical mapping (Wolf et al., 2000). Topographic maps have been replaced as the primary output of photogrammetry by newer photogrammetric products, namely orthophotos and digital elevation models (DEMs). These newer products allow systematic and automated analyses to be made, which are particularly useful for studies of tectonic geomorphology. Orthophotos are either aerial photographs or satellite images which have been modified to have a constant scale throughout the image. A DEM is an array of points for an area for which the x,y (longitude and latitude) and z (altitude) co-ordinates have been determined (Wolf et al., 2000).

One aim of this study was to produce a DEM from stereoscopic satellite imagery. Figure 2.1 outlines the workflow of this DEM generation. A minimum of two images, taken from separate locations are required. The Worldview-3 imagery is already geolocated and ortho-rectified. After any further processing of the images, such as histogram equalization to improve image contrast, a photogrammetric project is

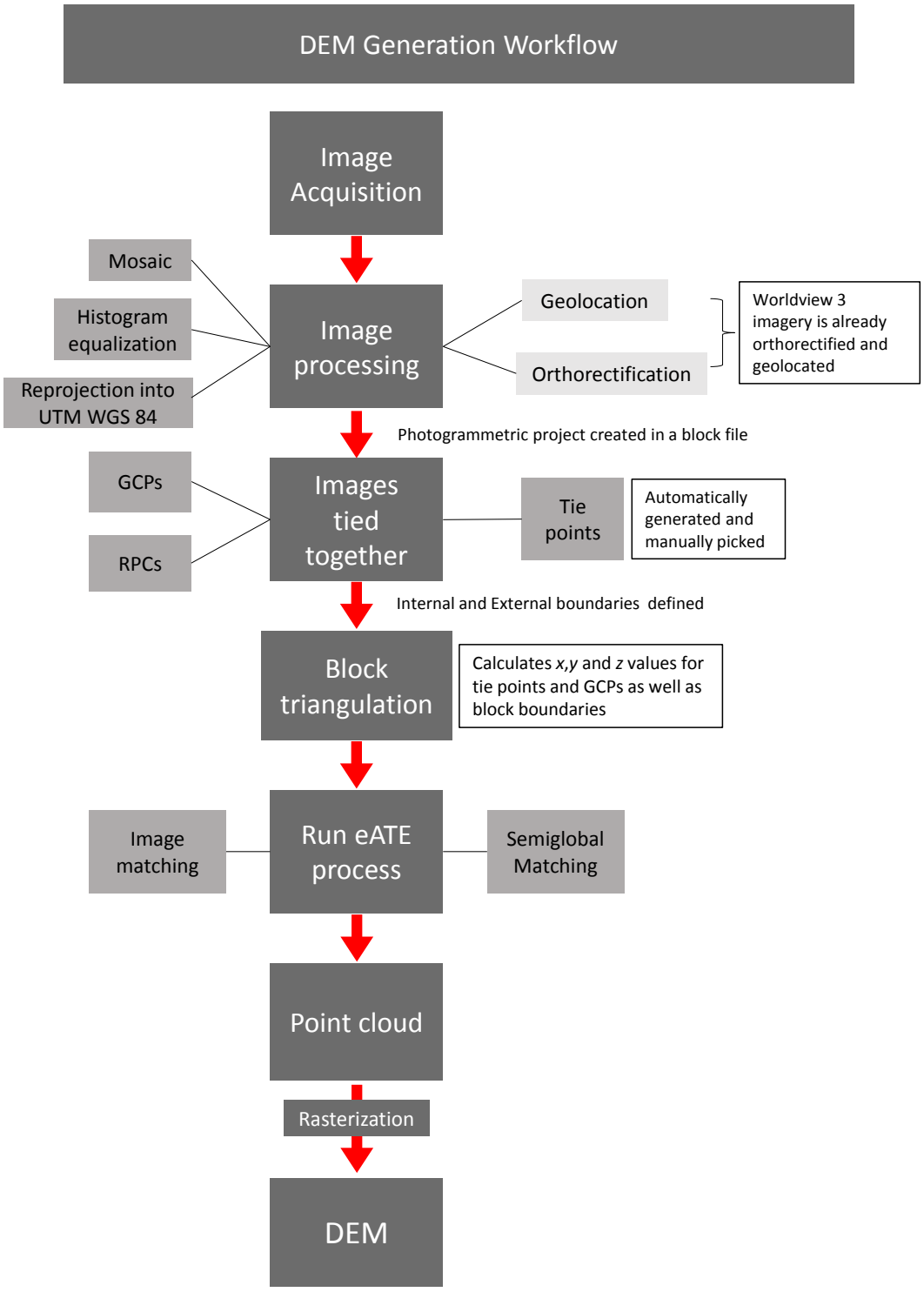

Figure 2.1: Workflow for DEM creation using Worldview 3 imagery and the ERDAS Imagine Photogrammetry Suite

created in a .block file within ERDAS Imagine. The internal and external image orientations are loaded by adding the Rational Polynomial Coefficients (RPCs) that are provided with the satellite images. The images are then aligned using a pattern finding algorithm which ties the images together with common points, or "tie points". Ground control points (GCPs) are added in order to ensure global accuracy of the final DEM. In the case that not enough points are found automatically (ERDAS recommends a minimum of 25), tie points are manually selected. The block triangulation is run which calculates the ground x,y and z values for each of the tie points. The enhanced Automatic Terrain Extraction (eATE) algorithm is run which uses image matching and semi-global matching to perform a pixel-by-pixel interrogation of the imagery and produce a dense point cloud. This point cloud is then rasterized to produce the DEM used in the following geomorphological analyses. Further details about the individual steps taken for the DEM can be found in Sections 2.1.1, 2.1.2, 2.1.3 and 2.1.4.

2.1.1 Stereophotogrammetry

Stereophotogrammetry falls within the metric branch of photogrammetry which involves the precise measurement of distance, angles, areas, volumes, sizes and shapes of objects (Wolf et al., 2000). In particular, stereophotogrammetry is used to estimate the three dimensional co-ordinates of objects from two or more images that have been taken from different (unique) locations.

Stereoscopy and triangulation

A single image is merely a projection of a 3D scene onto a 2D plane. In order to see objects in 3D, at least two images are needed. This concept is known as stereoscopy (Waack, 1985) and this is how humans perceive depth using their eyes (Figure 2.2a). When two different images of a scene are available (Figure 2.2b) then the position of a 3D point within the scene can be calculated as the intersection of the two projection rays. One ray from the corresponding point on each image. The location of the camera has to be known for each image. This process is known as triangulation (Hartley and Zisserman, 2003) and is the basic method of obtaining x,y and z co-ordinates from imagery. The geometry of the camera has to be known

in order for triangulation to be accurate. One important measure is the focal length of the camera (Fig. 2.3). This is the length from the lens to the focal point, which is the point where the light rays converge.

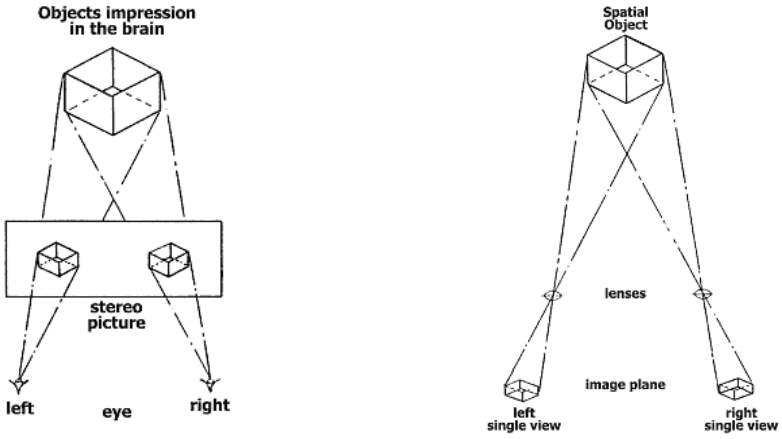

(a) How our eyes perceive 3D objects (b) Stereo images of an object

Figure 2.2: Comparison between (a) how our eyes obtain information about an object, such as the dimensions and position of the object relative to us by viewing objects in stereo. (b) Stereo images that can be used to produce a sense of perspective. (Waack, 1985)

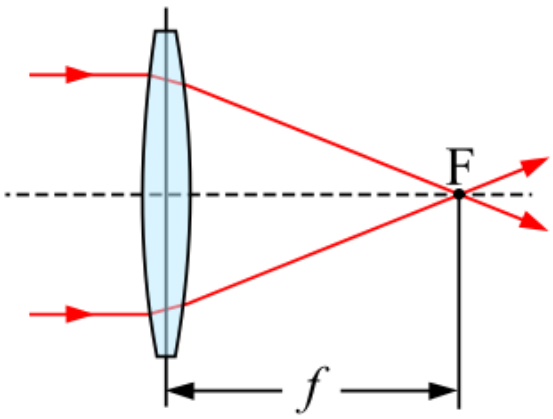

Figure 2.3: Diagram of light passing through a concave lens. The focal length (f) is the distance between the lens and focal point (F). Adapted from (Henrik)

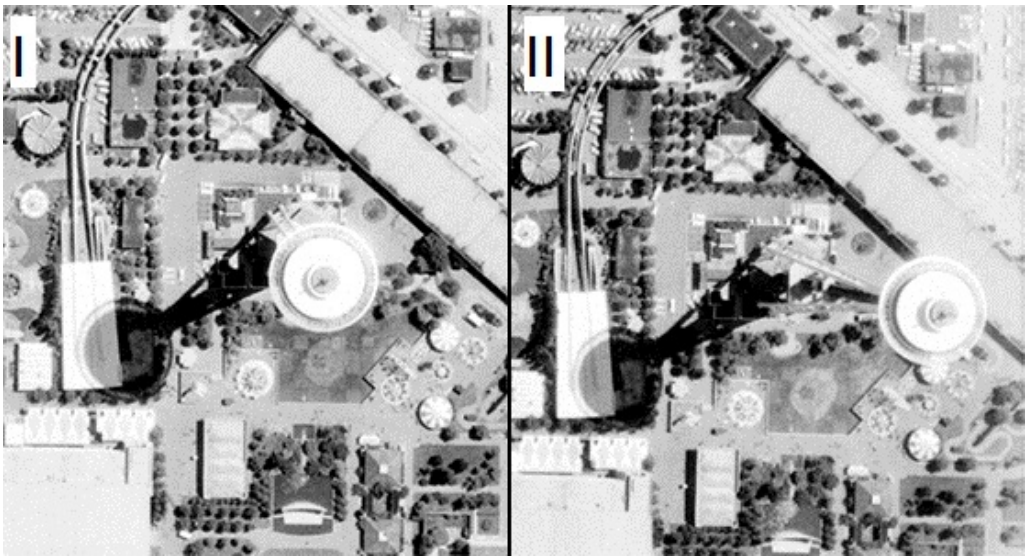

Figure 2.4: An example of how radial displacement can differ between two images. (I) The Space Needle in Seattle is located close to the principle point of the image and thus the displacement is relatively low. (II) The Space Needle is further away from the principle point, the radial displacement is greater and thus the building appears to lean further away from the center (Anon, 2017)

Parallax equations

When aerial and satellite images are taken, tall objects such as buildings appear to lean away from the center of the image. This phenomenon is known as radial displacement (Figure 2.4). The further away the object is from the principle point of the image (in the case of a perfectly vertical, or nadir, photograph, this would be the center), the greater the displacement of the top of the object with respect to the bottom of the object.

A parallax is the apparent displacement in the position of an object, with respect to a frame of reference, caused by a shift in the position of observation (Wolf et al., 2000). The parallax equations are used to calculate the elevation of the terrain from the apparent displacements in the images (Wolf et al., 2000). The height (h_A) of a point (A) can be calculated using equation 2.1

$$h_A = H - \frac{Bf}{P_A} \tag{2.1}$$

Where H is the flight height (altitude of the camera at the time of exposure), f is the focal length of the camera, B is the air base (the linear distance between the

two camera positions) and P_A is the parallax of A. The individual locations where images are captured are called exposure stations — this the position of the camera at the time of the camera sensor (or film) exposure. Furthermore, equations (2.2) and (2.3) can be used to determine the x (X_A) and y (Y_A) ground co-ordinates of point A (i.e. latitude and longitude of the object on the ground surface):

$$X_A = B\frac{x_a}{P_A} \tag{2.2}$$

$$Y_A = B\frac{y_a}{P_A} \tag{2.3}$$

where x_a and y_a are the image co-ordinates of the point A (i.e. the location of A within the gridded raster image, the cell co-ordinates).

Collinearity equations

The collinearity condition is that for any point in a photogrammetric project, the exposure station and its photo image all lie along a straight line in 3D space (Wolf et al., 2000). This condition is expressed in two equations, one for x photo co-ordinate and one for the y photo co-ordinate. The linearized forms of these equations are as follows (Wolf et al., 2000):

$$b_{11}d\omega+b_{12}d\phi+b_{13}d\kappa-b_{14}dX_L-b_{15}dY_L-b_{16}dZ_L+b_{14}dX_A+b_{15}dY_A+b_{16}Z_A = J+v_{x_a}dd \tag{2.4}$$

$$b_{21}d\omega+b_{22}d\phi+b_{23}d\kappa-b_{24}dX_L-b_{25}dY_L-b_{26}dZ_L+b_{24}dX_A+b_{25}dY_A+b_{26}Z_A = K+v_{y_a} \tag{2.5}$$

The $d\omega$, $d\phi$ and $d\kappa$ terms relate to the orientation angles of the photo, whereas the dX_L, dY_L and dZ_L terms are corrections for the initial approximations for the exposure station co-ordinates. The dX_A, dY_A and dZ_A terms are corrections to initial values for the object space co-ordinates for point A. This method provides approximations for the x and y values, because the higher order terms are ignored when linearizing the equations with Taylor's theorem (Wolf et al., 2000). As such, this can be solved iteratively until the magnitude of the corrections become negligible.

Thus, these equations can be used to refine the x and y ground co-ordinates of a point before calculating the elevation using equation (2.1).

Photogrammetric software

Recently, improvements in computational speed, memory and digital imagery capabilities have allowed photogrammetry software packages to be developed. There are multiple software packages available to deal with various types of photogrammetric projects. Some of these include the ERDAS Imagine Photogrammetry Suite, Photomodeler, Agisoft Photoscan, MicMac and SOCET SET. These packages take account for the geometry of various camera types, as well as to make corrections for lens distortions, principle point offset, atmospheric effects and camera orientation. Photogrammetric projects may range from covering small trace fossils (Mallison and Wings, 2014; Falkingham, 2011) to historical buildings (Eisenbeiss, 2009), cities (Over et al., 2010) and landscapes (Bi et al., 2018; Abdrakhmatov et al., 2016). However, only a few of these software packages have support for stereo satellite images, such as ERDAS Imagine and MicMac. I chose to use the ERDAS Imagine Photogrammetry suite as it one of the most popularly used software packages for this type of photogrammetric project. Furthermore, ERDAS has support for stereoscopic satellite imagery as it is able to, with the use of RPCs, approximate camera geometry for the push-broom sensor of the Worldview-3 satellite.

Photogrammetric projects

As previously mentioned, photogrammetric projects can be created with a range of different media including: satellite imagery, aerial photographs, UAV images and photos from digital cameras. Each of these types of imagery have unique advantages and disadvantages when generating a DEM. The greater the resolution of the images, the more detailed the final DEM will be. Satellite and aerial photography are ideal for creating DEMs for large areas. UAV photogrammetry is able to produce a DEM for smaller, but still sizeable areas. UAV photogrammetry is often regarded as a cheap alternative to the more conventional acquisition of aerial photography, however, this has some tradeoff as more images may be required to produce a product of similar quality (Eisenbeiss, 2009). Thus UAV photogrammetry can be more com-

putationally intensive and the data acquisition would be far more time consuming. Nonetheless, UAVs have been used to produce DEMs of archeological sites, castles and other world heritage sites (Eisenbeiss, 2009). Handheld cameras may also be used to produce high-resolution DEMs, although these are usually of considerably smaller features, such as trace fossils (Mallison and Wings, 2014; Falkingham, 2011).

2.1.2 Image acquisition

Traditionally, frame cameras were used in photogrammetric projects. This is because, by using stationary film and a fast shutter speed, the change in position of the camera at the time of capture was considered negligible (Methley, 1986). This allowed images taken from a moving plane (aerial photography) to be used for topographical mapping. The camera lens acts as a geometrical point source as well as the boundary between the object plane and the image plane (in this case, the film). Furthermore, the geometry of a frame camera can be known exactly, allowing the construction of a rectangular co-ordinate system upon which measurements can be taken from the photograph. This is provided that certain other parameters such as flight height and camera angle are known.

Satellite imagery is different from frame cameras in several ways. These cameras no longer operate with film or a physical shutter. Instead they use sensor plates which can capture a range of spectral wavelength bands, often ranging from visible light to infrared (Baldridge et al., 2009). The Worldview-3 satellite collects imagery on a spectral range of 0.450-0.800 μm and uses two push-broom scanners, allowing it to acquire multi-spectral and panchromatic images simultaneously (Maglione, 2016). A push-broom sensor is comprised of a scanner with a linear array of sensors. The image is collected one line at a time, with all the pixels in that line being collected at the same time (Fig. 2.5a). The lines are perpendicular to the direction of flight (Maglione, 2016). As more than one image has to be collected, and the return period on the most modern satellites are still on the order of a day, the images have to be collected on the same orbital pass. As such, the first image is taken as the satellite approaches the target area then, as the satellite passes overhead, the second image is taken (Fig. 2.5b).

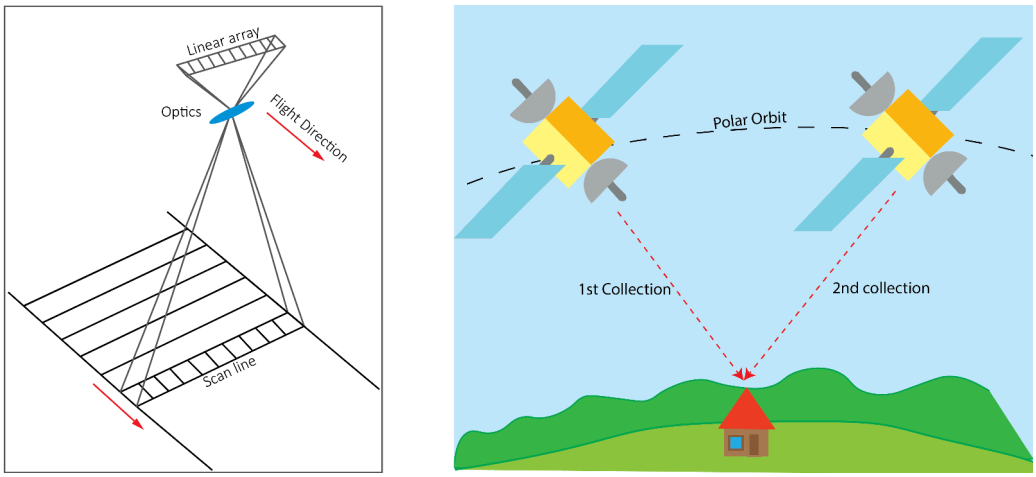

(a) Push-broom sensor image collection for the Ikonos-2 satellite. Adapted from Maglione (2016)

(b) Simple model showing how the satellite imagery is collected on one orbital pass.

Figure 2.5: Acquisition of satellite imagery

Because satellite imagery is not captured by frame cameras with rigid geometrical models, another method has to be used in order to allow the mapping of 3D object co-ordinates from 2D image co-ordinates. The rational function model (Tao and Hu, 2001) has been used since 1999 to model sensor orientation and assist ground point determination from Ikonos, Quickbird and Worldview satellite imagery (Fraser and Hanley, 2005). The rational function model has 80 different Rational Polynomial Coefficients, which are often referred to as RPCs (Fraser and Hanley, 2005). These RPCs are calculated for the images and are included in the imagery bundle as a .rpc file. Despite some initial hesitancy about the quality of RPCs supplied with imagery, Fraser and Hanley (2005) demonstrate that RPCs provided by DigitalGlobe Inc. are equivalent to the rigorous model and thus suitable to be used in photogrammetric projects. While this may be the case, it is necessary to use Ground Control Points (GCPs) if absolute accuracy is required. This is because the rational function model produces only relative accuracy and GCPs are required to achieve absolute orientation and position (Fraser and Hanley, 2005). A minimum of 3 GCPs should ensure that the DEM is not warped or sloped compared to the Earth's surface, although it is common practice to include more GCPs for redundancy. It is important to note that DEMs created from stereoscopic imagery can contain additional distortions from jitter (vibrations of the platform, Tadono et al.

(2014)), striping from Charge Coupled Device (CCD) misalignments as a result of push-broom sensors having several combined CCD line arrays rather than a single CCD line array (Chen et al., 2014). Furthermore, aliasing and illumination bias can cause further distortions that are not accounted for by the RPCs, these distortions can result in topographically correlated noise.

The imagery used in this project was captured by DigitalGlobe's Worldview-3 satellite. The Worldview-3 satellite was launched in 2014 and has an orbital elevation of 617 km with a re-visit frequency of <1 day — at nadir, with 4.5 days at 20° off nadir (Maglione, 2016). With 0.31 m panchromatic and 1.24 m multi-spectral resolutions at nadir respectively, Worldview-3 imagery is among the highest resolution imagery that is commercially available (Maglione, 2016). Worldview-3 has the capability of collecting stereo-image pairs in-track for a swath size of $\approx$ 17 km. Three stereo-pairs were purchased for a total area of 226 km^2, giving a buffer zone of 2.5 km on either side of the fault. The imagery was captured on 17 February 2017, with a panchromatic band and four multi-spectral bands being recorded. The panchromatic band was used in the generation of the DEM whilst the multi-spectral imagery was used to classify different sediment packages. The imagery was "stereo-photogrammetry ready" having already been pre-processed and geo-referenced. The geolocation accuracy is rated as <3.5 m CE90 without ground control. The inter-image angle was a maximum of 20°. One image at nadir, the other at 20° off nadir. For more information on the specifications of Worldview-3, please refer to Appendix A for the specifications sheet.

The GCPs were collected during a field-trip to Hebron in November 2018. Two Leica 1200 GPSs were used in a static GPS survey. One GPS acted as the base and the other, the rover. The base station was located in the center of the field area, near the Elegant Desert Lodge farmhouse on the Hyas farm. At each of the GCPs, the rover station recorded position for 40 minutes in order for the locations to have horizontal and vertical accuracies of 10 mm. The GCP locations were selected to be easy to define in the imagery as well as within the field. Some examples of GCP locations include the intersection of vehicle tracks and fences (Fig. 2.6).

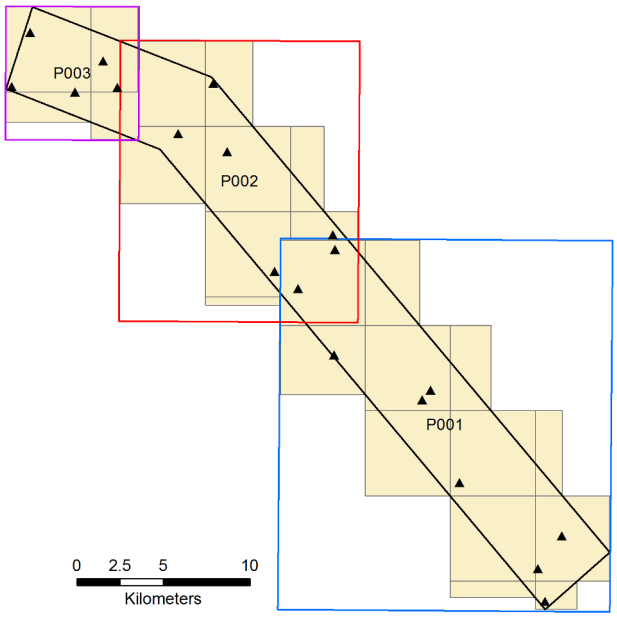

Figure 2.6: Layout of Worldview-3 satellite imagery, each small box represents the border of an individual image pair that were stitched together. Initially, a DEM was produced for each region: P001, P002 and P003. The black triangles are the locations of the GCPs.

2.1.3 Image processing

The study was divided into three regions by DigitalGlobe: P001, P002 and P003 (Fig. 2.6). This was because the study area runs NE-SW, diagonal to the polar orbit of the satellite. The three regions were split into 12, 8 and 4 images respectively in order to keep within the file size limit for geotiffs. A DEM was generated for each of the regions, these DEMs were then stitched together into a single DEM. This was done at the same time as the DEM was down-sampled and converted back to a tiff in order to reduce file-size and make the extraction process smoother.

The images were processed in ArcMap 10.6 as well as using the ERDAS Imagine 2018 software package. In ArcGIS, the images for each scene were mosaic-ed to form complete images for each scene. The images were then re-projected to UTM WGS 84 Zone 33S. This changed the default units from decimal degrees to meters, thus making future measurements on the images and DEM easier to read. Next, both images for each scene (P001, P002 and P003) were added to a photogrammetric project in ERDAS Imagine where the histogram equalization tool was run. This tool adjusts the contrast and the image histograms. If the image histograms are

similar, the pairwise matching will be more successful during DEM generation. The images were then ready to be loaded in a photogrammetric project.

2.1.4 DEM Generation

In ERDAS Imagine, a photogrammetry project is created and saved within a .block file, the images can then be added to this file. The next step is to load the interior and exterior extents of the images. This is done by adding the RPC file that accompanies the satellite imagery. In the case of a frame camera, the precise geometry of the camera would need to be input in order for the boundaries to be calculated. The next step is to generate, or add, tie-points. Tie points are used to align the two images and thus must be objects visible on both of the image views. It is important to achieve a good coverage of points across the images, in order to prevent misalignment, especially near the edges of the images.

The "Point Measurement" tool was run which automatically searches for tie points by way of a pattern-finding algorithm. ERDAS recommends that a minimum of 25 tie points are required for accurate results, however, a minimum of 50 tie points was chosen in order to keep the image RMSE values for point locations below 1 pixel (0.33 m). As such, where the point measurement tool was unable to find 50 points automatically, tie points were manually selected until the minimum of 50 points was met. The manual process of picking points was completed using the classic viewer (Fig. 2.7). The images were displayed side-by-side and tie points were selected. A priority was made to select features as accurately as possible. Features that were used included fence-posts, intersections of vehicle tracks and the corners of buildings. These all have well-defined boundaries and thus can be selected with an error of less than a pixel. A further effort was made to distribute the points throughout the image, with a simple grid-like pattern.

For Area 1, two tie points were generated automatically (due to poor contrast in the images) and 51 were manually selected (Fig. 2.8A). For P002, 28 tie points were automatically generated and a further 31 were hand-picked (Fig. 2.8B). P003 had 25 automatically picked and 18 more points were selected by hand (Fig. 2.8C). As P003 was the smallest region, the image RMSE values were well under 1 pixel even though the total number of tie points was less than 50.

Once the tie points were completed, the ground control points were added in

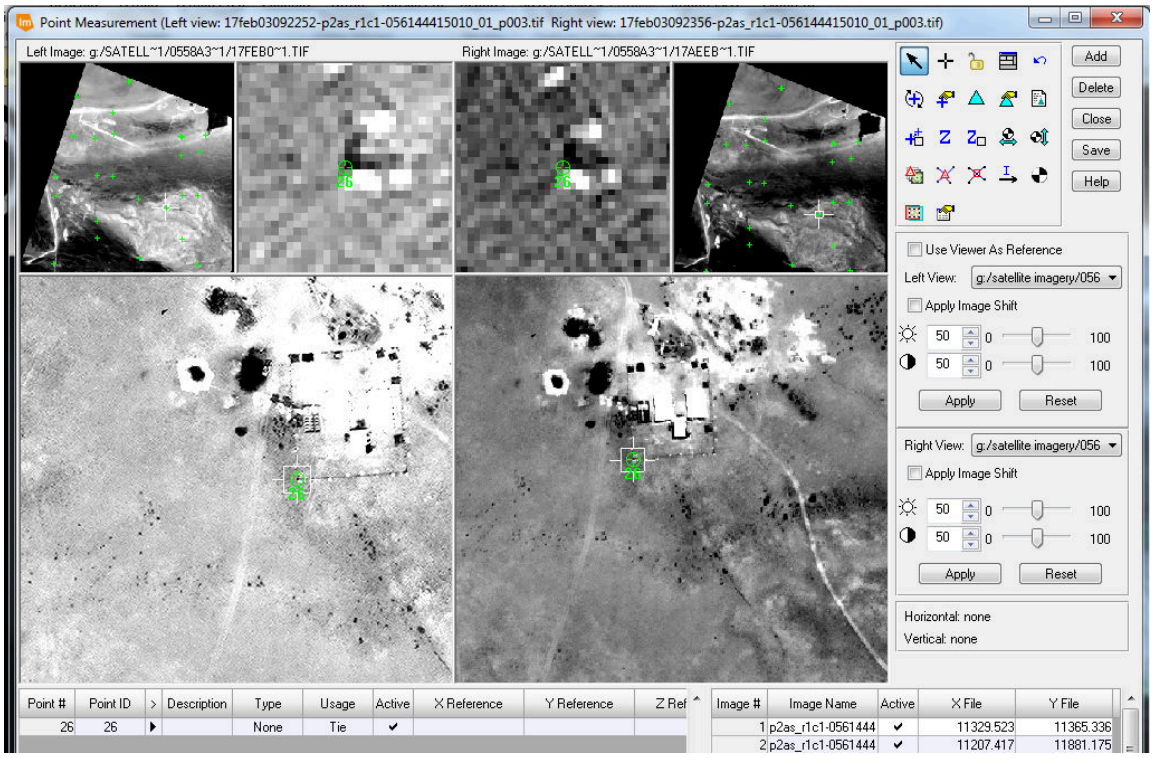

Figure 2.7: Screenshot of tie point selection in the classic viewer

the same manner as the tie points using the classic viewer. Except in this case, the locations for each of the GCPs were added during the feature creation, rather than calculated using the RPCs afterwards. When this was complete, a block triangulation could be run on the images where x, y and z co-ordinates were calculated for the tie points. During this process the GCPs were used as reference and helped achieve absolute accuracy, enabling the DEMs for each region to be easily stitched together later on in the process.

The next step was to create a batch file and run the Automatic Terrain Extraction (eATE) tool. This tool initially uses image matching and semi-global matching to find points that are visible on both images. Once this is done, the x, y and z values can be calculated for those points using a combination of parallax and collinearity equations to ensure minimal errors are present. Due to the proprietary nature of the software, the exact algorithm is not available. The tool produces an irregular dense point-cloud for the overlapping image area. This point-cloud was then rasterized using the nearest neighborhood technique in order to produce a regular gridded raster DEM. The imagery we used had a pixel resolution of 0.4m due to re-sampling

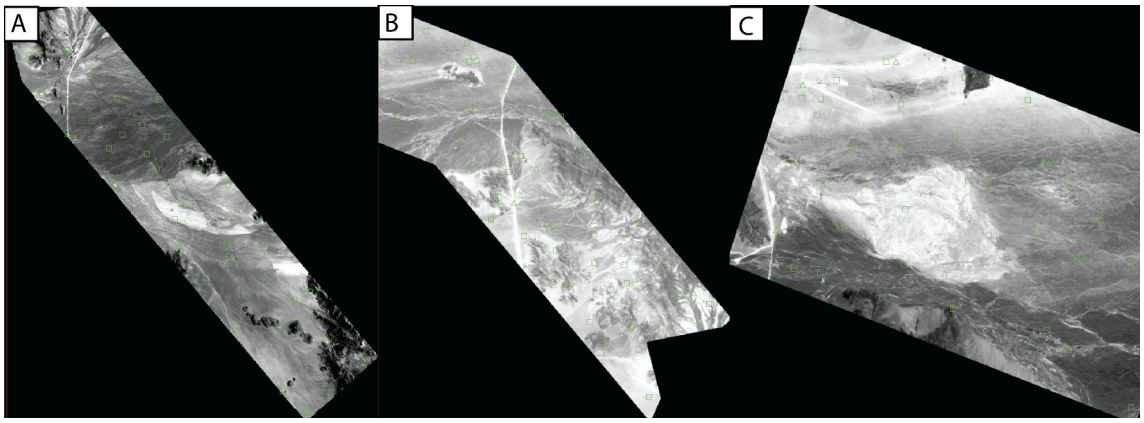

Figure 2.8: Tie point (green squares) and GCP (green triangles) locations for (A) P001, (B) P002 and (C) P003.

for commercial sale (Maglione, 2016). The initial raster DEMs produced had a pixel resolution of 0.33 m, this was re-sampled to 0.5 m when the DEMs were stitched together. The images were stitched using the "Mosaic to new raster" tool in ArcMap.

2.2 Stream Extraction

Once the DEM was generated it can be used to make measurements of various geomorphological features. One of these features of interest is the drainage network. By modelling where water would flow on the DEM, the drainage pattern can be extracted. To provide the locations of the streams present in the field area. This information is useful when analyzing water courses for knickpoints as well as for channel displacements. Note, there are no perennial rivers near Hebron as the area is extremely arid (the area is on the edge of the Namib Sand Sea) and all the waterways in the DEM are ephemeral. These streams are generally quite small with the exception of the Tsauchab river.

The courses of all the streams in the DEM were extracted using ArcGIS, particularly the hydrology section of the Spatial Analyst toolbox. This method produced a shape-file, that not only contains the x, y co-ordinates for all the streams in the DEM area but also includes elevation information for each of those streams. This was used in both the determination of lateral offsets (Section 2.2.2) as well as the knickpoint analysis (Section 2.2.3).

2.2.1 Stream Extraction Procedure

The first tool to be run was the "Fill" tool. This was done to ensure that there were no empty spaces (holes) in the DEM. The values of surrounding cells around any holes present are used to approximate the value of the empty cell using the nearest neighbor technique. A "filled" version of the DEM is produced with no holes present. This tool works well to remove small holes and other imperfections that may be present in the DEM.

Next, the "Flow Direction" tool was run for the DEM. This tool calculates the direction of flow from each pixel in the DEM to its steepest down-slope neighbor (ESRI, b). As each pixel is surrounded by 8 other pixels, there are 8 possible directions for flow. These directions are coded according to the table below (Table 2.1). For example, if the steepest drop was directly to the north of the cell in

question, that cell would be allocated a flow direction value of 64. Similarly, if the steepest drop was to the right of the current processing cell, the flow direction value would be 1. The output of this tool is a raster containing the flow direction values of each cell.

Table 2.1: Direction values for the 8 possible flow directions (ESRI, b)

32	64	128
16		1
8	4	2

The "Flow Accumulation" tool is run with the raster produced from the flow direction tool. The tool calculates the number of cells that flow into the processing cell. A weight raster may be provided, however, if no weighting is given, each cell is allocated a weight of 1. The values of a cell in the output raster is equal to the number of cells that flow into that cell (Fig. 2.9). Cells with flow accumulation values of zero are topographical highs and may be used to identify watersheds and interfluves.

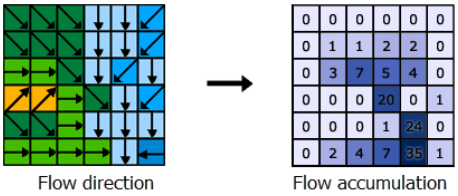

Figure 2.9: Example of how the flow accumulation tool works (ESRI, a)

Cells with high values for flow accumulation represent areas of concentrated flows. These areas are then used to identify stream channels. In order to do so, a limit has to be chosen in order to separate between concentrated flow areas, such as stream channels, and low flow areas. This limit depends on the size of the file as smaller files have less cells and thus the accumulation values will be smaller. Given that the DEM contains over 4 billion cells, a cut-off of 10 000 000 (10 million) was used to identify the stream channels. A range of values were tested and this value was chosen because the results best represented the drainage visible on the imagery. A majority of the stream channels had been identified successfully at this value. The raster calculator was used to impose the limit we chose and then write a new file that only includes the accumulation values that lie above the limit. This was done

with a single line of code (see below). The results of this returned a raster with cell values of 1 for those cells that had an accumulation value of >10 million.

```
stream_channel_raster = Raster("flow_accumulation") > 10000000
```

The last step in the stream extraction was to run the "Raster to poly-line" tool in order to convert the raster output into a poly-line shape-file. A shape-file is much easier to work with, being a much smaller file-size as well as having the ability to simply extract the elevation values from the DEM and write these attributes to the poly-line.

2.2.2 Lateral Offsets

Offset geological features are commonly used to determine the amount of slip generated in one or more earthquakes (Burbank and Anderson, 2012). This is because these features, such as stream channels and river terraces, can be easily observed and measured using photographs or digital elevation models (Fig. 2.10A). Additionally, because they occur along the length of the fault, these features provide insight to the variations in slip along the fault trace (Burbank and Anderson, 2012). The measurement of offset in these geomorphological features provides evidence of strike-slip faulting. A well-known case study of this observation are the channel offsets visible on the San Andreas Fault (Wallace, 1968)(Fig. 2.10B). In the case of a pure strike-slip fault, the distance between the features will be equal to the amount of lateral offset. However, if there is also dip-slip motion, and the slope of the surface is not perpendicular to the fault strike, this vertical motion must be subtracted to determine the horizontal component (Burbank and Anderson, 2012).

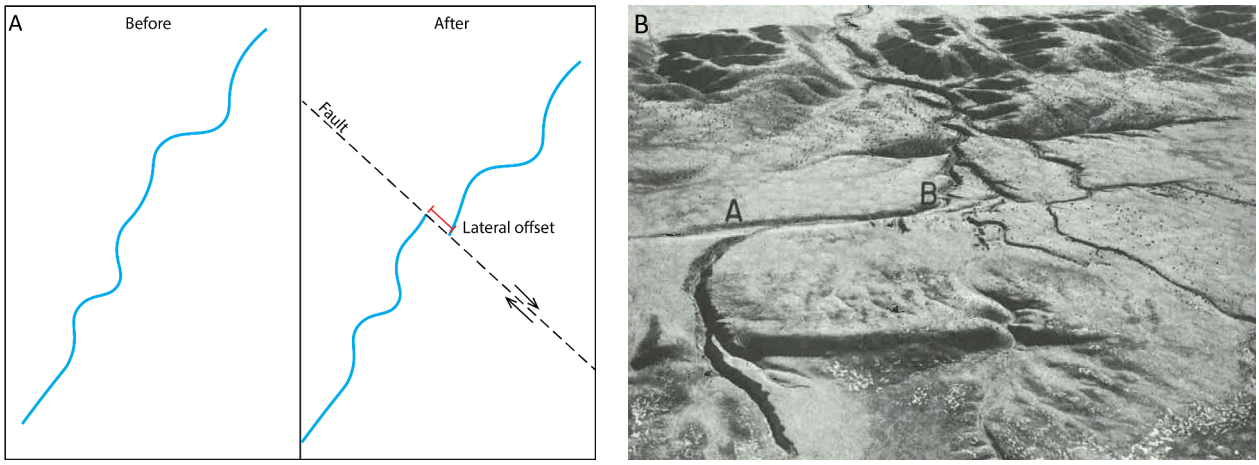

Figure 2.10: (A) Formation of stream displacements as a result of strike-slip faulting. (B) Example of channel displacement from the San Andreas Fault, California (Wallace, 1968)

In order to determine if there was any amount of strike-slip motion on the fault plane, as was observed by Viola et al. (2005)(Section 1.3.2), the river channels that cross the fault scarp were inspected for apparent offsets much like the examples in Fig. 2.10.

The poly-line layer of stream channels (generated above) and a poly-line containing the fault trace were added as layers with the satellite imagery as a base-map.

Using this setup, the river channels that cross the fault scarp were inspected for channel displacements. Specifically, the offsets should be systematic in terms of sense of motion and, to some extent, the magnitude of the offset.

2.2.3 Knickpoint Analysis

For a river in equilibrium, the longitudinal profile will generally be smooth and concave in shape. The steepest gradients are present near the source of the river and the gradient decreases as the river moves towards its base level. Various processes, such as a tectonic movement or the exposure of an easily erodible layer below a more resilient layer, can lead to a portion of the equilibrium profile being steepened. The gradient at that point will therefore increase, along with the energy level (Burbank and Anderson, 2012). Thus, a knickpoint will be created along the rivers profile in that location. Over time, this knickpoint will migrate backwards as a result of erosion due to the increased energy level. When the knickpoint eventually reaches the rivers source, the profile will once again be a smooth concave shape (Fig. 2.11).

In the case of tectonically produced knickpoints, when there is a normal fault and the hanging wall is in the downstream direction, a step or knickpoint, is created along the profile of rivers that cross the fault line. This is the case for Hebron where most of the rivers run NE to SW and the land SW of the fault has been down-thrown. As such the local base level would be lowered during a normal faulting event, producing a knickpoint which should be discernable on a DEM (Burbank and Anderson, 2012). Furthermore, if more than one knickpoint was found to be present on a rivers profile, this may be indicative of multiple events (Fig. 2.11). Each event would form a new knickpoint which would subsequently migrate backwards. By counting the number of knickpoints that are present on a river's profile, some information about the seismicity of the fault it crosses may be extracted. This is provided that the knickpoints have not migrated completely back and returned the profile to equilibrium. Due to the arid climate present in Namibia, the erosion in river channels is likely to be low. Especially considering that all the rivers in the field area are ephemeral, it is quite possible that the river profiles would not have reset

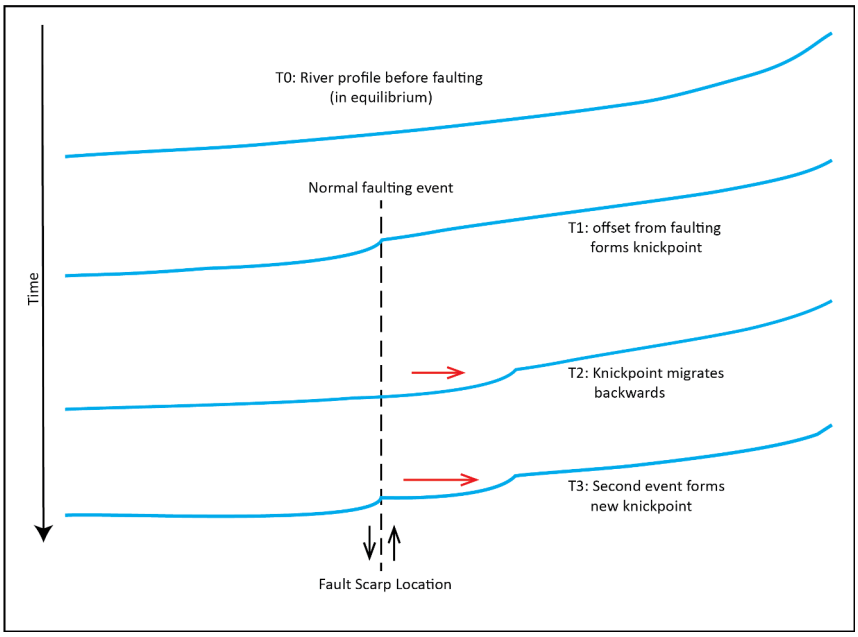

Figure 2.11: Diagram explaining how multiple knickpoints may be preserved as a result of multiple tectonic events

since the last glacial maximum. The erosion rate of other desert surfaces located to the south of Hebron have been calculated to be 3.6 ± 1.9 m/Myr (Bierman and Caffee, 2001). This is negligible, implying that the erosion of large geomorphological features is not noticeable over timescales of 10^5 - 10^6 years (Bierman and Caffee, 2001).

The profiles of the rivers were extracted from the DEM using the "Interpolate Shape" tool in the ArcMap Spatial Analyst toolbox (Fig. 2.12) and the shape-file of drainage. The profiles of 20 rivers were selected. These rivers were distributed along the length of the map and they all crossed the fault at a bearing that was nearly perpendicular to the strike of the fault. The lengths of these rivers are variable from approx 500 m to 5 km, and the size of the channels represented the variability of the stream channels found in the DEM. The longest and widest river in the field area (the Tsauchab river which feeds Sossusvlei) was not used as its braided network of channels lead to considerable artifacts when extracting the profile. In particular, the channels extracted for the Tsauchab show a lot of noise due to smaller channels and sand-banks. Furthermore, the Tsauchab has eroded away the fault scarp near its course and thus any knickpoint may have migrated backwards considerably,

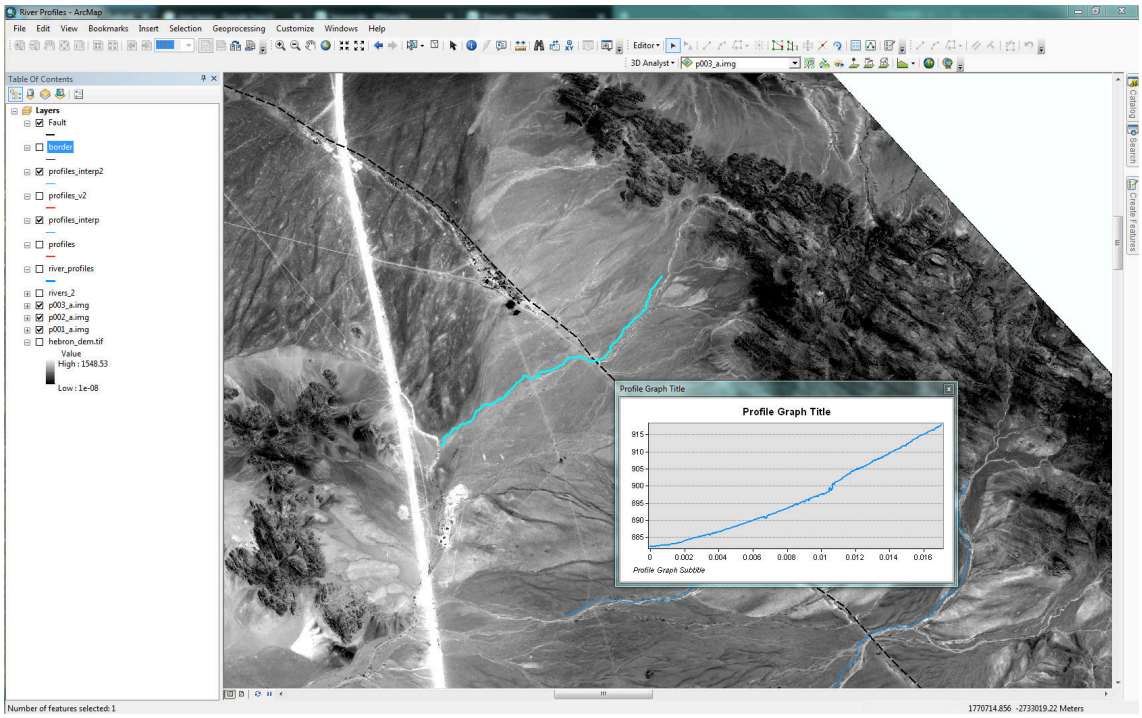

Figure 2.12: Screenshot of the river profile extraction within ArcMap

potentially out of the DEM itself.

Once the profiles for the selected rivers were extracted (Fig. 2.12), they were exported as a text file and plotted individually in Excel. The elevation data was then smoothed using the exponential smoothing function within the Data Analysis Add-on in Excel. A dampening factor of 0.9 was used, to smooth the data in order to reduce the amount of noise in the following steps. The slope (m) between each point along the profile was then calculated as the change in elevation divided by change in distance along the profile. A moving mean was then taken with a bin width of 10 values. This bin width corresponds to a horizontal window of approximately 5 m and was chosen as the majority of boulders and shrubs that cause noise in the DEM would be smaller than this. The moving mean values were then plotted along with the river profile. The distance to the fault from the start of the channel was measured using the ruler tool in ArcMap and added to the plots. Knickpoints were chosen where the change in slope (Δm) had positive peaks. As the profiles all followed the same direction, moving from the down-thrown block over the scarp and onto the up-thrown block, this agreed with the expected change in slope values. Signals in the Δm plot that had both positive and negative peaks were most likely

smaller features such as trees or boulders which would show an increase in slope (positive Δm) followed by and equally sized decrease (negative Δm)(See Fig. 2.13).

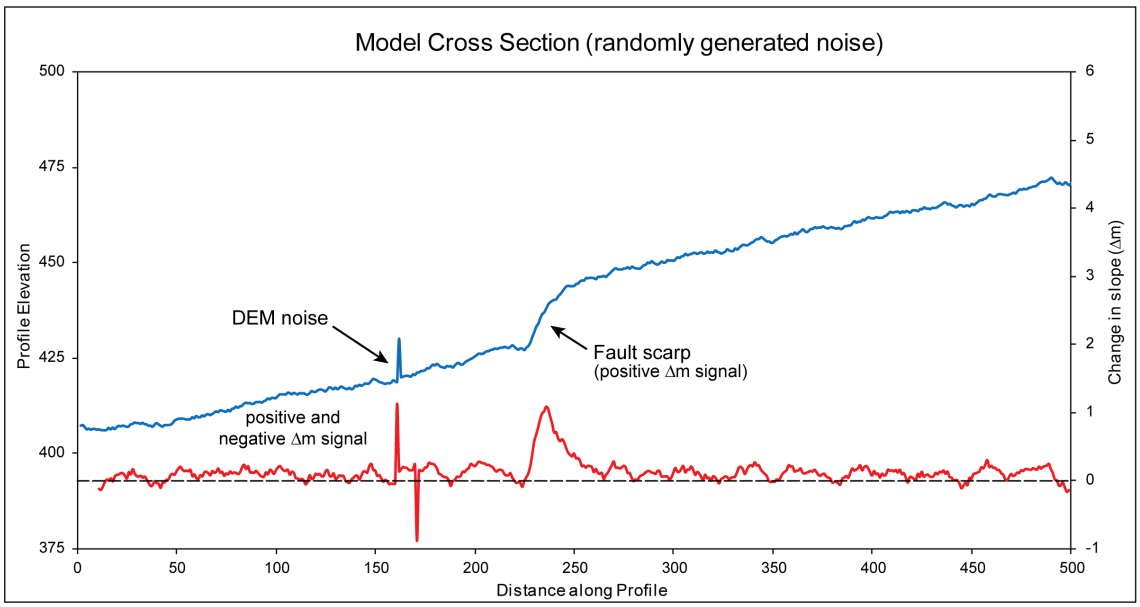

Figure 2.13: Model of knickpoint analysis on a generic profile with randomly generated background noise. DEM noise was simulated to show how the change in slope values respond to this noise compared to the fault scarp. The delay before the decrease in signal (Δm) for the anomalous knickpoint may be due to the bin width ($\approx$ 10 m) used in this example.

2.3 Vertical Offsets

For a fault scarp to form, there must be some amount of dip-slip movement on the fault plane to move one block up relative to the other. Therefore, the measurement of the height of a fault scarp can be used to calculate the amount of vertical motion that has occurred on the fault plane. By taking measurements of the fault scarp along its length, the variation in slip along the length of the fault can be determined. However, it is important to note that if the slope of the surface is not parallel to the dip direction of the fault, then lateral movement of the fault can cause an apparent vertical offset (Mackenzie and Elliott, 2017). Historically, scarp heights were measured using survey equipment such as a theodolite. This process is time consuming and thus requires extensive time in the field. However, high resolution DEMs can also be used to make scarp measurements (Burbank and Anderson, 2012). Using a DEM has the advantage that the process can be semi-automated fairly easily and thus many more measurements can be made, providing significantly more detail than previous field surveys.

The following general procedure was followed in order to measure the scarp height. A cross sectional profile, perpendicular to the fault scarp, is extracted from the DEM. Two planes are then identified within the profile — one representing the surface of the down-thrown block, the other representing the up-thrown block. The vertical distance between these two surfaces is then measured to obtain the scarp height.

2.3.1 Cross section selection and issues

While it is possible to automatically generate and extract cross sections at predetermined intervals (for example, every meter along the scarp), I chose instead to select the cross sections by hand. This was done in order for the measurements to accurately represent the scarp with as little interference from other geomorphological features as possible. As such, the cross sections were subject to several selection criteria.

The selected cross sections were taken as perpendicular lines to the fault trace. An average length of 500 m was used, however in some circumstances this was not ideal and so the length of the cross section was adjusted. In the step over zone, the length was much longer in order to fit both of the fault scarps and to get a representative surface for the down-thrown and up-thrown blocks.

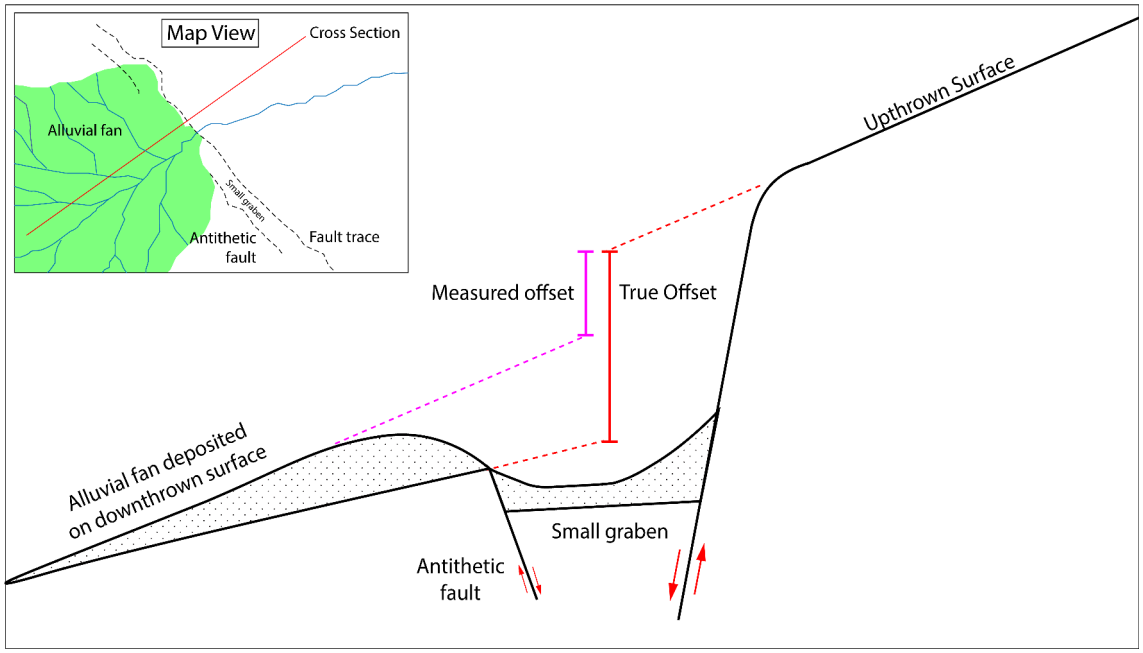

Figure 2.14: Cross section of how a post-faulting alluvial fan can affect the measurement of scarp height. Inset (top left) shows a map view of the fan.

In the Hyas Farm, the fault scarp runs through an outcrop of Proterozoic basement rock (Fig. 1.3). This outcrop forms a valley which the fault runs through, parallel to the valley floor. When a cross-sectional length of 500 m was used in this area, anomalous values were obtained. This is because the steep valley sides affect the plane fitting section of the Matlab code (Appendix C) negatively. The planes were fitted to the sides of the valley, leading to large and even negative values as the dip of the planes were in opposing directions. At some locations at lower gradients in the valley, it was possible to obtain a reasonable offset as long as the cross section was kept short ($\approx$ 100 - 200 m long).

Some criteria that was used for selecting the cross sections included the following:

- Presence of a river channel. In particular, river channels that were located close to the fault were avoided, because a channel located on the down-thrown surface may artificially increase the observed scarp. Additionally, where rivers cross the scarp, they decrease the gradient and reduce the scarp height by depositing material on the lower surface. Furthermore, there were some cases where rivers on the up-thrown surface had been deeply incised and the steep banks in those cases are not ideal for the plane fitting solution.

- The same geomorphological surface. An effort was made to draw sections in areas where it was clear that the same geomorphological surface was present on both the up-thrown and down-thrown surfaces. Different geomorphological surfaces may have unique gradients which could lead to inaccuracies in the measured offsets.

- Slope angles were not too high. When steep slopes are introduced, particularly if they are opposite directions to one another, the offset measurements can be anomalously high or even negative. Thus cross sections were generally shortened (or at worst, avoided) in selected areas where high topography was located close to the fault scarp. One such area included the outcrop of Proterozoic basement in the Hyas Farm in the central region of the DEM. Another was an inselberg of basement outcrop located in the Neuhof reserve, the same inselberg upon which the dip was calculated (Section 2.5).

- The fault was located in the center of the cross section. This is because the Matlab code expected the fault scarp to be within the center of the cross section. Thus some cross sections where either the up-thrown or down-thrown surfaces had been intensely modified were avoided. This is because these altered surfaces would be difficult to fit a representative plane to. Examples of this include incised river channels on the up-thrown block as well as large alluvial fans deposited on the down-thrown block (Fig. 2.14).

- Spacing between the cross sections was approximately 250 m where possible. Cross section locations were adjusted if the presence of river channels, alluvial fans or a clear change in sedimentary units were to interfere with this spacing.

A total of 160 cross sections were selected, with an average spacing (along the length of the fault) of 250 m. This is well over 10 times the number of scarp measurements made by White et al. (2009).

2.3.2 Determination of scarp height

A MATLAB function, called `cross_section`, was created which generates plots of the cross sections, fits planes to the up-thrown and down-thrown surfaces and calculates the vertical offset. The complete script can be found in Appendix C. The function takes two input arguments, a csv file and the approximate spacing (in m) between the cross sections. The profile csv has the horizontal distance (x) and elevation (z) in separate columns for each cross section. This is the format that ArcMap outputs profiles when using the Spatial Analyst Tool. The function produces three variables as the outputs, namely the vertical offset for each profile, the moving mean of these values and a variable with the distances along the length of the fault.

The function starts by reading the cross sections from a comma separated file and converting these to an array. Further variables are created for the lower and upper planes of each cross section, i.e. the down-thrown and up-thrown surfaces respectively. A linear regression is run in order to fit a linear plane to these lower and upper planes. Outliers from this first iteration are removed and the regression is run again, this time without the outliers. The vertical offset between the two planes is then calculated for each cross section. A plot is produced with the profile and fitted planes.

2.3.3 Calculation of slip

Once the amounts of horizontal and vertical slip are known, the total amount of slip along the fault plane can be calculated. The horizontal slip component, as can be calculated in Section 2.2.2, is already aligned to a principle axis. The dip-slip component of slip needs to be converted into the remaining two principle axes, with a horizontal and vertical component. If only one of these is known, the other components can be calculated using trigonometry.

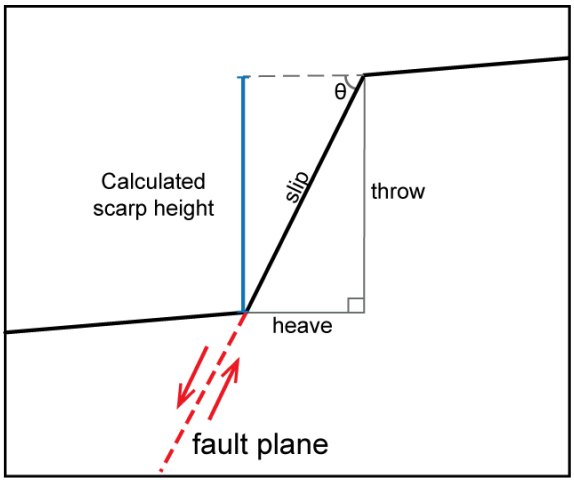

Figure 2.15: The scarp height is equal to the purely vertical component of slip, otherwise known as the throw. The slip can be calculated from the throw, taking into account the angle between the dip (θ) and the vertical component.

The dip-slip motion can be separated into a purely vertical component, known as the throw, and a purely horizontal component, known as the heave. By measuring the height of the scarp in Section 2.3.2, the throw of the Hebron fault was measured (Fig. 2.15) and thus the slip can be calculated from this using Equation 2.6; where S is the slip, T is the vertical component or throw (scarp height) and θ is the dip of the fault plane.

$$S = \frac{T}{sin(\theta)} \tag{2.6}$$

Estimating the dip of a normal fault from surface observations can be challenging, especially as normal faults can steepen as they pass through unconsolidated sediments (Bray et al., 1994). In this study, a combination of field observations, satellite imagery measurements (Section 2.5) and seismological observations (Section 4.4) were used to estimate the dip of the fault.

2.4 Mapping Sediments

Satellite imagery is often divided into different spectral bands. Combinations of these bands can be used to pick out features with different characteristics to their surroundings. For example, satellite imagery can be used to map cities, cultivated land, vegetation type and even geological units. This technique was first implemented in 1972 with the launch of the Landsat I Multi-spectral Scanner (MSS) (Goetz et al., 1981). The use of satellite imagery was confined to mapping fairly broad regions, due to the coarse resolution of the imagery. However, with increasingly more accurate satellite imagery, and the incorporation of DEMs, remote sensing data can be used to map finer and finer features (Siart et al., 2009).

The Worldview-3 satellite imagery that was acquired for this study's field area included multi-spectral images. These multi-spectral images have four bands and a spatial resolution of 1.24 m. Any combination of these four bands can be displayed in the Red, Green, Blue and Alpha (RGB+A) Channels within ArcMap. By selecting different band combinations several effects can be achieved. For example, by selecting the combination of 4,2,1 (RGB), a false colour image is created which displays green vegetation in red and man-made features a light blue. See Figure 2.17 for an example of this effect.

To map different geomorphological and geological surfaces from the imagery, several band combinations were used. These combinations included 1,2,3; 2,1,3; 1,3,4 and 4,2,1. As different combinations highlight unique features within a particular surface, it was beneficial to use a selection of band combinations to identify the boundaries between several surfaces. The reflectance of surfaces is due to the lithology and vegetation. Thus differences in reflectance can allow one sediment unit to be differentiated from another. As most of the study area is covered by the Karpfenkliff conglomerate (White et al., 2009), the variation in lithology is likely due to different sources for this unit. These sources may include the Sinclair Group Proterozoic basement rocks and the Nama Group sedimentary rocks which make up the Great Escarpment in this region.

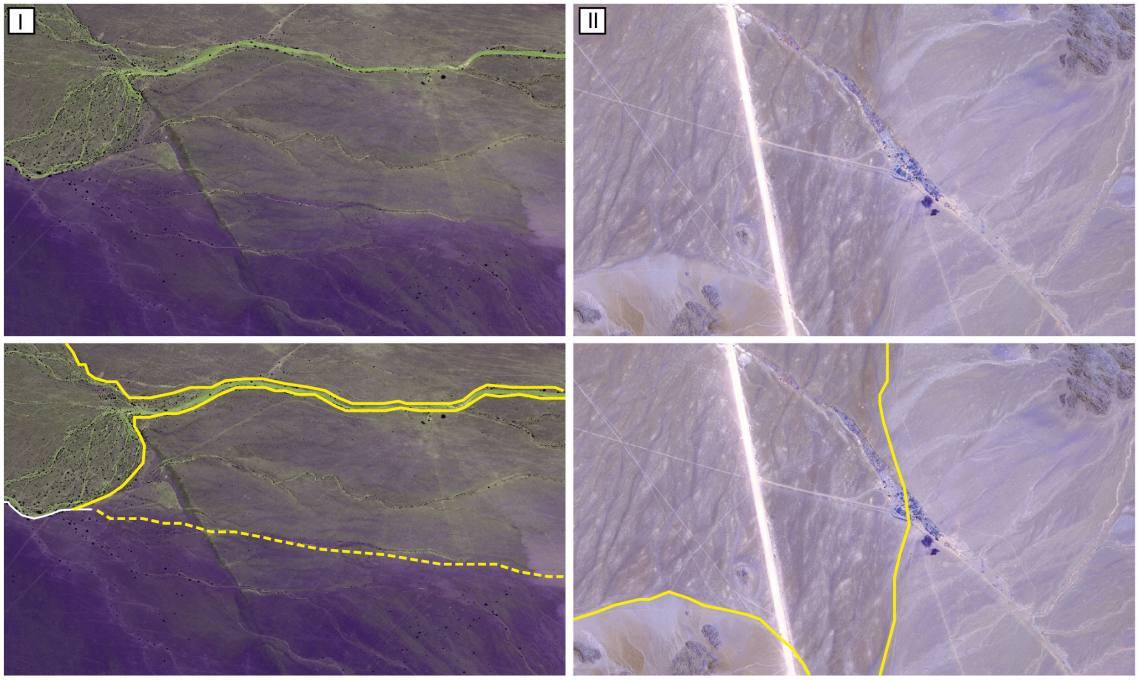

Figure 2.16: Examples of sediment mapping due to different reflectance and drainage patterns evident on the multi-spectral Worldview-3 imagery (I) sediments that displayed a significant difference in reflectance. The bottom panel shows inferred sediment package contacts (yellow lines). Note that the dashed line represents a gradational contact for an area without a distinct change in reflectance.
(II) Example of sediments that did not show as distinct a reflective difference. However, the drainage patterns were used to help differentiate between units. The bottom panel shows inferred sediment package contacts (yellow lines).

Additionally, the drainage patterns and vegetation present were used to constrain the boundaries of the surfaces. In some cases the vegetation will change depending on the lithology, due to different soil types and thus, a different dominant vegetation type. In Hebron, the vegetation is sparse with numerous desert gravels at the surface and, if present, vegetation is usually grassland. The Neuhof reserve, located on the southern extent of the fault was categorized with grasses and scattered shrubs. The NW limb of the fault, just south of Sesriem also had scattered shrubs but less grass. The rest of the fault was categorized by grasses and gravel pavements. Drainage patterns, such as the size, number and spacing of channels on a surface were used to separate units from one another. The directions of flow on these channels also helped to identify units. The mapping was done in ArcMap by tracing the surfaces with the create area feature tool.

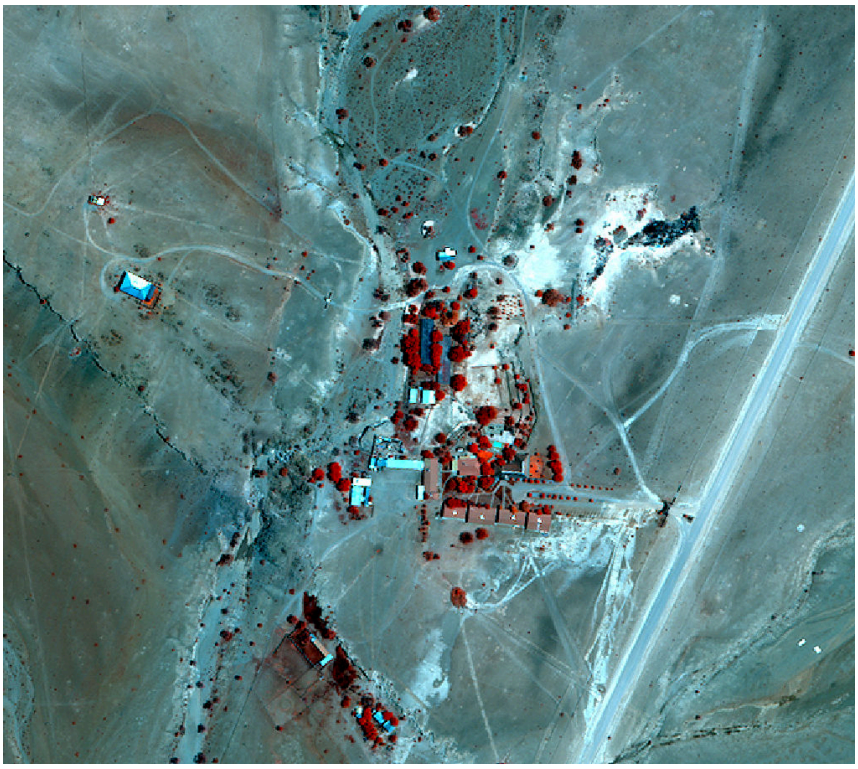

Figure 2.17: (A) Example of the false color image created by using the band combination of 1,3,4 in the RGB channels of the Worldview-3 multi-spectral imagery. Vegetation is highlighted in blue and sand is a clay-orange.
(B) Image with band combination 4,2,1. Vegetation is in red while man made features are in blue and brown.

2.5 Dip Calculation

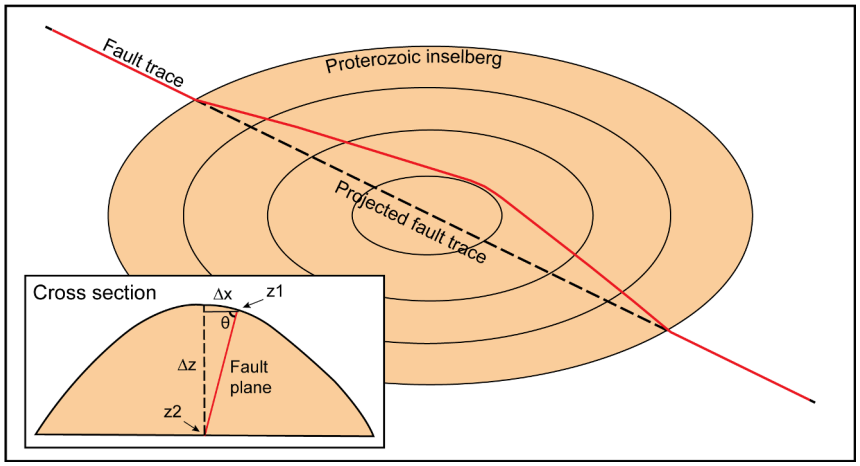

Figure 2.18: Calculation using offset of fault trace through an inselberg of Proterozoic basement rock from satellite imagery and the DEM. Projected fault trace is for a flat surface

The dip of the fault plane was measured in the field north of Hyas Farm, where the fault runs through an outcrop of Proterozoic basement rock. The dip in this area was measured to be around 70°. In addition to this, it was possible to obtain a measurement of the fault at the surface using offsets in the satellite imagery. In the southern section of the DEM, the fault runs through an inselberg of Proterozoic basement rock. The fault trace in this area makes a wide "V" shape. The dip was measured by taking the horizontal distance (Δx) between the actual surface position of the fault scarp and the projected position of the fault scarp, assuming a flat surface (Fig. 2.18). This projected surface position was a straight line connecting the edges of the inselberg. The heights of the two points were then measured off of the DEM. z_1 was the elevation of the scarp outcrop and z_2 was the elevation of the projected line. These heights were used to calculate the vertical difference (Δz) and solve for the dip (θ) of the fault plane using the expression, $tan\theta = \frac{\Delta z}{\Delta x}$.

Results

3.1 The Digital Elevation Model

The final DEM (Figure 3.1) was rasterized from a point cloud of over 127 million points and covers an area of 239 square kilometers. The point cloud has an average density of 0.57 points per square meter (pts/m^2). However, this is generally higher in the areas proximal to the fault scarp, with a point density of $\geq$ 1 pts/m^2 (Fig. 3.2 A). This is because the feature finding algorithm struggles with large, flat low-contrast areas. Near the fault scarp there are shadows, small channels and more vegetation. Thus, there are usually more points surrounding it than some feature-poor areas distal to the scarp. This average point density is similar to the minimum densities (0.5 - 1 pts/m^2) obtained in large scale LiDAR acquisitions (Anderson et al., 2006). While significantly higher density point clouds can be acquired using LiDAR — such an acquisition would be very expensive. Table 3.1 summarizes the results of the block triangulation that was run on the tie points and GCPs before the DEM was generated for each of the three sections; P001, P002 and P003 (Fig. 2.6). The RMSE values in Table 3.1 are the square roots taken from the average (mean) of squared errors for each tie-point and GCP. This is used as a measure of how well the images are "tied" together. The RMSE values are all below 1, in other words, the difference between the predicted and observed locations of each tie point and GCP was less than 1 pixel (0.33 m).

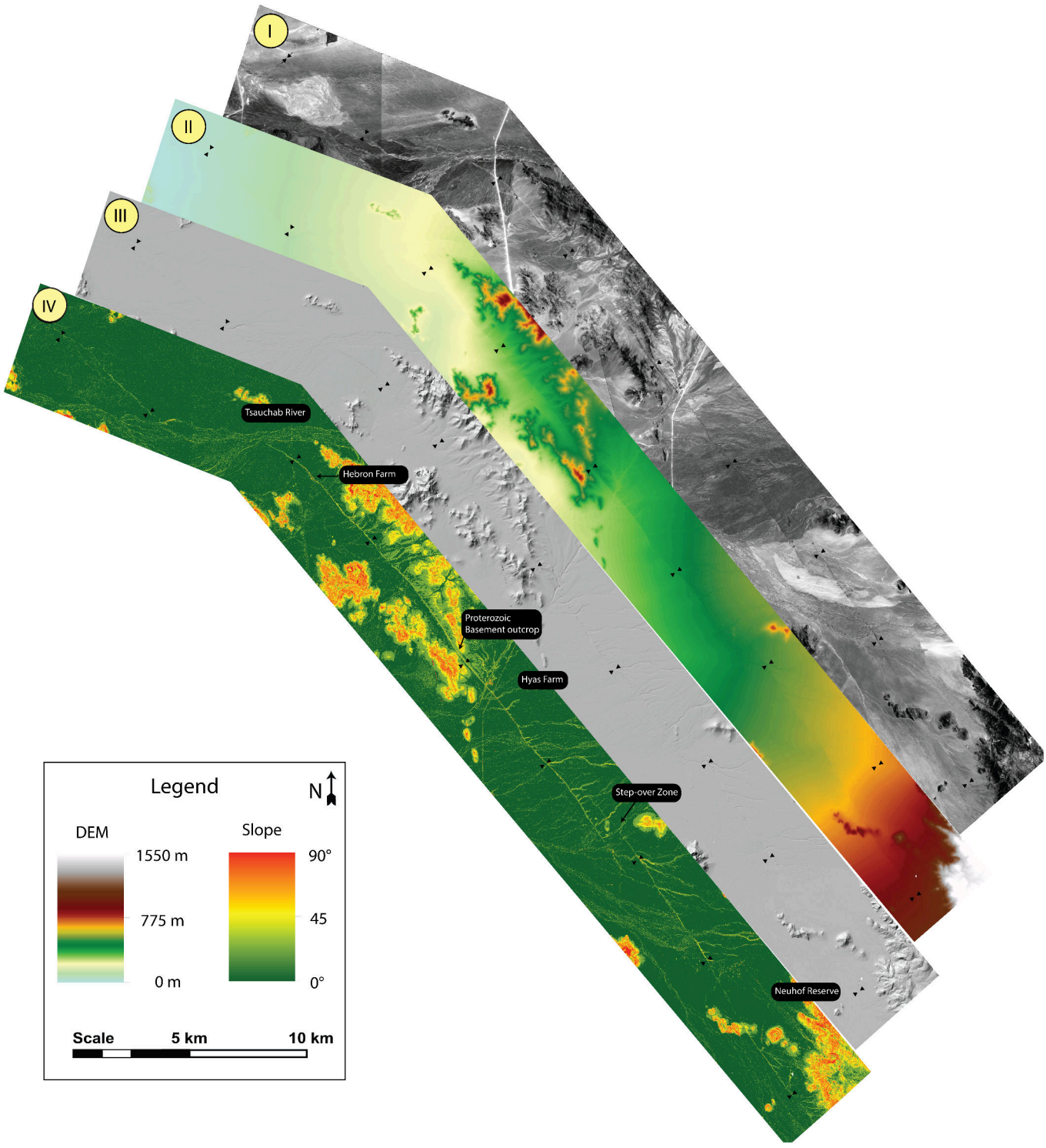

Figure 3.1: (I) One view of the stereoscopic pan-sharpened Worldview 3 imagery (0.33 m resolution) used to generate the DEM.
(II) The rasterized DEM with a pixel resolution of 0.5 m.
(III) Hill-shaded DEM. The fault is clearly traceable on this as well as the incision in river channels on the up-thrown side of the fault.
(IV) Slope angle for the study area. Green colours are close to 0° while hotter colours represent higher slope angles, the fault scarp is easily observable in this layer.

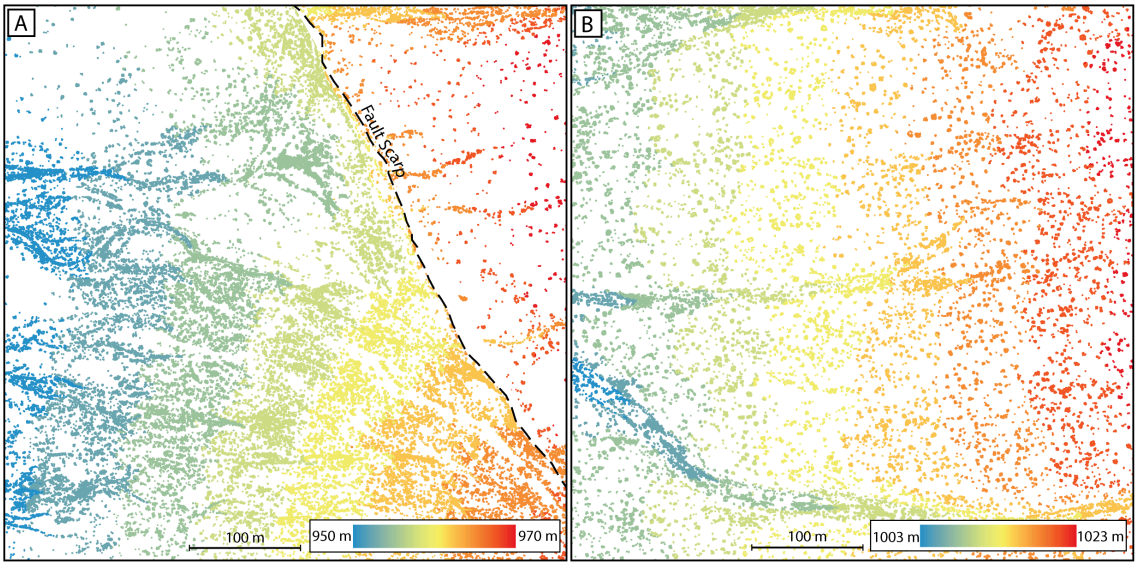

Figure 3.2: Subsets of the point cloud to show variation in point cloud density.
(A) location close to the fault scarp with a point density of 1.06 pts/m^2.
(B) location away from the fault with less linear features and a point density of 0.56 pts/m^2.

Table 3.1: Block Triangulation Results

Region	Auto Tie	Manual Tie	GCPs	RMSE	rmsex	rmsey
P001	2	51	5	0.355	1.057	1.082
P002	28	31	5	0.345	0.996	1.149
P003	25	18	6	0.252	0.529	0.752

The DEM was initially produced with a pixel resolution of 0.33 x 0.33 m. This was re-sampled to be 0.5 x 0.5 m to reduce file size. The white spaces visible in Figures 3.3 A and 3.3 B are areas where the point cloud was not dense enough for the rasterization process to adequately fill the remaining spaces. These areas are flat, highly reflective surfaces with low contrast and very little vegetation. As a result, the feature finding algorithm did not produce enough points for that area to be rasterized. These holes have been filled using the ArcMap "Fill" tool which uses the nearest neighbor technique to estimate the ground surface of the hole from the values of the surrounding cells. There are some remaining artifacts, including some small steps (see the black lines near the voids in Fig. 3.3 B) in the filled areas of the DEM.

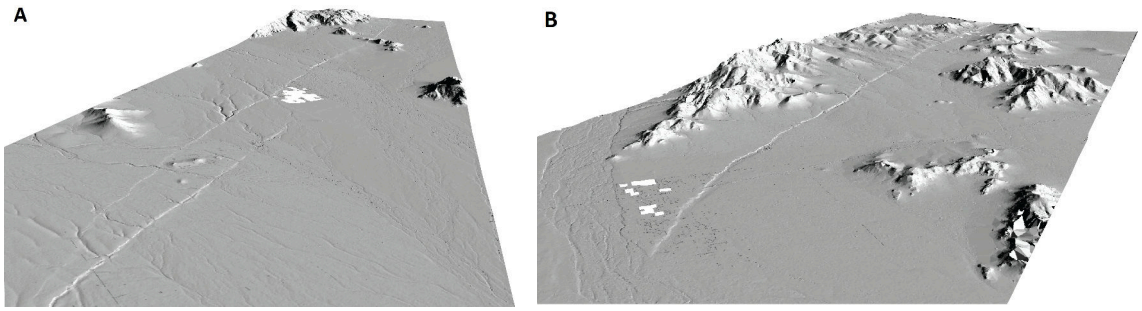

Figure 3.3: (A) Hill-shaded oblique view of the DEM for the southern section of the fault scarp. Looking SE over the cross over zone. (B) Hill-shaded oblique view of the central fault scarp, including Hebron farm. Looking to the SE from the Tsauchab river. The fault scarp is clearly visible as a light grey line on both images.

Figure 3.1 shows the final product of the filled DEM as well as some of the DEM products that were produced. The slope map (Fig. 3.1 IV) is particularly useful for mapping the total extent of the surface rupture. The fault scarp appears as a clearly defined yellow line, with a total of 45 km km of exposed fault scarp.

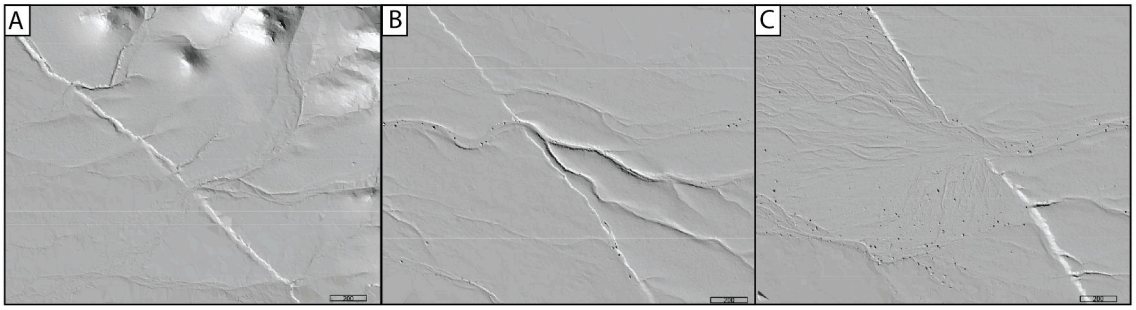

Figure 3.4: Close up views of the DEM close to the fault scarp.

Figure 3.4 A shows how the DEM handles areas of higher topography while Fig. 3.4 B exhibits some of the finer detailed features. The river visible on Fig. 3.4 B has been clearly incised on the north eastern, up-thrown block. Individual shrubs and bushes are visible along and near the stream channel. Figure 3.4 C shows an alluvial fan which has been deposited on the down-thrown block.

3.2 Sediment Map

The following map (Fig. 3.5) was produced using various spectral band combinations of the multi-spectral Worldview-3 imagery. Most of the field area is covered by the Karpfenkliff conglomerates, although there is some outcrop of the Sinclair Group basement rocks. These outcrops are generally areas of high topographic relief. Despite this, there is some variation in lithology of the clasts and cements that comprise the Karpfenkliff group. In addition, this unit has been reworked in several instances where alluvial fans have formed on the hanging wall of the fault.

Of the mapped units (Fig. 3.5), Surface 1 appears to be the oldest as it is overlain by its neighboring surfaces and appears to have a distinctive desert varnish and thus low reflectance. Surfaces 2, 3 and 4 also show some amount of desert varnish, albeit less than Surface 1.

The southern fans are comprised of alluvial fans which have been deposited on the hanging wall of the fault. It is therefore reasonable to conclude that they were formed after the scarp was formed (Fig. 2.14) due to the creation of depositional space after the fault ruptured. The alluvial fans located in the center of the fault, between the Hebron Farm and the Hyas Farm (Fig. 3.6), are older than the southern fans. This is because the first two fan generations in this area (Central Fans 1 and 2) have been offset by the fault, implying that they existed before the scarp was formed. The latest generation (Central Fans 3) may be temporally equivalent to the Southern Fans as they are also deposited on the down-thrown block. The river sediments associated with the Tsauchab are the youngest sediments, along with a palaeo-flood plain which is located just to the north of the Hebron farm.

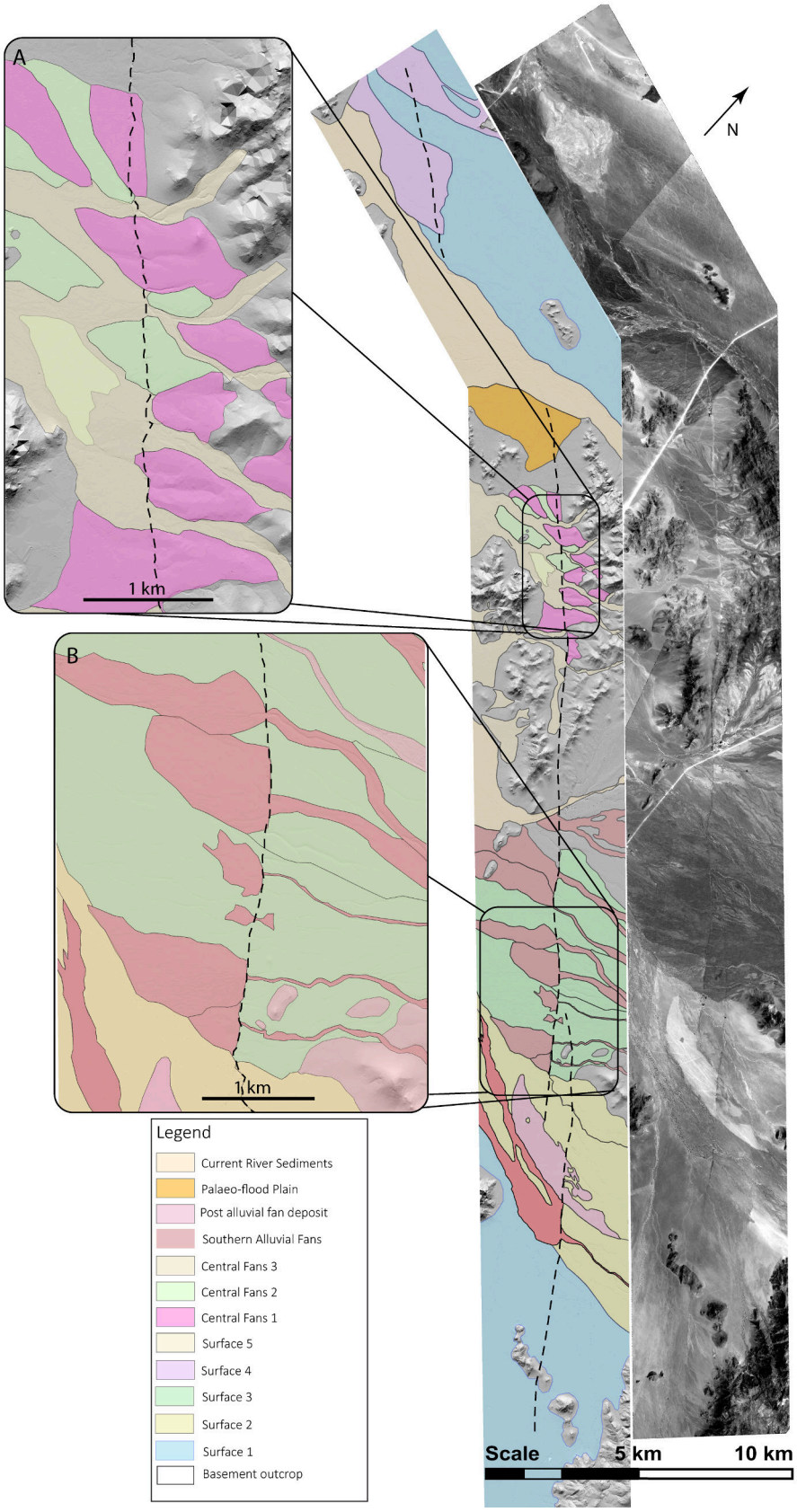

Figure 3.5: A map of sediment packages mapped overlying a hill-shaded DEM image. A satellite image layer of the area is provided to the right of the map. (A) Generations of alluvial fans on Hebron Farm. (B) Post-fault alluvial fans on the Hyas Farm.

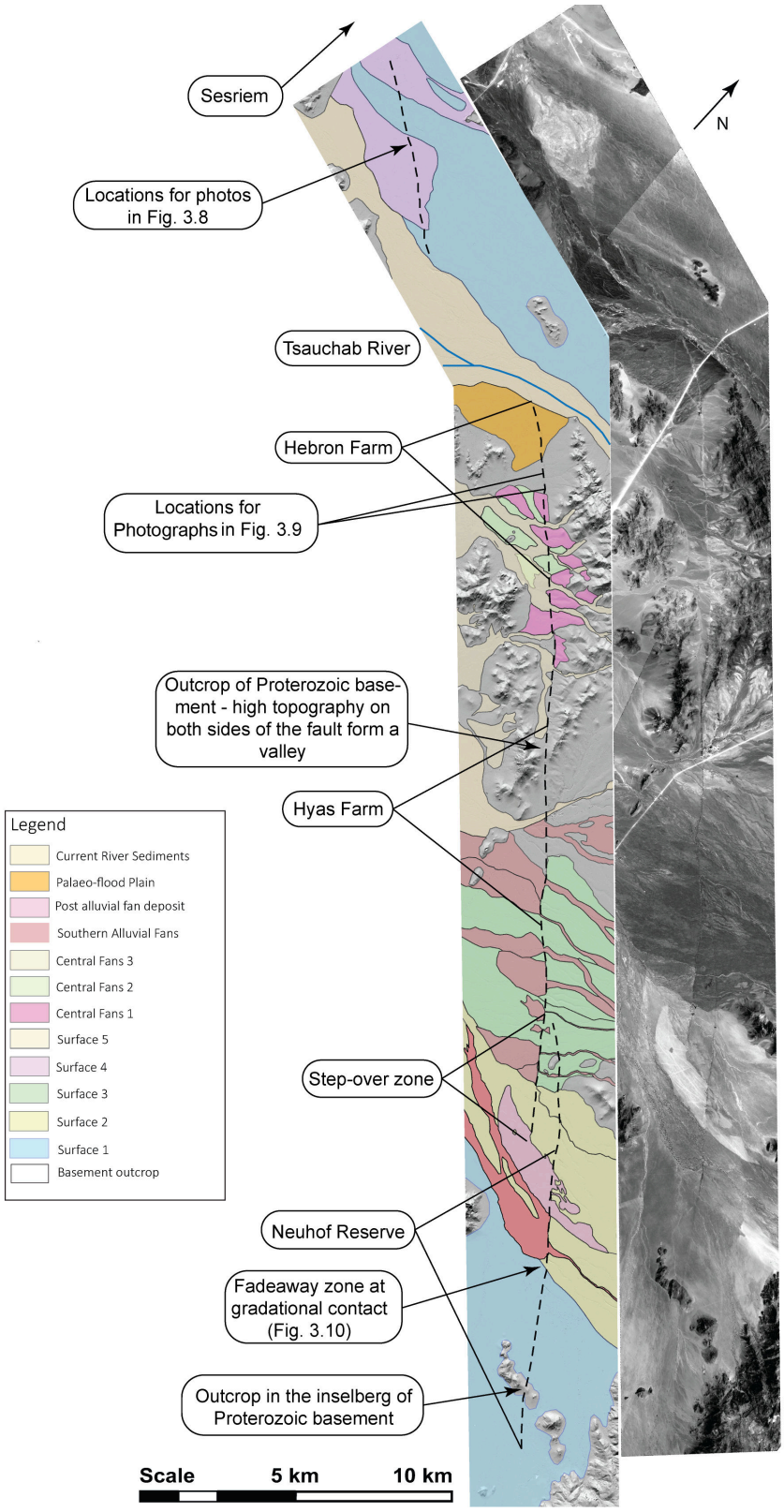

Figure 3.6: Location map for sites of interest along the fault scarp

3.3 Scarp Morphology

3.3.1 Relationship to lithology

The Hebron fault scarp changes in height, width and appearance along the length of the fault. The previous study by White et al. (2009) described and defined three different scarp categories. These categories were named C1, C2 and C3. In addition, they were given descriptive names of juvenile, intermediate and mature respectively. In this study, these scarp types will be referred to as sharp, intermediate and diffuse (Fig. 3.7). This is to prevent an association between the age and the scarp morphology. Furthermore, White et al. (2009) describes the scarp only in areas where the fault runs through the calcrete-cemented breccia-conglomerates (White et al., 2009). These descriptions generally do not apply to regions where the bedrock outcrops. For the most part, the scarp is relatively sharp in the areas of basement outcrop, being clearly visible on cross sections and as a dark line in the satellite imagery. The following paragraphs compare my observations of the scarp in the field to the descriptions made by White et al. (2009). The scarp morphology along the fault appears to be controlled by the degree of calcretization present within the geological units that the scarp runs through.

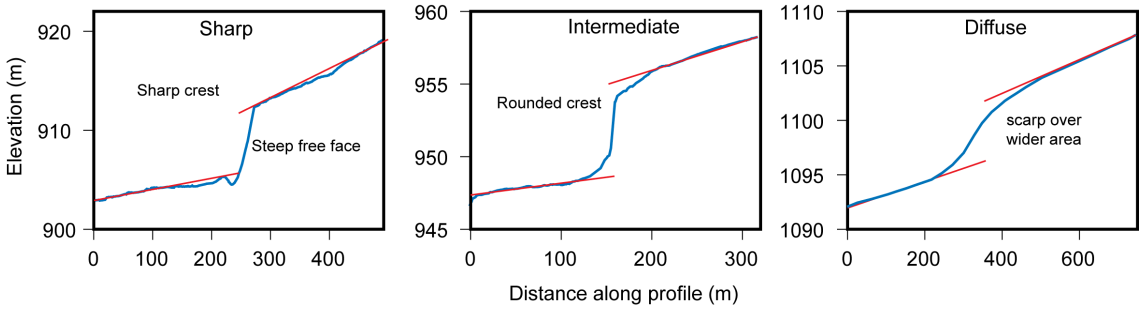

Figure 3.7: Example cross sections for the three scarp morphology categories; sharp, intermediate and diffuse

The scarp height is lowest in the north-western segment of the fault (Fig. 3.6) with values ranging from 1 - 4 m. This section was not included in the description by White et al. (2009), as it did not form a part of their field area. The scarp is sub-vertical here and falls between the intermediate and diffuse categories (Fig. 3.7)

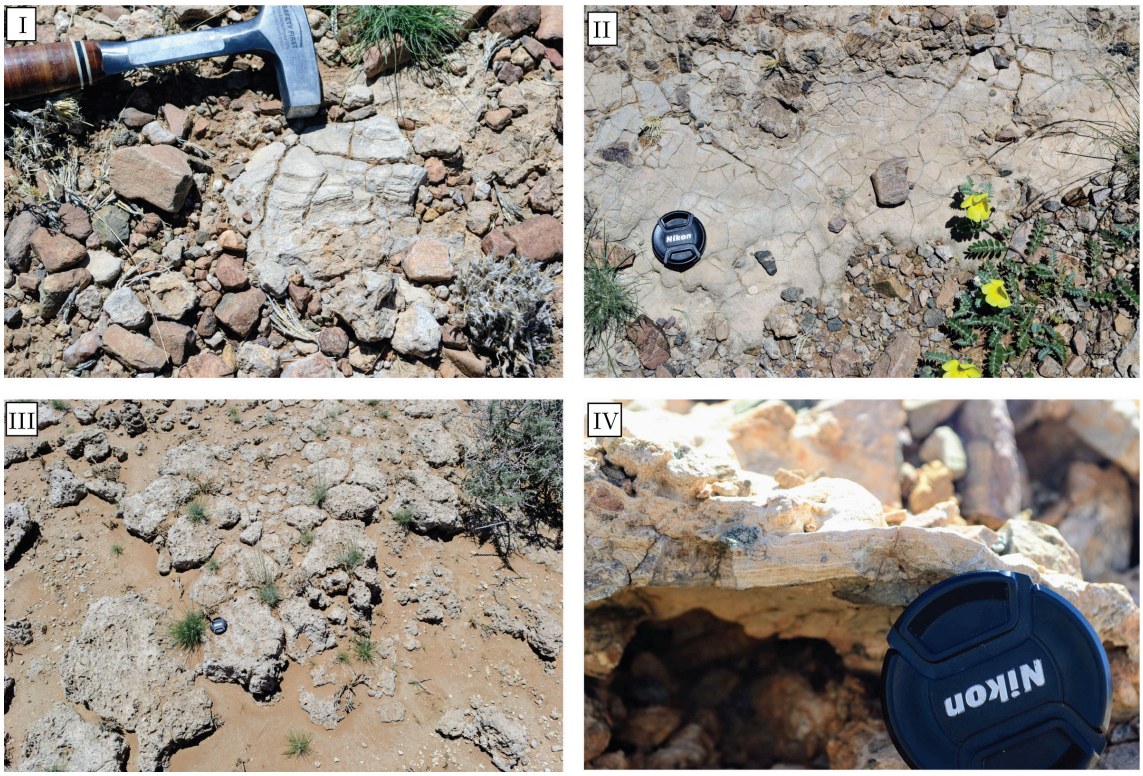

Figure 3.8: Photographs of the calcrete cement and other calcrete features observed.
(I) Dessication-cracks in the calcrete at the top of an exposed calcrete nodule.
(II) Dessication-cracks on the top of a calcrete nodule
(III) Calcrete nodule in situ. This particular nodule is located near the fault in the NW part of the field area.
(IV) Fine-laminations present in the calcrete.

In this segment, the scarp has a dip of $\approx 60°$ to the SW and a width of 10 - 20 m. The fault is running through Surface 1 (Fig. 3.5). In this area, nodules (2-3 m wide and 10 - 20 cm high) of finely laminated calcrete protruded from the ground in several places. The top of the these calcrete nodules have desiccation cracks, suggesting that they formed on a sub-aerial surface (Fig. 3.8 I, II).

The scarp morphology is quite uniform on the Hebron Farm, immediately south of the Tsauchab River (Fig. 3.6) where its height gradually increases as you move further south (from $\approx$ 4 m to 6 m). This section is most closely related to the C1 (White et al., 2009) or sharp scarp. The scarp has a free face, near vertical and in some places is under-cut by erosion (Fig. 3.9 II). The uppermost layer has a large amount of cementation by calcrete/silcrete. The scarp crest is sharp and the down-thrown surface has evidence of debris that has fallen from the crest (Fig. 3.9 I). In several places a small graben has been formed as a result of antithetic faults on the

down-thrown surface (Fig. 2.14). The lithology in this area is a calcrete-cemented breccia-conglomerate with angular clasts that have been cemented together by both calcrete and silcrete, although the calcrete is more ubiquitous. This lithology is the Karpfenkliff conglomerate as described by White et al. (2009). The breccia-conglomerate clasts are comprised of Sinclair Group rocks (Hoal and Heaman, 1995) including rhyolites, quartz porphyry granitoids and quartzites. In the areas closer to the Tsauchab channel, there are also clasts of Nama Group sedimentary rocks such as laminated dolomites, limestones and sandstones of the Schwarzrand and Kuibis subgroups (White et al., 2009). The clast shape varies according to the dominant clast lithology with limestone clasts being the most rounded and granite and quartzite clasts being angular. This is in part due to the amount of transport and relative distance from the surrounding mountains and bedrock inselbergs which were the source of these sediments (White et al., 2009). The calcrete cement was visible on both the up-thrown and down-thrown surfaces. Dessication cracks, similar to Fig. 3.8, were also present in the upper 1 - 5 cm of the calcretized sediments. In areas of large accumulations of calcrete, millimeter scale laminations were observed (Fig. 3.8 IV). Furthermore, these laminations were not present throughout the unit. On an exposed section of the calcretized scarp, horizons were evident on the scarp face but laminations were not present on all of these horizons.

The scarp morphology changes 2 km south of Hebron farm house (Fig. 3.6). This occurs within a lithological change where three generations of alluvial fans (the central fans, Fig. 3.5) have been deposited on top of the calcrete-cemented breccia-conglomerate. The scarp becomes less sharp with a more rounded crest and the accumulation of debris on the down-thrown surface is greater. There is still a free face, albeit only on a portion of the scarp. This resembles the description of intermediate scarps made by White et al. (2009) However, the scarp height still continues to increase as you move south. The geological unit is still the Karpfenkliff breccia-conglomerate (White et al., 2009), however, the clast lithology has changed to become primarily Sinclair Sequence lithologies from the hills located to the north, with very few clasts of Nama Group rocks. The clasts are still cemented with calcrete, although there appears to be less cementation between clasts.

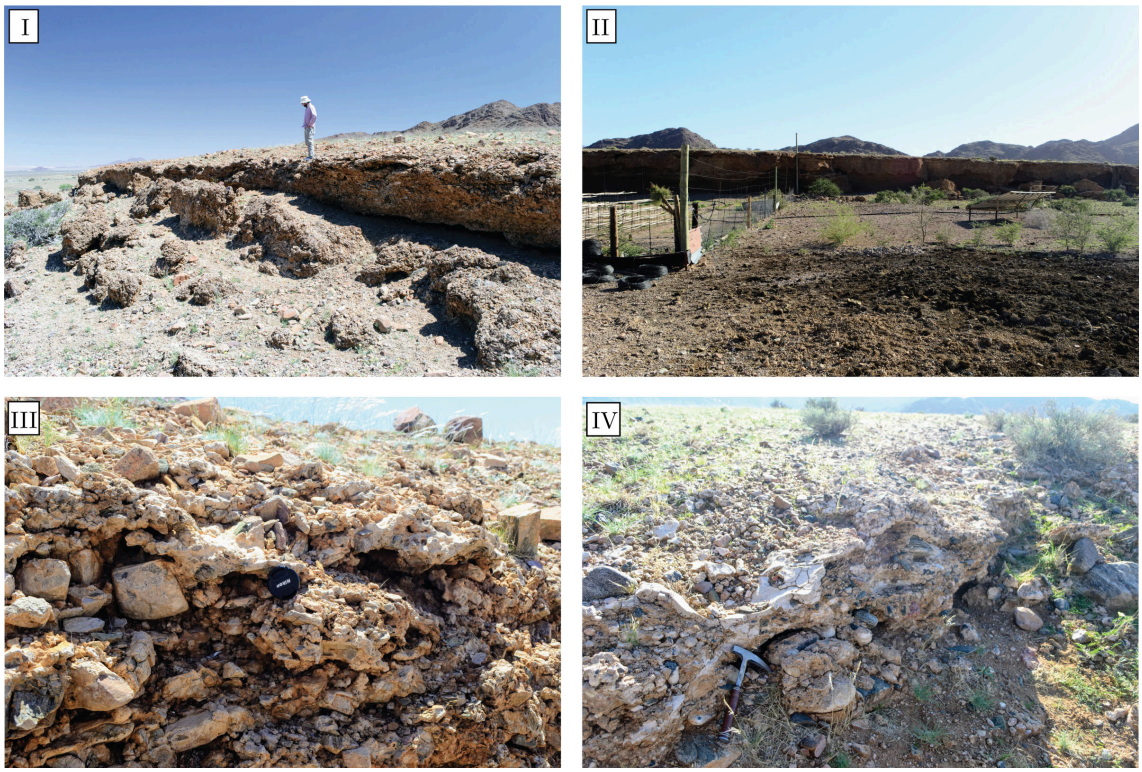

Figure 3.9: Photographs of the fault scarp near the Hebron Farm.
(I) The intermediate scarp morphology. A steep free face is still present although there is also a considerable accumulation of material from the fault crest on the down-thrown surface.
(II) The sharp scarp morphology with a large free face and sharp fault crest.
(III) A close up look at the calcrete-cemented breccia-conglomerate that the fault is cutting through.
(IV) Calcrete-cemented breccia-conglomerate. Note, the amount of calcrete cement varies along the length of the fault.

There are at least three generations of alluvial fans in this area. With at least one of these generations being deposited on the down-thrown surface. The reduced scarp height readings from these post faulting fans (Fig. 2.14) could explain some of the variation in scarp height values observed (Fig. 3.19).

There is an outcrop of the Proterozoic Sinclair Group basement in the center of the fault between the Hyas and Hebron Farms (Fig. 3.6). The scarp in this area is continuous with the scarp running through other units, indicating that the scarp in the calcretized breccia-conglomerates represents a fault plane that extends down into a single basement fault (White et al., 2009). The scarp morphology in the basement rock shows a clearly defined free face with a dip of 70°. The dip appears to be parallel to the bedding planes of the Sinclair Sequence quartzite in

this location. Striations were observed on this face, indicating a dip of 70° and a nearly pure dip-slip vector. The quartzite is brecciated in the region of the fault and it is likely to be an old structure which has been recently re-activated to produce the scarp.

The fault scarp south of Hyas Farm is interspersed with sections (about 2 km long) of the sharp and intermediate scarp types described by White et al. (2009). There are several small, 10 - 50 m wide, grabens on the down-thrown surface formed by antithetic faulting. Additionally, alluvial fans which have been deposited on the down-thrown surface are present — which introduces variation in the scarp heights. The scarp in the step-over zone (Section 3.3.2) was described as diffuse, with a uniformly sloping ramp and a low slope angle of around 15°, by White et al. (2009). These slope values are corroborated by the values calculated using our DEM, although in some sections, with more calcrete present on the up-thrown surface, a free face of $\leq$ 1 m is visible.

South of the step-over zone, the scarp is interspersed with intermediate and diffuse scarp morphologies as the fault continues to run through calcretized breccia-conglomerates. However, within the Neuhof reserve, the lithology changes to a sandy unit (E, Fig. 3.5) without any calcrete cement. The fault scarp goes from $\approx$ 8 m high and relatively steep (60°) intermediate morphology to 2 -3 m high and very diffuse (60 - 80 m wide) within several hundred meters (Fig. 3.10). White et al. (2009) did not observe a scarp in this area, however, a lineation can be traced using the high-resolution Worldview-3 imagery. In addition cross sections taken from the DEM show a diffuse scarp with a slope angle of around 10°. This dramatic change in scarp height occurs at a lithological boundary between a calcrete-cemented unit (F) and a relatively unconsolidated sandy unit (M). Thus, the height of the scarp appears to be controlled by the amount of calcrete present on the offset surfaces. The calcrete being more resistent to erosion allows the fault scarp to be better preserved, so much so that in several places that are highly calcretized the fault scarp is near vertical without a rounded fault crest.

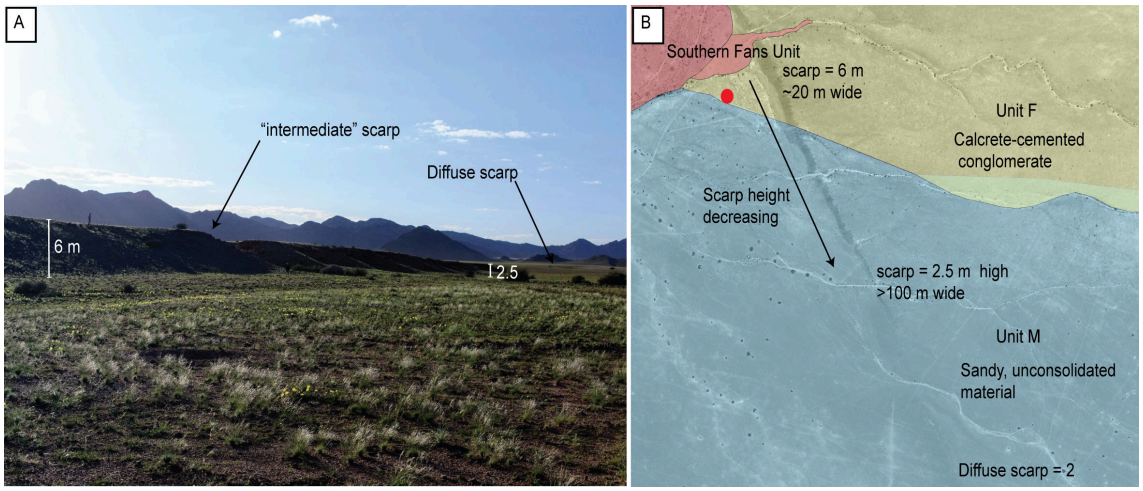

Figure 3.10: Fadeaway zone in the Neuhof Reserve. (A) Photo showing the decrease in scarp height from ≈ 8 m to 2.5 m within several hundred meters. (B) Satellite image with the sedimentary map overlaid of the area.

South of this non-calcretized unit, the fault runs through an inselberg of Proterozoic basement (Fig. 3.6) where the scarp once again displays a clear free face within the basement rock. South of the inselberg the scarp morphology is largely that of the intermediate category grading into the diffuse scarp with slope angles decreasing southwards. Eventually, the fault trace fades away towards the far south of the DEM (Fig. 3.1).

3.3.2 Step-over zone

When looking at the scarp heights individually, the scarp heights are subdued in the area where the scarp segments step-over, near the center of the DEM (Fig. 3.6). Although when the scarp heights for each strand of the fault are added together, the scarp height is very similar to the values found in the scarp directly north and south of the step-over (See Fig. 3.19). Thus there was an equal transfer of slip that was dispersed over the two fault strands and this is in agreement with observations made by White et al. (2009).

3.4 Lateral Offsets

Previous work on Hebron interpreted the Hebron Fault to have a sense of right-lateral motion in addition to normal faulting (Viola et al., 2005). In order to determine if there was evidence of strike-slip motion using our DEM, displacements in the 73 channels crossing the fault scarp were measured. The following figures (3.11, 3.12) show the imagery, with the DEM derived channels being shifted north to allow for comparison with the channels in the imagery. Each of these figures displays numerous channels with no lateral offsets and at least one channel that displays an apparent offset.

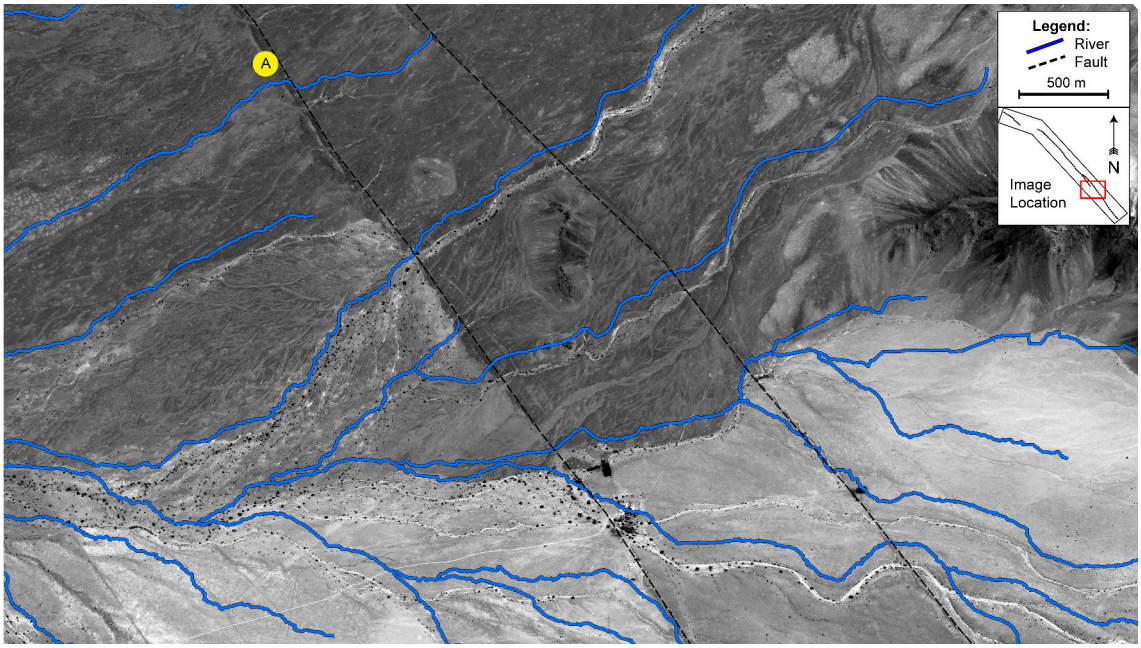

Figure 3.11: River channels for a segment of the field area directly to the south of the step-over zone, see inset at top right. The blue lines, representing the mapped river channels have been shifted to the north by 100 m in order to allow for comparison to be made between the channel extracted from the DEM and the channel visible in the imagery.

In the case of the apparent offset at point A on Fig. 3.11, the sense of offset is sinistral. However, the streams directly to the south of A show no sense of motion. There is a possibility that the stream at A changed direction as a result of the small graben creating a new lower level along which the stream could flow. The formation of this graben may be due to the presence of a parallel antithetic fault, causing the block between the two faults to be down-thrown (Fig. 2.14) creating a shallow

trough which may divert channels and cause pooling, forming ponds during times of rainfall.

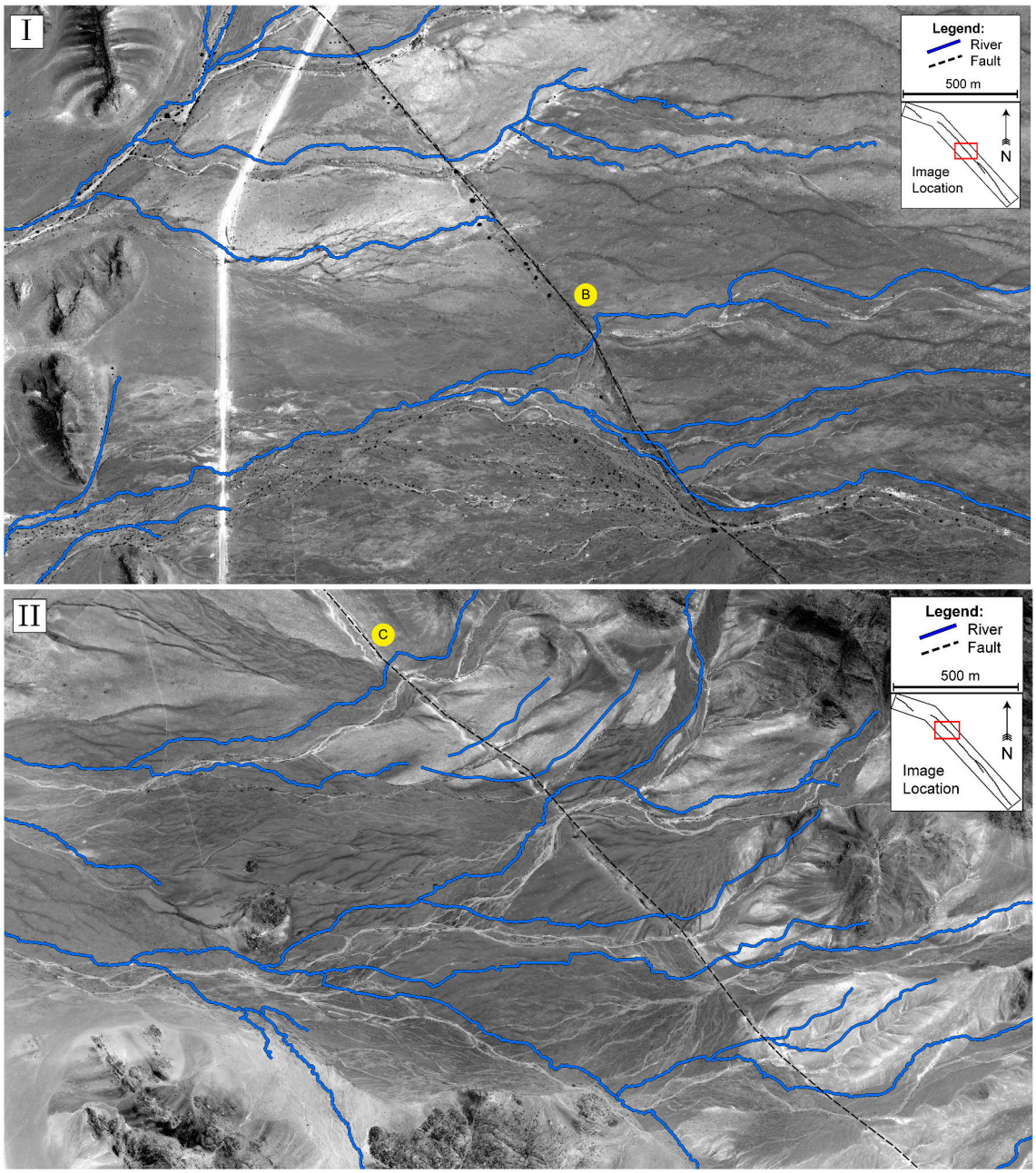

Figure 3.12: (I) River channels that cross the fault scarp in the central zone of the field area, in the Hyas Farm (See inset). There is one channel, B, that appears to have been offset but this is a change in channel direction as a result of an alluvial fan deposited on the down-thrown block. (II) River channels that cross the fault scarp in the central part of the field area, south of Hebron Farm (See inset). Channel C appears to have some horizontal offset, however, the channels directly to the south show no such movement. The apparent offset may be due to a change in channel on the down-thrown side of the fault. The blue lines, representing the mapped river channels have been shifted to the north by 100 m in order to allow for comparison to be made between the channel extracted from the DEM and the channel visible in the imagery.

In the case of point B (Fig. 3.12 I), the sense of motion is dextral, however, once again the rivers in close proximity to point B show no sense of motion. This is a case where the river has changed directions after the fault scarp formed as a result of an alluvial fan being deposited on the down-thrown surface. The offset in point C (Fig. 3.12 II) appears to occur behind the fault scarp and thus may not be an offset but rather a change in stream direction due to some other factor.

The lateral offsets observed on stream channels are plotted on Fig. 3.13. This plot shows a mix of both sinistral and dextral senses of motion, with little systematic preference in the amount or type (sinistral or dextral) of offset. Furthermore, these offsets are often surrounded by channels of similar maturity that do not display any offsets. The implication is that the offsets in Fig. 3.13 are attributed to channels changing course on the down-thrown surface, often as a result of the deposition of an alluvial fan, rather than the effect of horizontal motion on the fault plane.

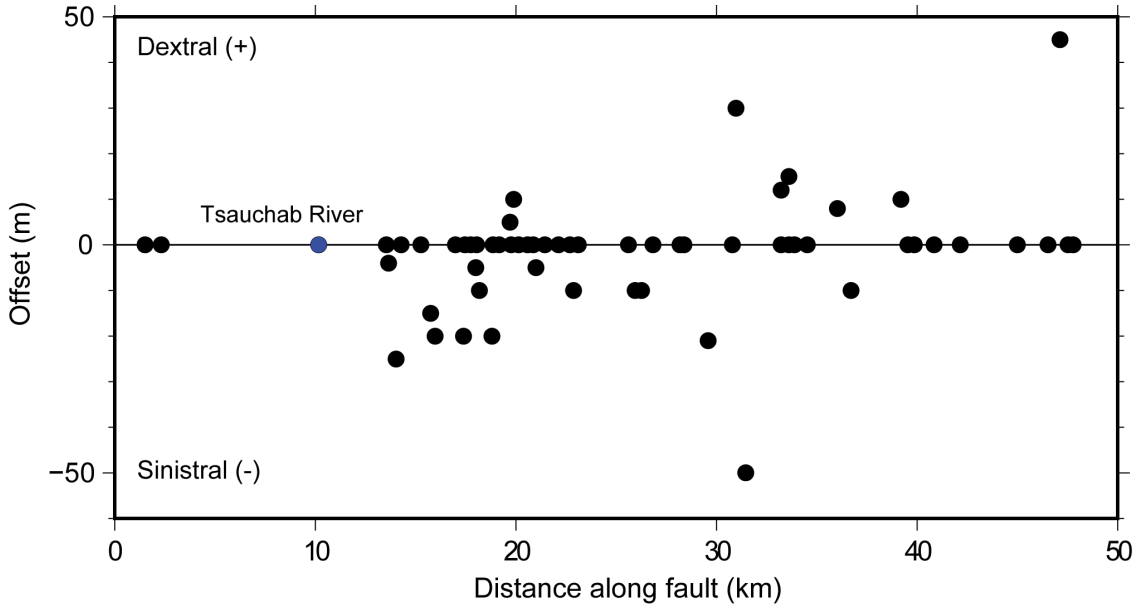

Figure 3.13: Apparent offset measured on channels crossing the fault scarp within the DEM area. Positive offsets infer a dextral sense of motion while negative values infer a sinistral motion. The channel of the Tsauchab river is shown in blue.

The 13 channels that were clearly on a post-faulting alluvial fan (like B on Fig. 3.12) were removed from Fig. 3.13. The plot starts measuring distance along the fault in the NW segment near Sesriem. The majority of the channels show no offset and so plot along the zero line in Fig. 3.13. However, there are several channels

with apparent offsets, the majority of these are small but there are several larger offsets, the largest being ≈ 50 m. These apparent offsets are unlikely to be the result of strike-slip movement on the fault. For one, the channel displacements reflect opposing senses of motion, sometimes changing from one channel to the next. The mean value of these apparent offsets is 1.6 m, with a sinistral sense of direction. The standard deviation was 12.33 m. The large (≈ 50 m) apparent offsets are likely due to the fault, and the associated small graben, changing the course of several streams.

Variations in strike

The north western segment of the fault scarp, south of Sesriem (Fig. 3.6), follows a different strike (138°) to the other fault segments (125 - 130°)(Fig. 3.14). This segment was not included in the study by White et al. (2009), presumably because the fault scarp is much lower and less continuous in this area. The segment appears to be comprised of smaller fault segments that have a left stepping geometry suggesting a component of right-lateral slip due to the different strike angle.

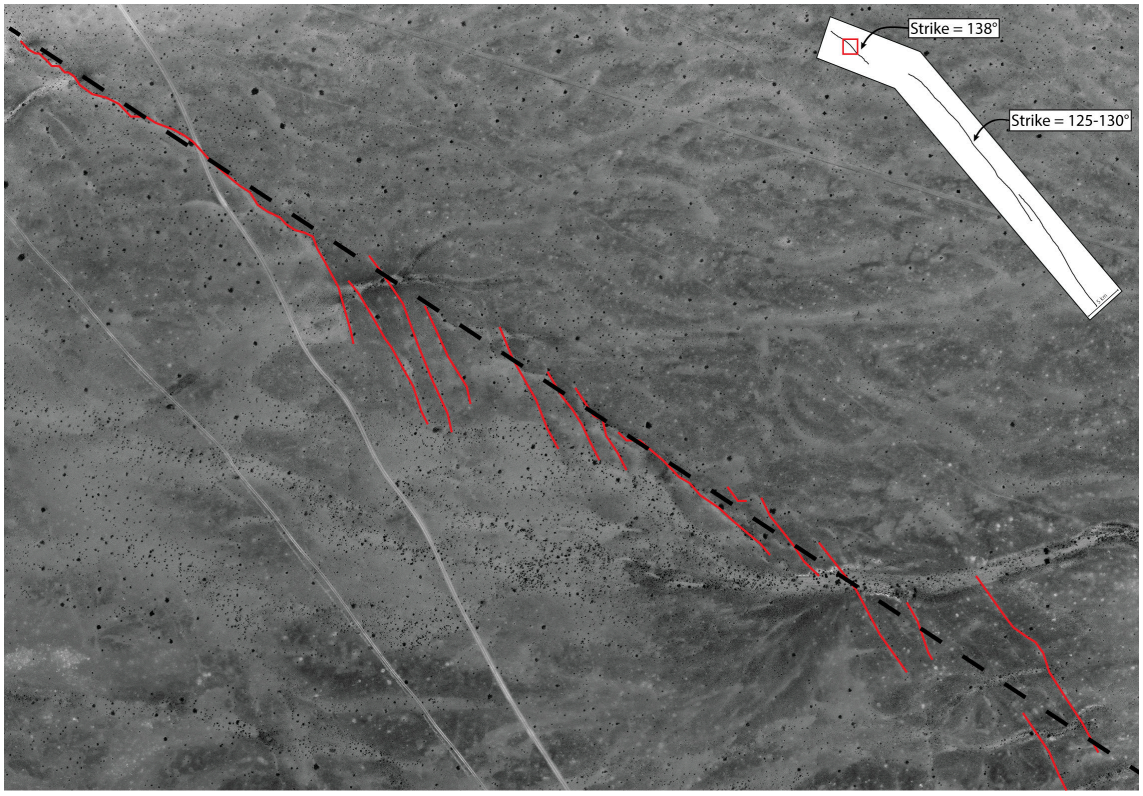

Figure 3.14: Discrete scarps (red lines) in the central area of the NW fault segment instead of a continuous fault scarp (dashed black line), this pattern is characteristic of strike-slip motion

From the middle of this segment, the scarp does not follow a single continuous line but rather several smaller discrete lines that have a left-stepping geometry (Fig. 3.14). This continues until the scarp is cut off and hidden by the Tsauchab river channel.

3.5 Knickpoint Analysis

The elevation profiles for 23 streams that cross the fault scarp were extracted and used in the knickpoint analysis. This included 6 rivers which run through the step-over zone and pass through both fault scarps. The remaining 17 river channels were distributed along the length of the fault scarp as much as possible (Fig. 3.15). There are considerably fewer stream channels in the far south and north of the fault scarp, although since the scarp is also lower in these regions, any knickpoints present may be harder to detect.

For the 6 streams that run through the step-over zone, thus crossing the fault scarp twice, a maximum of 2 knickpoints were found. For the other 14 streams, there were only 2 cases where two clear knickpoints were discernable, these were streams R (Fig. 3.16) and Q (Fig. 3.15). These streams are located next to one another in the southern section of the DEM, near the fadeaway zone (Fig. 3.10). The remaining 12 streams all contained a single knickpoint. In 5 of these cases the knickpoint had not migrated very far from the fault scarp (G, I and J in Fig. 3.15 and K and W in Fig. 3.16). Fig. 3.15 shows 6 river profiles arranged from north to south and Fig. 3.16 shows three profiles from the step-over zone as well as three additional profiles from the southern section of the fault.

Minor knickpoints can be seen on many of the longitudinal profiles. These small knicks are interpreted to be due to noise on the DEM. This may be due to the presence of small bushes, shrubs or boulder in the stream channel, that create a bump on the surface of the DEM which may have been included when extracting the river profiles. These features cause a positive and negative change in slope value (Δm, the red line on Fig. 3.15 and 3.16). This is in contrast to modelled knickpoints

which show only a positive change in slope 2.2.3. The positive and negative slope change signals for each profiles have been marked as green triangles on Fig. 3.15 and 3.16 to indicate anomalies that are due to trees, boulders and imperfections in the DEM.

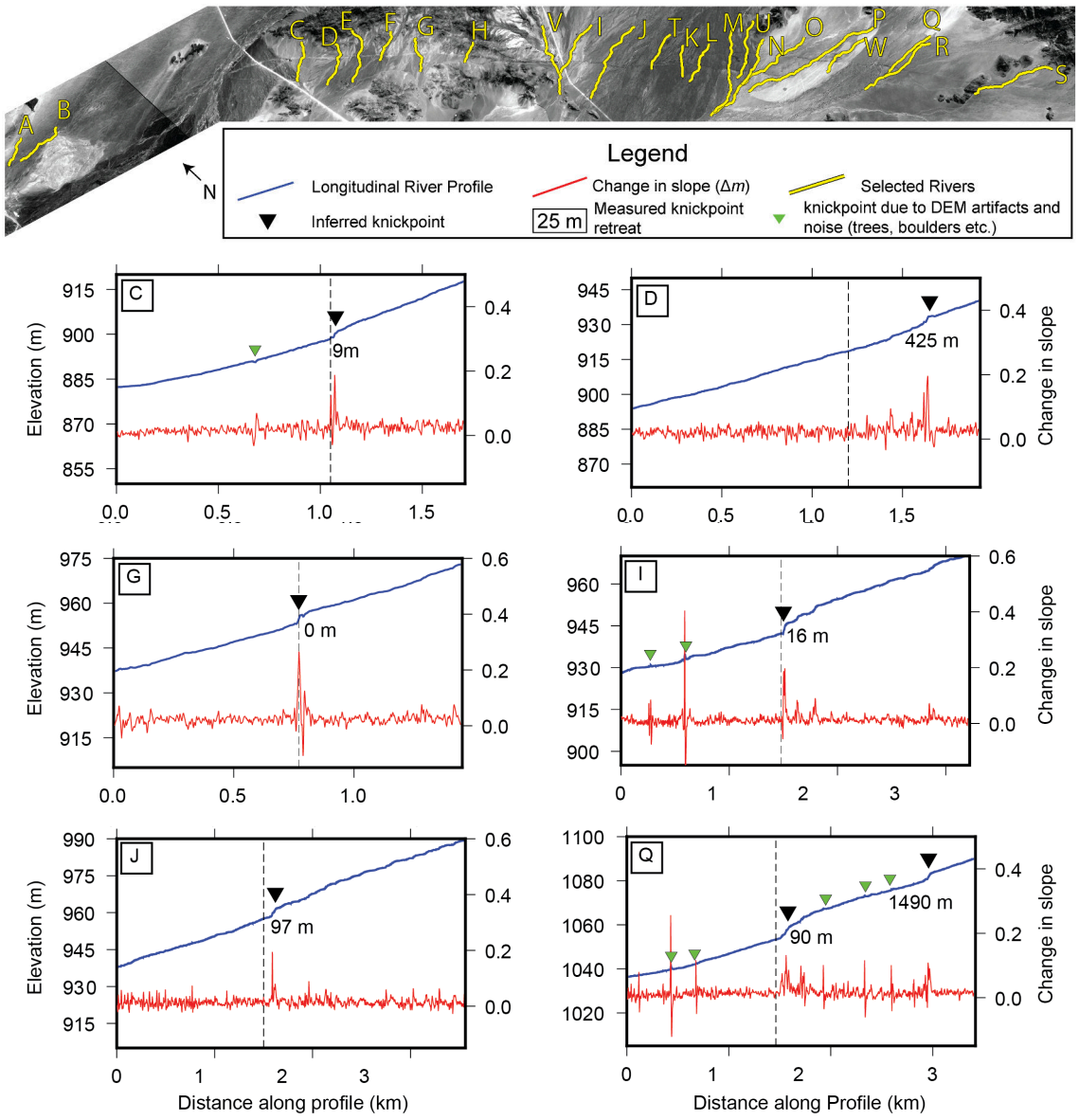

Figure 3.15: Longitudinal stream profiles for 6 of the selected streams. The profiles are shown in blue and the change of slope is displayed in red. The dotted black line indicates the approximate location of the fault scarp. The profiles show some migration of the knickpoint backwards away from the scarp, this is displayed near the knickpoint which is marked by a black inverted triangle. The green inverted triangles are apparent knickpoints due to trees, boulders or imperfections in the DEM.

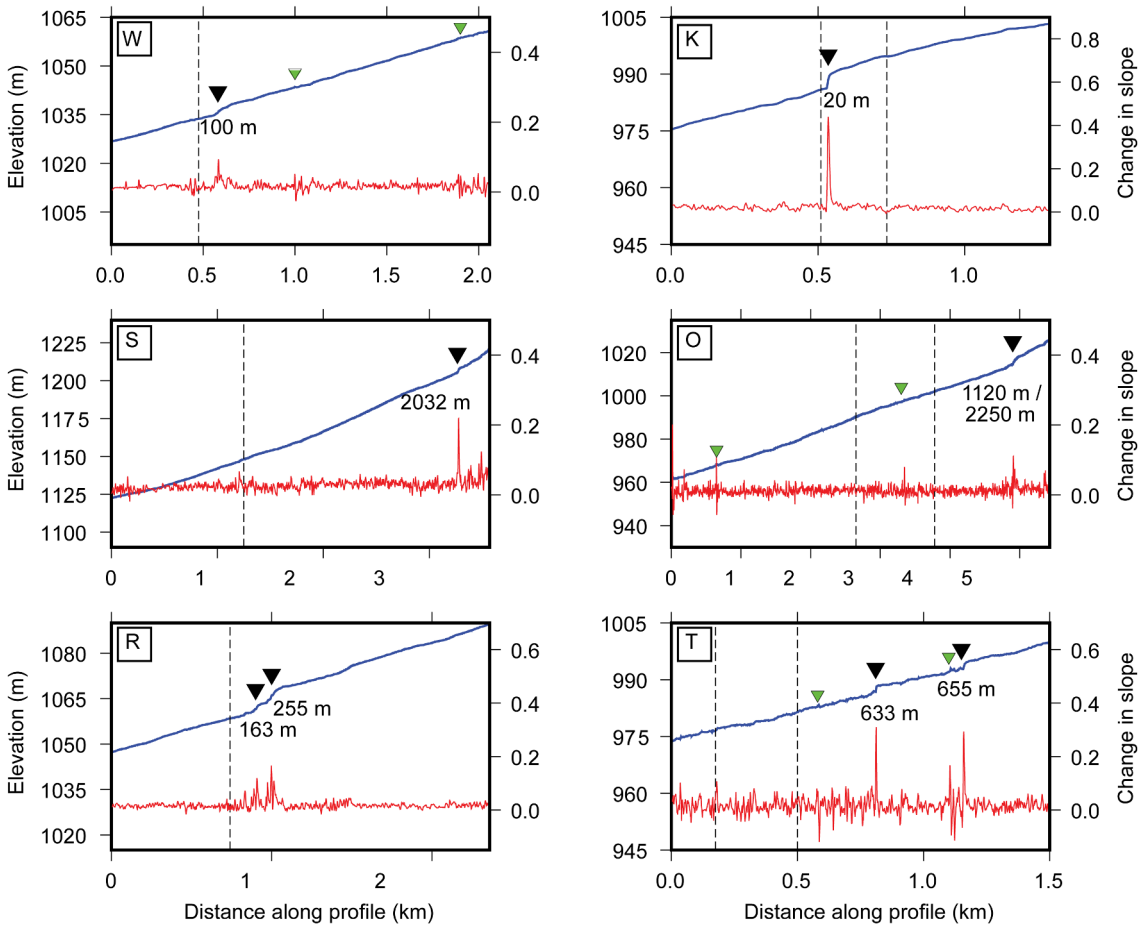

Figure 3.16: Longitudinal stream profiles for 6 more of the selected streams. Three of the streams displayed (K, O and T) run through both fault scarps in the step-over zone. The profiles are shown in blue and the change of slope is displayed in red. The dotted black line indicates the approximate location of the fault scarp. The profiles show some migration of the knickpoint backwards away from the scarp, this is displayed near the knickpoint which is marked by a black inverted triangle. The green inverted triangles are apparent knickpoints due to trees, boulders or imperfections in the DEM.

The plots for all 23 profiles can be found in Appendix B.

3.6 Vertical Offsets

Examples of how the Matlab function performed can be found in Figure 3.17. The function was run for a total of 160 cross sections, at an average spacing of 250 m along the fault. In most cases, the fault scarp was clearly evident on the cross sections. Most of the up-thrown and down-thrown surfaces were also near planar and thus the linear regression worked well when fitting the planes. However, in some cases the fitted planes were not that well aligned with the surfaces that they were supposed to

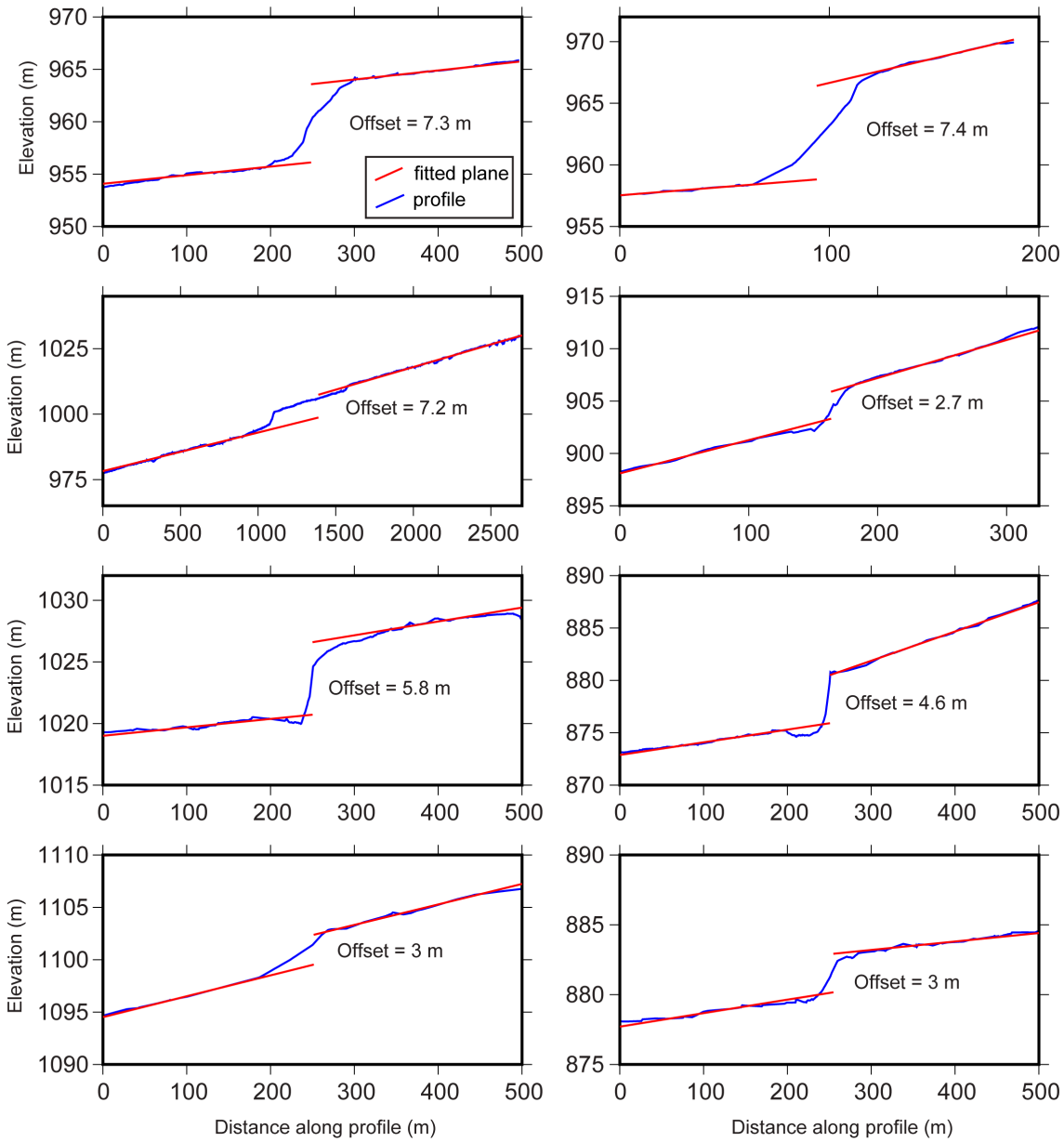

Figure 3.17: Example cross sections. The blue lines are the cross sectional profiles extracted from the DEM. The red lines are the fitted planes to the down-thrown and up-thrown surfaces. The location of each cross section is shown on the minimap to the left of the plots.

be representing (Fig. 3.18). These cases were assessed visually to classify whether the measured offset was either an under-estimate or an over-estimate. Figure 3.18 displays examples of an under and over-estimated scarp height.

From the 160 measurements a subtotal of 112 were good measurements, 35 were under-estimates and 13 were over-estimates. Overall, the function worked fairly well with 70% of measurements being classified "good". The good estimates were

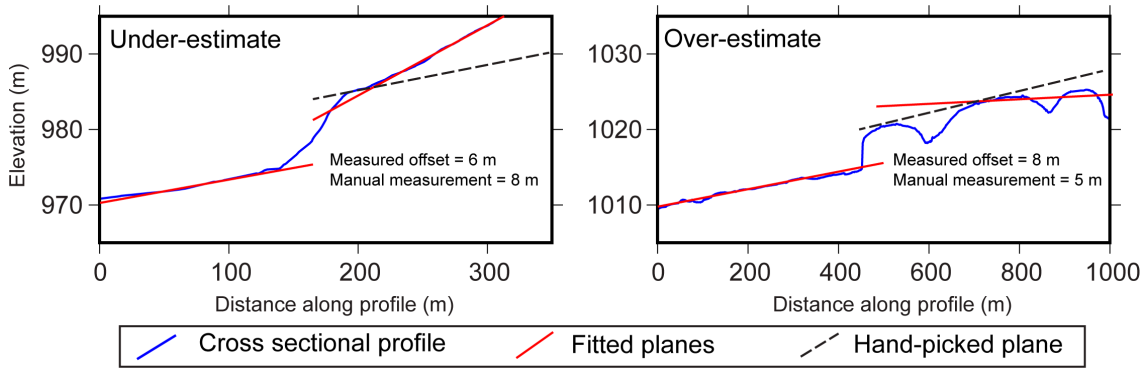

Figure 3.18: Example cross sections that were categorized as an under-estimate (left) and an over-estimate (right)

used to calculate the slip on the fault, See Appendix D for plots of all these cross sections. The cases where the scarp height was poorly estimated were generally areas where compromises had been made in order to place a cross section in that position. In other words, some of the criteria used to select the cross section were not completely fulfilled (Section 2.3.1). A plot of the scarp height results of the MATLAB `cross_section` function with distance along the fault can be found in the top panel of Figure 3.19. The bottom panel displays the slip values associated with these scarp heights that were calculated assuming a fault dip of 60°. The average value for the good estimates of scarp height was 5.03 m with a standard deviation of 1.51 m. The maximum value was 8.86 m while the 95^{th} and 90^{th} percentiles of the good estimates were 7.67 m and 7.22 m respectively.

Slip Distribution

The slip values were calculated from the good estimates of scarp heights, with several assumptions of dip angle. The results of which are plotted on Figure 3.19. The scarp heights were taken as the pure vertical component of the slip, i.e. the heave. Assuming a fault dip of 60°, the average slip value was 5.81 m with a standard deviation of 1.82 m. The maximum, 95^{th} and 90^{th} percentile values were 10.02 m, 8.86 m and 8.34 m respectively.

The distribution of the scarp heights and subsequently, the slip values, fit a single arc shaped rupture (Fig. 3.19 B). The values towards either end of the fault are the lowest, the northern edge has the lowest values overall. These measurements

increase as you approach the central region to eventually reach a maximum roughly in the middle of the fault. The curve displayed in Fig. 3.19 B is a sum of sine curve which fits the upper limit of the slip values found along the fault. A sum of sine curve fits a line to periodic functions according to the number of terms (n). For the slip distribution on the Hebron Fault, n was equal to 1 as the slip values could be constrained by a single arc — rather than two or more.

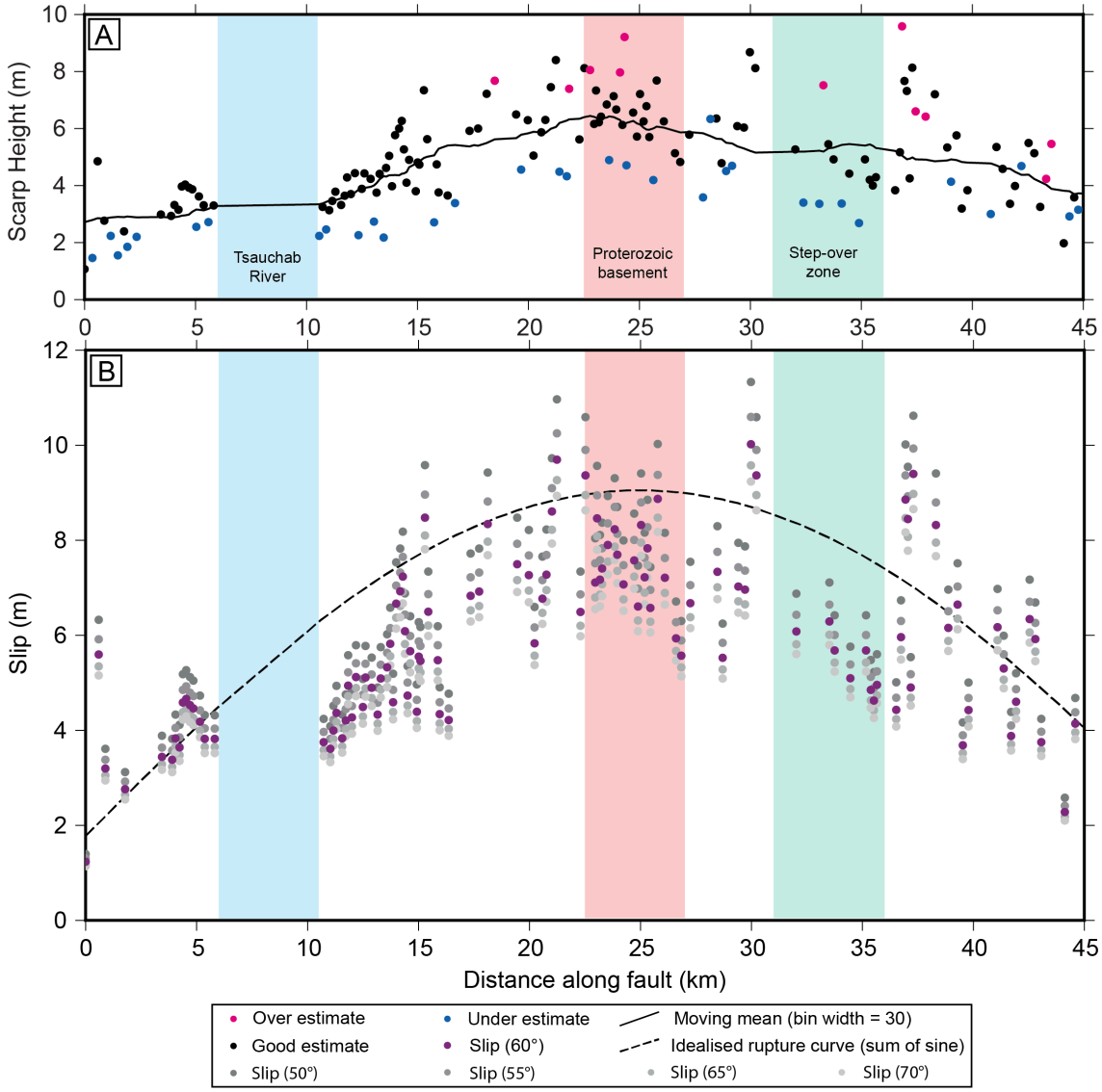

Figure 3.19: (A) Scarp heights as measured from cross sectional profiles along the length of the fault. The measurements start in the NW of the DEM and moves SE. The measurements have been categorized by visual examination as either an under (blue), over (pink) or good (black) estimate of scarp height. The black line represents the moving mean for these scarp heights with a bin width of 30 values. Furthermore, the locations of various places of interest have been highlighted with different colours. (B) This plot shows the slip calculated from the scarp heights using fault dips of 50 - 70°. The dashed line represents an idealized rupture curve - note that despite some variability the slip values are well constrained by this curve.

There are no measurements where the fault scarp runs through the Tsauchab River channel, because the river has eroded through the fault scarp completely. The measurements taken where the fault scarp cuts through the exposed Proterozoic basement rocks, as well as the step-over zone, seem to have the same magnitude and variation in values as the other measurements that are located near to these zones.

3.7 Dip Calculation

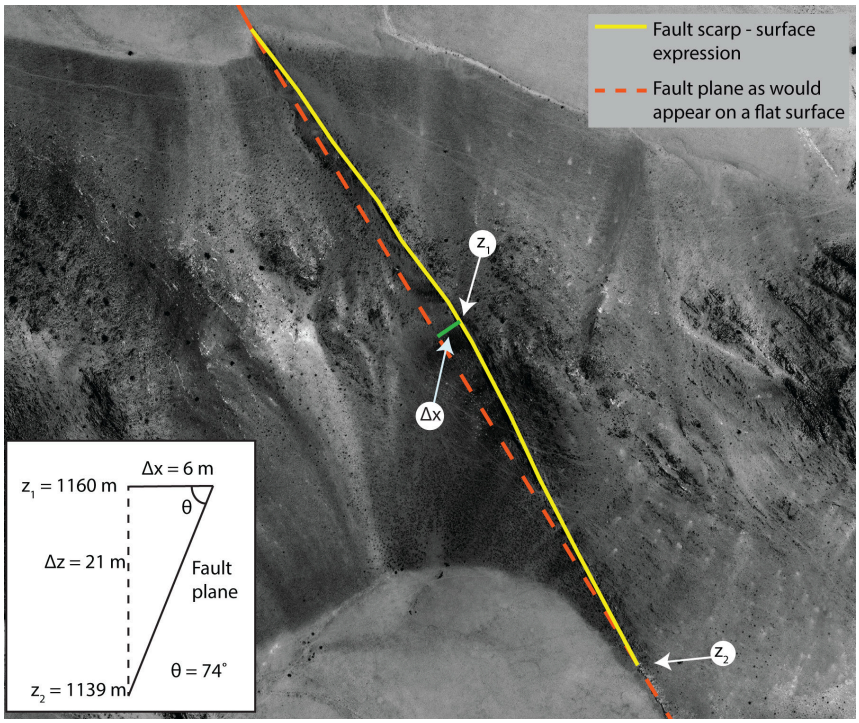

Figure 3.20: Calculation of fault dip from satellite imagery

The dip of the fault near the surface was measured to be dipping at 74° to the south west. This measurement was taken using the satellite imagery on a inselberg of Sinclair Group basement within the Neuhof Reserve (Fig. 3.6). The measurements of horizontal (Δx) and vertical (Δz) differences can be found in the bottom left corner of Figure 3.20. This is in agreement with the values of 70° - 75° with the same dip-direction, obtained from measurements taken from striations in the exposed Sinclair Group quartzites to the north of the Hyas farmhouse.

Discussion

4.1 DEM Quality

4.1.1 Comparison to other studies

This study produced a DEM with a 0.5 m cell size from stereoscopic, panchromatic Worldview-3 satellite imagery with a resolution of 0.33 m. This allowed for sub-meter measurements to be made on the Hebron fault scarp. Other studies of fault scarps have used a variety of DEMs with resolutions ranging from 12 m (Hodge, 2018) to 1 m (Bi et al., 2018; Cochran and Spotila, 2017) that were derived from several different methods. I believe this is the first DEM to use WorldView-3 imagery in order to study a fault scarp. Namibia makes a good case study because the arid climate and low erosion rates can be expected to preserve the record of ancient fault ruptures well.

The 12 m resolution DEM used by Hodge (2018) was the commercially available TanDEM-X 12 m, purchased from the German Aerospace Center (DLR). This DEM and other global DEMs, such as the SRTM (Shuttle Radar Topography Mission), have been used in geomorphological studies of large areas, for which producing high-resolution DEMs may prove too expensive and difficult to store. The vertical resolutions of these DEMs range from 2 m for Tan-DEM X (Zink et al., 2014) and ca. 10 m for SRTM (Gorokhovich and Voustianiouk, 2006). This, in addition with their fairly large cell sizes, imply that any measurements made from these models come with a large amount of uncertainty. As such, determining the height of a fault scarp with varying morphology can prove difficult when using these lower resolution DEMs (Hodge, 2018). Lower resolution DEMs can be useful in tectonic geomorphological

studies, they are often used to identify faults and fault-linkage features over large areas (White et al., 2009; Hodge, 2018).

Other studies of fault scarps that have used satellite imagery to produce DEMs include Hodge (2018); Bi et al. (2018); Grützner et al. (2017); Middleton et al. (2015) and Zhou et al. (2015). Among satellite-derived DEMs, the DEMs derived from Worldview-3 satellite imagery have some of the highest resolutions, due to its very high-resolution panchromatic imagery. The accuracy of DEMs derived from these images is also good, with an absolute vertical accuracy of 2.61 m and a standard deviation of 0.49 m without GCPs. This is significantly improved to 0.27 m vertical accuracy and 0.36 m standard deviation by including 5 GCPs (Hu et al., 2016). In this study, we estimate that the vertical accuracy produced here is similar to this, as a minimum of 5 GCPs were included for each scene (Fig. 2.6).

DEMs obtained from LiDAR acquisitions can have much higher resolutions than that available from satellite imagery. Vadman (2019) produced a point-cloud with a density of 11.21 pts/m^2 for an area of 80 km^2. This is significantly higher than the point density of 0.5 - 1 pts/m^2 from our point-cloud. Similarly, DEMs produced using drone photogrammetry are also a higher resolution than satellite-derived DEMs. In smaller areas of interest, the resolution of DEMs produced by drone photogrammetry may be equal to that of DEMs produced by LiDAR surveys, at significantly less cost.

4.1.2 Advantages and disadvantages of satellite imagery

Generating DEMs from satellite images can vary significantly depending on the imagery used, such as GEO-EYE, Pleiades or Worldview-1, 2 and 3 etc. As the resolution of the imagery varies between these satellites, so too would the quality of the DEM produced. However, as VHR (very high resolution) satellite imagery becomes more accessible (Hashim and Deilami, 2011), the quality of DEMs produced should also improve, with the range in errors decreasing. A factor that must be considered is the cost of this imagery. At present, VHR satellite imagery is only commercially available and the cost of this scales with the size of the area required. Additional

complications in using satellite imagery include the storage and processing of large data-sets (Hodge, 2018). As such, lower resolution imagery is still used in order to mitigate some of these problems, especially when covering large areas.

Unlike satellite imagery, LiDAR surveys are able to easily classify the points obtained by looking for latest returns in a pixel and can thus remove the vegetation from the surface of the DEM (Haugerud et al., 2003). Satellite photogrammetry based DEMs can also remove the effect of vegetation, but this requires laborious manual DEM editing (Höhle, 2013). This is sometimes necessary in relatively vegetated areas where trees and shrubs may obscure and hide parts of the surface. However, the Hebron fault is located in an arid area, with very little ground cover. Thus, with minimal vegetation obscuring the fault, Hebron provided an ideal case for the use of a photogrammetry derived DEM. A LiDAR survey would have yielded a higher resolution DEM, however, this was not necessary to carry out the analysis and would have been considerably more expensive.

A drone photogrammetry project would be able to produce similar resolutions to LiDAR at a much lower cost (Eisenbeiss, 2009). Although, when using drone photogrammetry over large areas, significant time in the field is needed in order to take the hundreds to thousands of photographs required. Additionally, flying a drone in part of the field area would have been very difficult due to strict Namibian legislation concerning UAVs, exacerbated by the presence of a small airport located very close to the northern segment of the fault scarp. An alternate image source that was not available was aerial photography. The Namibian National Spatial Data Infrastructure only has aerial photographs of urban areas available to the public. Unfortunately, the Hebron Fault is located well away from these urban centers.

While there were some issues with voids in the final product (due to non-vegetated, flat, low-contrast surfaces on which few points were generated) this did not hinder the analysis in a significant way. A possible improvement could have been to use a drone to produce small DEMs for each of the areas with voids. This would allow for a more complete coverage throughout the field area. Furthermore, higher

resolution DEMs could have been produced for areas of interest along the fault scarp — allowing for more detailed geomorphology analysis. However, this was not acted upon due to legislative barriers. This study's DEM has a similar resolution to other studies of fault scarp geomorphology. Additionally, the DEM produced in this study has higher resolution and lower vertical error than of DEMs produced from other VHR satellites due to the use of WorldView-3 imagery.

4.2 Variations in strike

The north-western segment of the fault scarp, located north of the Tsauchab river, follows a slightly different strike (138°) than that of the other scarp segments (125-130°, Fig. 3.14). This right-lateral stepping behaviour is typically associated with strike-slip movement, most likely due to the non-parallel orientation of the strike in this area with the rest of the fault.

If it is assumed that the Hebron fault is a pure normal fault, with the slip vector perpendicular to the mean strike in the main segment, the amount of strike-slip motion expected for this limb can be calculated. The mean strike of the main segment of the fault is ≈128° and the average slip (s) is 5.81 m (Section 3.6). The slip would have a direction of 38° ,assuming a rake of -90° for pure normal slip. The horizontal (strike-slip) component of the slip (s_{xy}) can then be calculated using $s_{xy} = s.cos(\theta)$. The strike slip component was thus calculated to be 0.7 m for this NW segment, with a dip-slip component (vertical component of slip, s_z) of 5.7 m.

It may have been similar features to this that led to the interpretation by Viola et al. (2005) that Hebron has a right lateral component. However, we only observed this behaviour in a relatively small portion of the north western segment, within an area of a different strike to the main scarp segments.

4.3 Number of events

If the fault scarp was created during a single event, this would represent an earthquake much larger than the maximum magnitude that would be expected for a normal earthquake in a region like Namibia. Previous studies (White et al., 2009; Viola et al., 2005) assumed that the scarp at Hebron was formed as a result of several earthquakes. We test this assumption through several geomorphological analyses including the relationship between the lithology and scarp height, knickpoints, slip distribution and the slip-to-length ratio. There is however, no definitive way to prove a single event origin, there are several geomorphological features that can be used as evidence for a multiple event hypothesis. Despite this, after performing several of these types of analyses, the results collected have consistently pointed towards a single rather than a multiple event origin for the Hebron fault.

4.3.1 Scarp height and calcretization

The height of the fault scarp appears to be controlled by the characteristics and degree of consolidation of the sediments that the fault is passing through. Specifically, the amount of calcrete-silcrete cement present controls the scarp height when the fault is passing through the Karpfenkliff breccia-conglomerates that make up the majority of the field area. Where there is more calcrete-silcrete cement, the scarp morphology is sharper and steeper than when compared with surrounding areas with lower amounts of calcretization. A good case study of this phenomenon is at the contact between the calcretized unit F and the non-calcretized unit M, where the scarp height and morphology changes dramatically (Fig. 3.10).

The fault scarp is broadly defined in two lithologies, the Karpfenkliff breccia-conglomerates and outcrops of Sinclair Sequence basement. However, the Karpfenkliff unit has been reworked in several places along the scarp, with the deposition of alluvial fans. Some of these fans show lower scarp heights, but in these cases the fans have been deposited on the hanging wall and have thus reduced the measured scarp height (Fig. 2.14).

Case study of alluvial fan generations

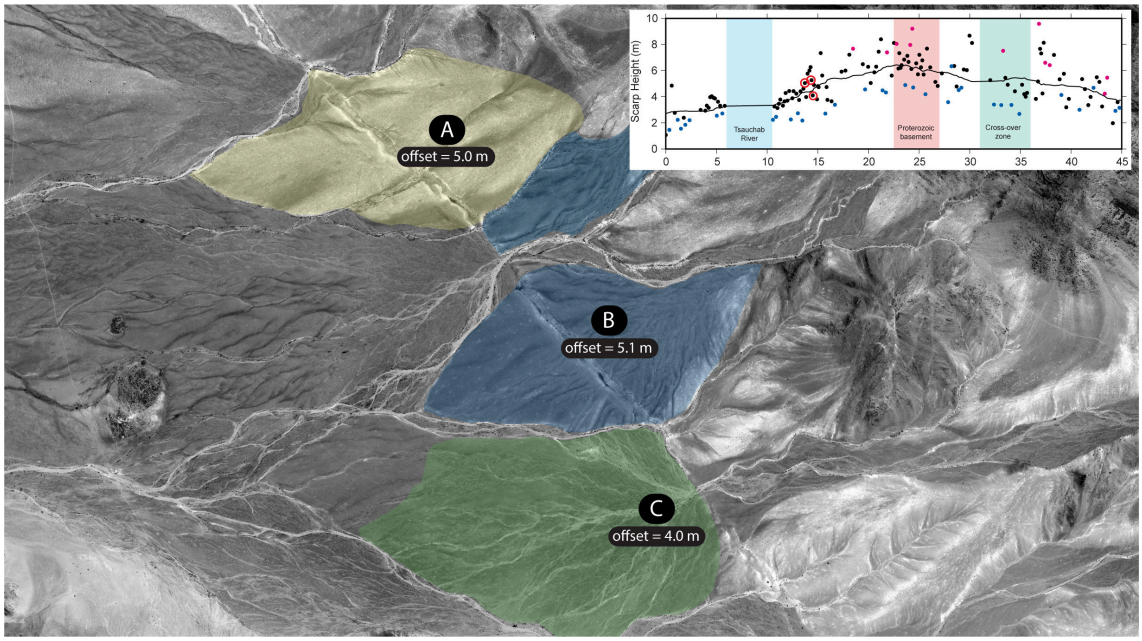

Figure 4.1: Three generations of alluvial fans

The presence of three generations of alluvial fans in the central section of the fault (Fig. 4.1) allows a comparison of scarp height and sediment age to be made. Two of these alluvial fans pre-date the scarp (A and B) and are thus displaced by the fault. The most recent generation (C) was deposited after the scarp formed with the alluvial fan being deposited on the down-thrown surface. If there have been several earthquakes, and some of these events occurred before the deposition of the younger fan generations, then the oldest fan generation would have accumulated more slip than the younger generations and thus would exhibit a higher scarp height.

The scarp height for the most recent fan was lower than that of the older fans. However, this was expected because the fan was deposited on the down-thrown surface. As such, the measured offset was less than the true offset (Fig. 2.14). The scarp height along the intermediate fan (5.1 m) was not significantly different, on average, than the scarp on the oldest alluvial fan (5.0 m) with the difference of 0.1 m being within the rangle of error. Thus, there have been no events between the formation of these fans as fan A not accumulated any more slip than fan B.

4.3.2 Knickpoints

Knickpoints are often used as geomorphological indicators of earthquakes. A single tectonic movement can create a knickpoint which then retreats towards the source (Section 2.2.3). Multiple earthquakes, separated by enough time for a knickpoint to retreat sufficiently, can stack knickpoints at various points along the length of the river's longitudinal profile (Fig. 2.11). This is dependant on the rate at which knickpoints retreat back along the profile, which in turn, is dependant on the amount of erosion. South west Namibia is very arid with very low erosion rates of 3.6 $\pm$ 1.9 m Myr^{-1} (Bierman and Caffee, 2001), thus it is unlikely that any knickpoints generated in the late Pleistocene to recent era would have retreated completely and allowed the river's profile to reach equilibrium once more. There is a good possibility that multiple earthquakes would be recorded in the longitudinal profiles of rivers crossing the fault scarps. Of the 23 profiles examined, only two examples (R and Q, Fig. 3.15) had more than one knickpoint. This may have formed due to a number of reasons discussed below. The other exceptions to this were the streams in the step-over zone which passed through two scarps. These all had at least a single knickpoint and at most two, corresponding to the number of scarps the stream has passed through. All of the profiles examined can be seen in Appendix B.

Case study: knickpoints in R and Q

Rivers R and Q are located next to one another within the Neuhof Reserve in the southern section of the fault scarp (Fig. 3.6). They are close to the lithological boundary between the calcrete-cemented breccia-conglomerates (Unit F) and a non-calcretized sedimentary unit (Unit M, Fig. 3.10). Due to their relative proximity, the factors that produced the knickpoints on these neighboring profiles are most likely the same.

Since the number of knickpoints found along the longitudinal profile of a river can be used to infer the minimum number of dip-slip earthquakes that have occurred in that area (Burbank and Anderson, 2012). One explanation for the presence of two knickpoints in these profiles is that the section of the fault scarp along these rivers has ruptured at least twice. The southern section of the fault may have ruptured first

with the northern scarp segments rupturing in subsequent events. The plausibility of this is further discussed in Section 4.3.3.

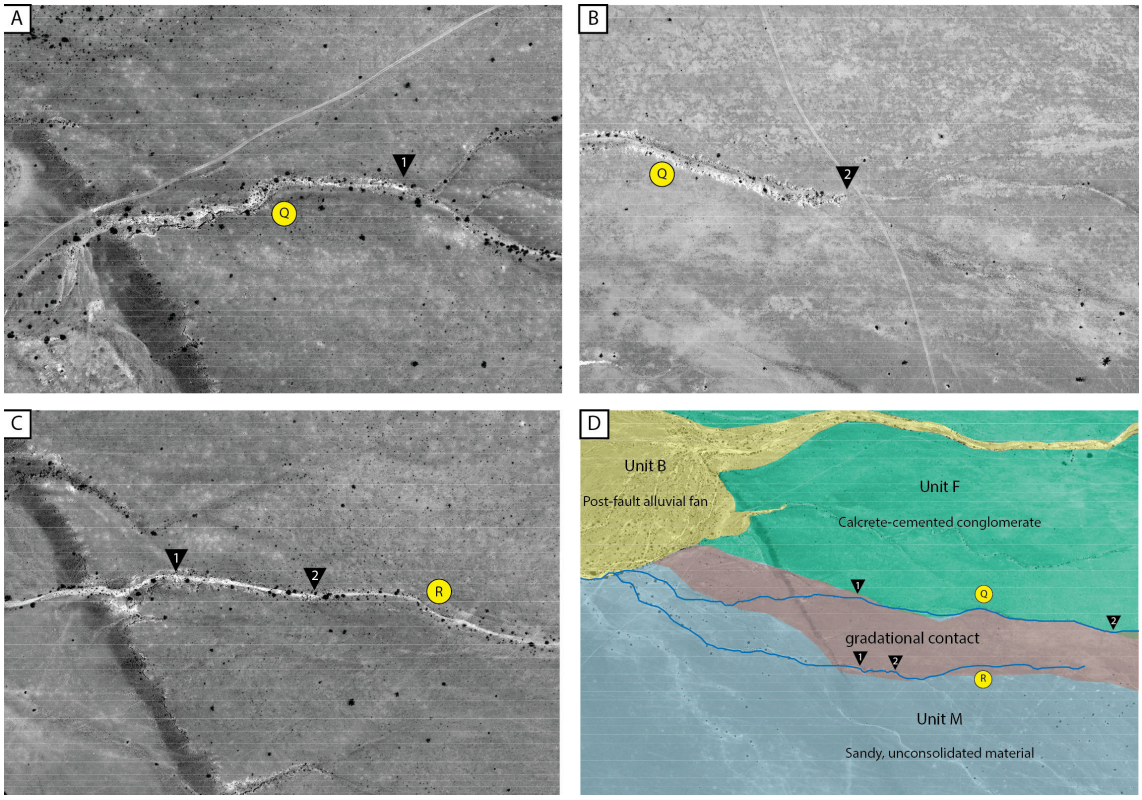

Figure 4.2: Close up look at the knickpoints on Q and R.
(A) Location of the first knickpoint, closest to the fault scarp, on stream Q.
(B) Second knickpoint location on stream Q
(C) Location of knickpoints on stream R
(D) Overview of both steams, the location of the knickpoints and the gradational contact between units M and F.

A tectonic movement is not the only mechanism that can create a knickpoint. Another process known to cause knickpoints is a difference in the resistance of lithological units. Specifically, a more erosion resistent unit being located above a less resistent unit. As the lower unit erodes faster, the harder capping unit is undercut and a knickpoint is formed (Burbank and Anderson, 2012). Unit F is a calcrete-cemented breccia-conglomerate which has already been shown to be more resistent than unit M (Fig. 3.10), as unit F preserves the scarp height much better than unit M. As such, the calcrete cement acts as the harder cap layer with less erosion resistant material below it. This works particularly well in the case of river Q, which runs along the contact between the two units (Fig. 4.2 D). Field observations

of the contact confirmed that it is gradational, with the amount of calcrete present decreasing over several hundred meters. The decrease in scarp height (Fig. 3.10) over this distance is likely a result of this lithological change. Thus, while R is south of the contact, there is still a layer of calcrete on the upper surface near R, which is responsible for one of the knickpoints.

It is possible that despite multiple events occurring in the formation of the fault scarp, there is only one knickpoint. This could happen if the rate of knickpoint retreat was very slow. And thus the knickpoint observed may actually be the result of several knickpoints that have only retreated a short distance from the fault scarp, this is an unlikely case for Hebron, despite that some knickpoints have only retreated a short distance.

4.3.3 Slip distribution

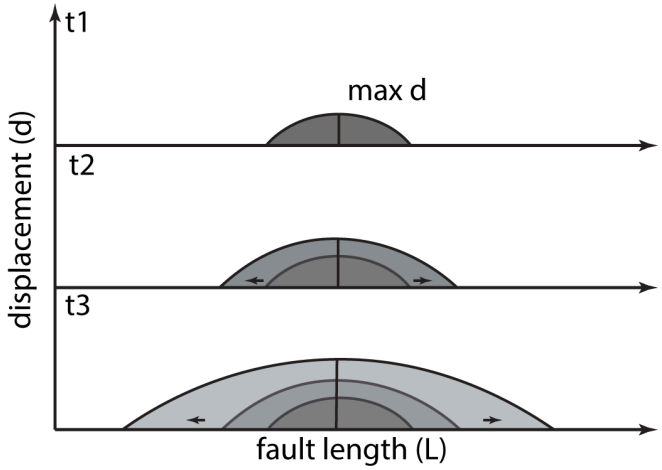

Figure 4.3: Model of fault growth for an unrestricted fault over multiple events, adapted from (Burbank and Anderson, 2012). Note that the shape of the displacement is bow-shaped

The study of fault displacement patterns is also used to estimate the number of earthquakes that have occurred on a given fault or fault segment. In order to do this, the shape of the rupture is used, measured as slip along the length of the fault. A fault with unrestricted horizontal growth will result in a bow-shaped profile (Burbank and Anderson, 2012) with each event increasing the length and height of the profile (Fig. 4.3). If the fault encounters an obstacle and thus only grows

in one direction, the profile is an asymmetric triangle (Burbank and Anderson, 2012). As a fault may form more than one segment, an older segment will have already accumulated slip relative to younger segments, having experienced more earthquakes. Thus, in fault scarps that formed as the result of several events, several rupture arcs may be identified, often being recorded on surfaces with different ages, allowing the amount of slip for separate events to be determined.

Cumulative probability density functions are often calculated for displacements along the fault. A normal distribution and standard deviation is assumed for individual offset values, based on uncertainty in measurement (McGill and Sieh, 1991). These distributions are then overlaid to produce plots like the top left panel on Fig. 4.4. The peaks in these plots are interpreted to correlate to previous rupture events, with the number of peaks indicating the number of past earthquakes (Bi et al., 2018; Zielke et al., 2010). However, it is possible for a cumulative offset measurement to be mis-interpreted as a single event offset (Zielke et al., 2010). This method is used in circumstances where the scarp height values show a lot of variation, particularly with different surfaces as is the case in Bi et al. (2018)(Fig. 4.4 A). In this study (Fig. 4.4 B), we did not observe a distinguishable difference in offset according to surface age (Section 4.3.1). As such, it was not advantageous to calculate cumulative density functions.

In Fig. 4.4 B, the slip values are lower on either edge of the fault trace and increase towards the center. The shape of the slip values from the Hebron fault can be constrained by a single, symmetrical arc. While there is some variability in these measurements, this is most likely due to different degrees of scarp preservation (due to degree of calcretization, fans deposited on the hanging wall etc.) rather than the effect of several rupturing events. The slip distribution is very similar to the shape described by the propagating fault model (Rotevatn et al., 2018). If the fault was the result of several rupturing events, then it is expected that the length would have increased. The presence of three, right-stepping, discrete fault segments may be evidence of this lengthening (Fig. 1.3). Subsequent events creating new segments should increase the amount of slip on the existing segments. However, there should

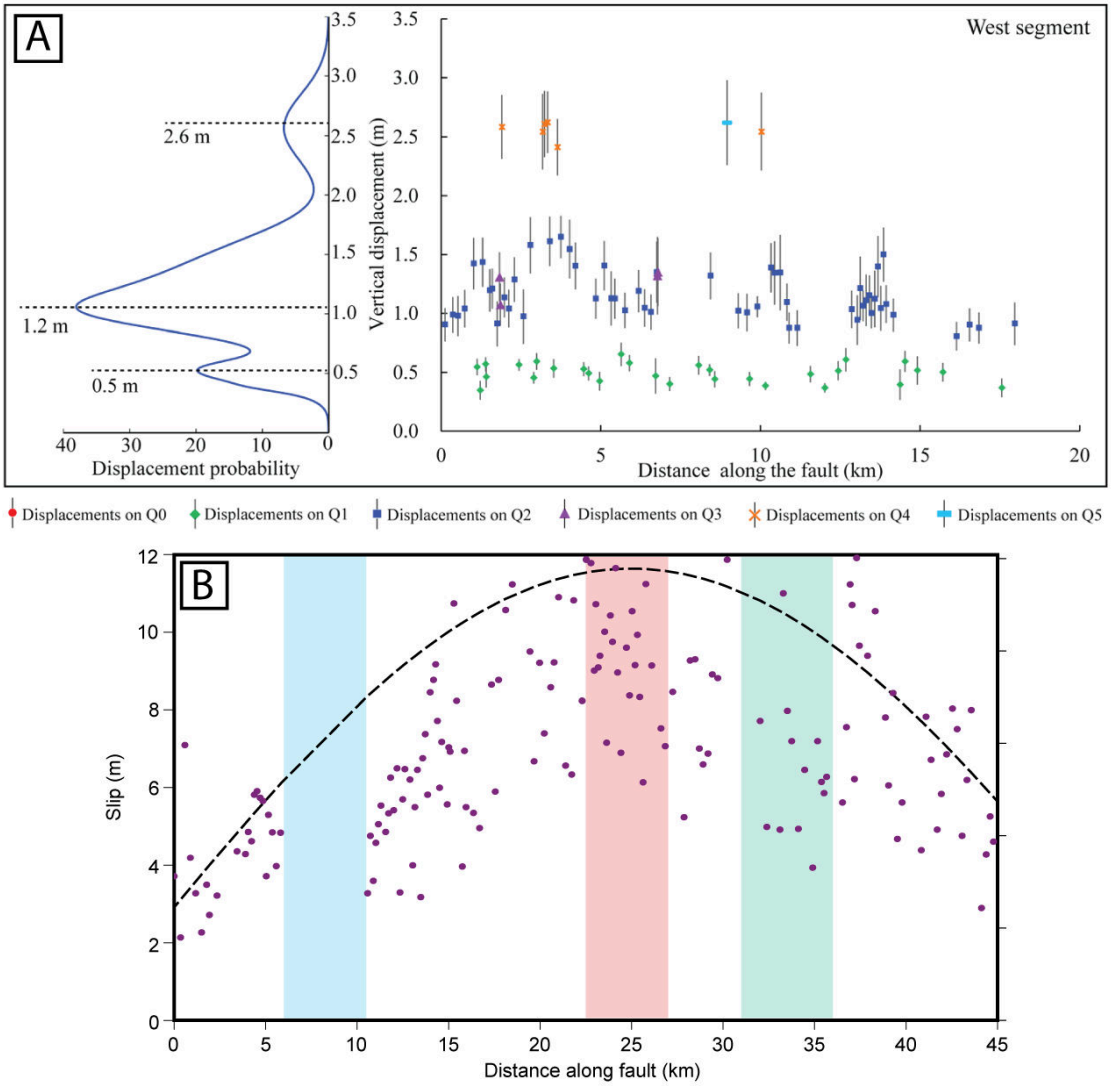

Figure 4.4: (A) Plot of slip against distance along fault from Bi et al. (2018). On the left hand side is the cumulative density function, used to distinguish multiple events in the plot.
(B) Plot of slip (calculated for a dip of 60°) against distance for Hebron (this study). Note that the shape of the slip values for this study are much more consistent with a single rupture arc

be a segment with more slip than the other two segments. This is not the case for the Hebron fault where the segments, with the exception of the off-strike NW segment, show similar amounts of slip, with peak values close to the step-over zone between two of these segments. The lower scarp heights in this segment may be due to strike-slip motion in addition to dip slip (Section 4.2). Furthermore, the step-over zone in the center of the fault displays overlapping segments with a cumulative displacement that is equal to the main segments to either side, indicating that these segments formed simultaneously, rather than in subsequent events (Zhang et al.,

1991).

The cause of single fault segmentation is thought to be related to seismogenic thickness. Fault segments are 20 - 30 km long in areas such as the Basin and Range Province where seismogenic thicknesses are *c.* 15km (Walker et al., 2017). While in areas with greater seismogenic thicknesses (>30 km), such as the East African Rift, fault segments can reach lengths of 100 km (Jackson and Blenkinsop, 1997). The longest segment on the Hebron fault is 22 km. An estimate of the depth of seismicity in this area is ≈ 17 km (Section 4.4), in which case, the length of the fault segments could be controlled by the seismogenic thickness rather than being the results of several events.

4.3.4 Slip-to-length ratio

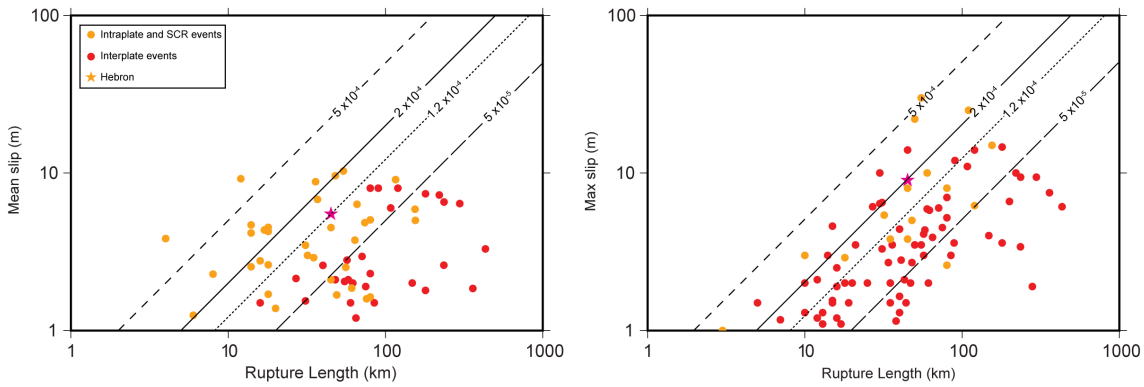

Figure 4.5: Slip-to-length ratios of intra-plate and SCR earthquakes (yellow) compared to inter-plate events (red). This studies results for Hebron are plotted as a pink star. The lines represent slip-to-length ratios from the literature as well as this study. See Appendix E for a table of events.

The relationships between different earthquake source parameters are used to predict a dependant parameter from an independent source parameter (Wells and Coppersmith, 1994). Fault scaling relationships are now used for a plethora of forecasts, including the maximum size earthquake that a given fault could produce (Equation 1.1) as well as the amount of slip that can be expected in a single event. A number of compilations, such as Wells and Coppersmith (1994), have been produced in order to determine the relationship between parameters like magnitude, rupture lengths and displacements. The ratio of the length of a surface rupture to the amount of

displacement, the slip-to-length ratio, has been found to generally be around 2.5 x 10^{-5} (Cowie and Scholz, 1992). Although, studies which have compared the slip-to-length ratio of interplate earthquakes to intraplate earthquakes, such as Scholz et al. (1986), have found that intraplate events can have higher ratios with higher stress drops — six that of an equivalent interplate event.

Hebrons' slip to length ratio implied by White et al. (2009) was 2.3 x 10^{-4}. The slip-to-length ratio determined by this study was 2 x 10^{-4}. These ratios for Hebron are an order of magnitude higher than the generally accepted average slip-to-length ratio for a single earthquake. As such, White et al. (2009) interpreted that the scarp at Hebron formed as a result of several events, each accumulating more slip but not increasing the length of the rupture significantly. This was used to explain the high slip-to-length ratio.

The majority of fault scaling compilations are predominantly comprised of inter-plate earthquakes. This is not surprising, considering that inter-plate events make up most of the seismicity observed on earth (Section 1.2). However, the Hebron Fault is within a stable continental region and thus the fault scaling relationships may be different to inter-plate conditions. In order to assess this, a compilation of slip-to-length ratios for SCR earthquakes was gathered from the literature (Appendix E) which was then compared to a compilation of inter-plate events from Wells and Coppersmith (1994) (Fig. 4.5).

On Fig. 4.5 the SCR events plot, on average, higher than the inter-plate events. Often with values near 2 x 10^{-4} and, in some cases, above this ratio. The slip-to-length ratio for the Hebron fault fits well within the range of values observed for other intra-plate and SCR events. This is in line with slip-to-length ratios having an upper bound of around 2 x 10^{-4} (Scholz, 2019). Additionally, the relationship between the mean and maximum slip is that $s_{max} = 2^{*}s_{mean}$. This is in agreement with Manighetti et al. (2005), who characterized slip distributions from 44 earthquakes with triangular slip distributions. It must be noted that almost half of our intraplate and SCR events come from a compilation of post-glacial faults (Stevens, 2019). The

higher slip-to-length ratios found within intraplate settings places the slip-to-length ratio for Hebron is well within the expected range for a single event. Furthermore, fault scaling relationships in intraplate and stable continental regions do behave differently to inter-plate areas, warranting further research.

4.3.5 Strain rate

One hypothesis for large earthquakes in SCRs is that stress accumulates slowly over large periods of time due to steady plate motions before being released when the coefficient of friction is overcome (Kanamori and Brodsky, 2004). Thus, the rate of accumulation of strain, or strain rate, could be used to infer whether multiple events could possibly have been generated on the Hebron Fault since it was reactivated $\approx$ 20 - 40 ka (White et al., 2009). If the strain rate over the last 40 kyr is enough to produce the amount of slip visible on the scarp, then multiple events could have occurred in the last 40 kyr. However, if the strain rate is very low and the loading (accumulation) period is greater than the last 40 kyr, then a multiple event hypothesis can be ruled out.

Unfortunately, the strain rate for Namibia is not well constrained. Saria et al. (2013) found an upper-bound on strain rate of 0.6 mm/yr (with a maximum residual of 1 mm) for southern Africa, although only one of their GPS stations (Windhoek) was located in Namibia. Despite this, if a low horizontal strain rate of 0.1 mm is assumed (with the current instrumentation and timeline for GPS measurements in Africa, measurements with this level of accuracy would not be possible.) a conservative amount of accumulation can be calculated. At this very low strain rate, over 40 kyr a total of 4 m would have been accumulated (horizontally). At this rate of accumulation, it would be possible for multiple events to have occurred. This is dependant on the age of the fault reactivation as determined by White et al. (2009). However, if the fault was considerably younger (10 - 20 kyr), then not enough strain would have been accumulated to account for multiple events to have been generated.

4.4 Current seismicity on the fault

In this section I investigate whether existing microseismic earthquake locations can be used to constrain the large scale fault dip and seismogenic thickness in order to estimate the potential size the earthquake that formed the fault scarp.

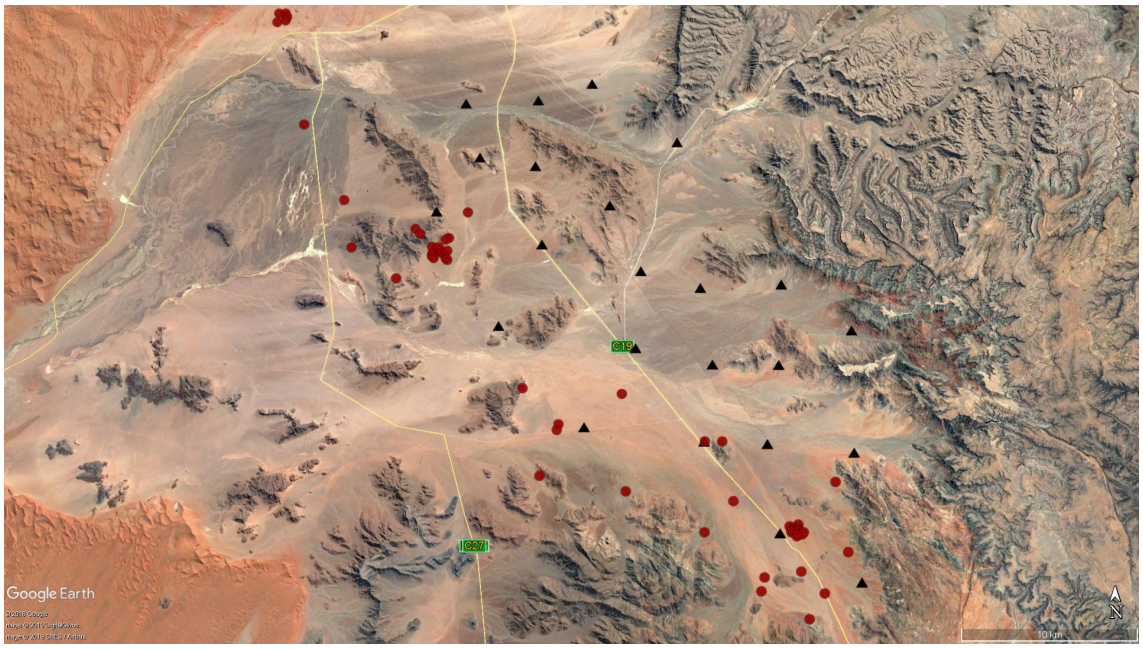

Figure 4.6: Map view of station and event distribution from Kahle (2017). Triangles represent the network stations and the red circles are earthquakes. Imagery courtesy of Google Earth

The farm owners in the area around the Hebron Fault have felt occasional tremors, indicating that there is still seismic activity along the fault. In 2017, a passive seismic network of 23 Omnirecs geophones was deployed for 3 months around the Hebron Fault. The network had an average station spacing of 2km. The data collected was processed by Kahle (2017) who identified and located a total of 78 events (Fig. 4.6 and 4.7).

These events clearly follow a plane dipping to the south west. Using the event locations and depths from Kahle (2017), I fitted a plane of best fit using linear regression, the results of which can be seen on Fig. 4.7.
In order to fit the plane to the events detected by the deployment, 20 of the 78 events were removed as they were located away from the network, far exceeding the network spacing. The remaining 58 events within the geophone network were used

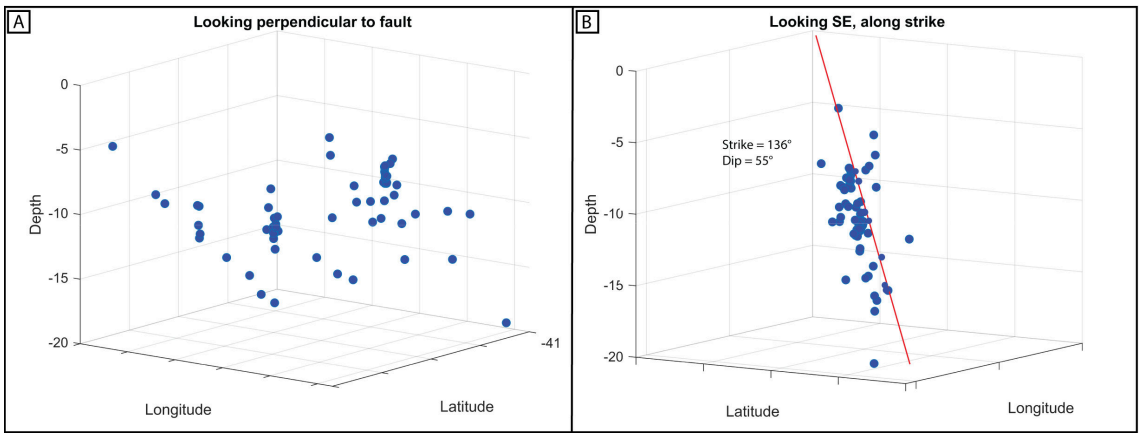

Figure 4.7: (A) Selected events looking perpendicular to the fault. (B) Selected events looking SE, along the strike of the fault.

to calculate the plane of best fit. The deepest event occurs at a depth of 17 km. Thus the minimum seismogenic thickness for Hebron is 17 km. Furthermore, the plane that was fitted to these events follows a dip of 55°. This is lower than the dip values that were observed (70°) at the surface, as well as the value calculated (74°) from the satellite imagery. The value from the plane of best fit may better approximate the dip of the fault below the surface, compared to the two surface measurements (70° - 75°). An average value of 60° was assumed for the fault as a whole. This value was then used to calculate the amount of slip and estimate the largest earthquake that the Hebron Fault could support (See Section 4.6). According to the Andersonian theory of faulting, normal faults are not expected to have dips of more than 60°, although, it is possible for steeper planes to fail as shown by the 2006 Machaze earthquake in Mozambique (Copley et al., 2012).

4.5 Regional Perspective

In order for seismicity to occur within a tectonic plate, stresses need to accumulate on the fault plane. There also need to be structures which can take up deformation and allow this stress to be released during seismic events. The stress field present in southern Namibia is dominated by the Wegener Stress Anomaly (WSA) (Fig. 4.8, Andreoli et al. (1996)). This anomaly is the incompatibility of observed extensional structures with the stress field implied from tectonic plate scale stresses. Namibia is located in the African plate, There are mid-oceanic ridge (MOR) boundaries in

the NE and SW of this plate (Fig. 4.8). From the location of these MORs, it is expected that the interior of the plate will undergo compression in a NW-SE orientation (Andreoli et al., 1996). The black bars, showing the direction of the most compressive horizontal principle stresses (Bird et al., 2006), within the WSA on Fig. 4.8 are all oriented roughly NW - SE, this is almost perpendicular to the expected orientation from the tectonic boundaries. Evidence of this takes the form of extensional structures with a NW - SE orientation, including the Hebron and Dreylington faults as well as offshore mud volcanoes (Viola et al., 2005).

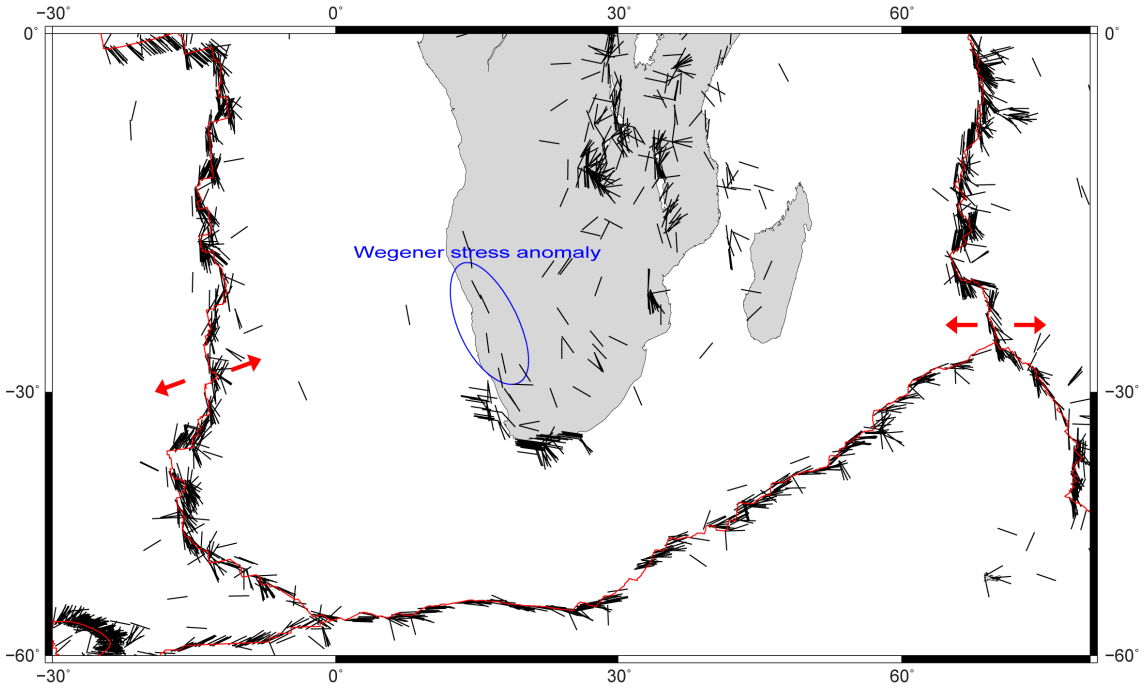

Figure 4.8: Wegener Stress Anomaly in southern Africa, strain indicators from Bird et al. (2006), the black bars show the direction of the most compressive horizontal principle stress (SH_{max}).

The presence of extension in this area, rather than compression must be controlled by factors other than the plate architecture (Viola et al., 2005). The Great Escarpment, the edge of the elevated plateau that comprises the interior of southern Africa runs NW-SE in southern Namibia, parallel to the Hebron and Dreylingen faults (Andreoli et al., 1996). The fault runs through the foothills of the escarpment. Thus, it is potentially the horizontal forces generated from the Great Escarpment that produced the extension observed within the Wegener Stress Anomaly. Similarly, White et al. (2009) interpreted Hebron to have formed as a result of coastal

gravitational collapse caused by instability associated with the African Superswell (Partridge and Maud, 1987), which is one proposed mechanism for the formation of the Great Escarpment. Furthermore, field observations of the fault plane following the bedding of the basement indicates that the fault has been re-activated on previously existing structures. These structures may have developed during the formation of Namaqua-Natal Metamorphic Province, 1 billion years ago during the Mesoproterozoic (Eglington, 2006).

4.6 Seismic Hazard Assessment

Seismic hazard assessments attempt to estimate the amount of ground movement that may occur in a particular area as a result of an earthquake (Bommer, 2002). Ground movement can be calculated for a number of parameters, such as peak ground acceleration (PGA) or spectral acceleration (SA). This is done by using ground motion prediction equations (GMPEs) and an estimate of the largest magnitude earthquakes that could be expected within the areas of interest (Bommer and Abrahamson, 2006). The location of faults in the area are important in determining the largest earthquakes that could be supported. The hazard maps produced are important for risk mitigation (Stein et al., 2012), both to existing infrastructure and future projects (Mosca et al., 2019). There are two approaches to seismic hazard assessment, namely PSHA and DSHA. The difference between these two is that DSHA only takes into account a single, or perhaps several, earthquake scenarios (Bommer and Abrahamson, 2006). PSHA takes into account the seismic record of the area and uses the a and b values of the Gutenberg Richter relationship to approximate the magnitude and frequency of future seismicity (McGuire, 1995). However, in order for the Gutenberg Richter relationship to be well constrained, there needs to be a suitable seismic record.

PSHA is the most used form of seismic hazard analysis, particularly for engineering design (Bommer, 2002). However, a PSHA can be particularly challenging when the seismological data for an area does not represent the long-term earthquake history (Mosca et al., 2019; Abdrakhmatov et al., 2016). Namibia has a poorly con-

strained history of seismicity as a result of it being a SCR as well as having very few permanent seismometers and thus poor network coverage (Mangongolo and Hutchins, 2008). Mosca et al. (2019) uses several DSHAs from palaeo-earthquakes to inform the PSHA for another SCR, the Tien Shan. This approach aims to produce a better seismic hazard analysis for regions with little seismological data. A deterministic approach was taken for this study which was then compared to the hazard map model produced by the Global Earthquake Model (GEM) using a PSHA.

Scenarios

The peak ground acceleration (PGA) was calculated for several single earthquake scenarios using the OpenQuake engine. The first scenario was for the maximum possible earthquake that could be produced by Hebron, assuming that the fault scarp had formed in one event (Fig. 4.9). The second scenario was for an earthquake magnitude that corresponds to the Hebron fault scarp being produced in two events, i.e. with only half the slip on the same fault area as the first scenario.

The results of these scenarios were then compared to the current hazard map for Namibia (Fig. 4.9A), this forms a part of the Eastern and Sub-Saharan Africa Hazard model produced by GEM (Poggi et al., 2018). This hazard model was produced in 2018 for GEM by incorporating the smoothed seismicity method employed by Poggi et al. (2017) with addition to other seismic data from southern Africa. The GEM model used to compare to our scenarios is a hazard map with a return period of 475 years, which corresponds to a 10% probability of exceedance in 50 years (Poggi et al., 2018).

The magnitudes of the earthquakes were calculated using equation $M_0 = \mu WLs$ where μ is the shear modulus (3x10^{10} Pa), W is the down-dip width of the fault (20 km, calculated from the fault dip of 60° and seismogenic thickness of 17 km), L is the fault length (45 km) and s is the slip on the fault plane (5.5 m for the first scenario and 2.75 m for the second.). Both of the scenarios used the same ground motion logic tree as was used by Poggi et al. (2018) for stable continental regions. The GMPEs used in this logic tree were OpenQuakes' AtkinsonBoore2011Modified2014

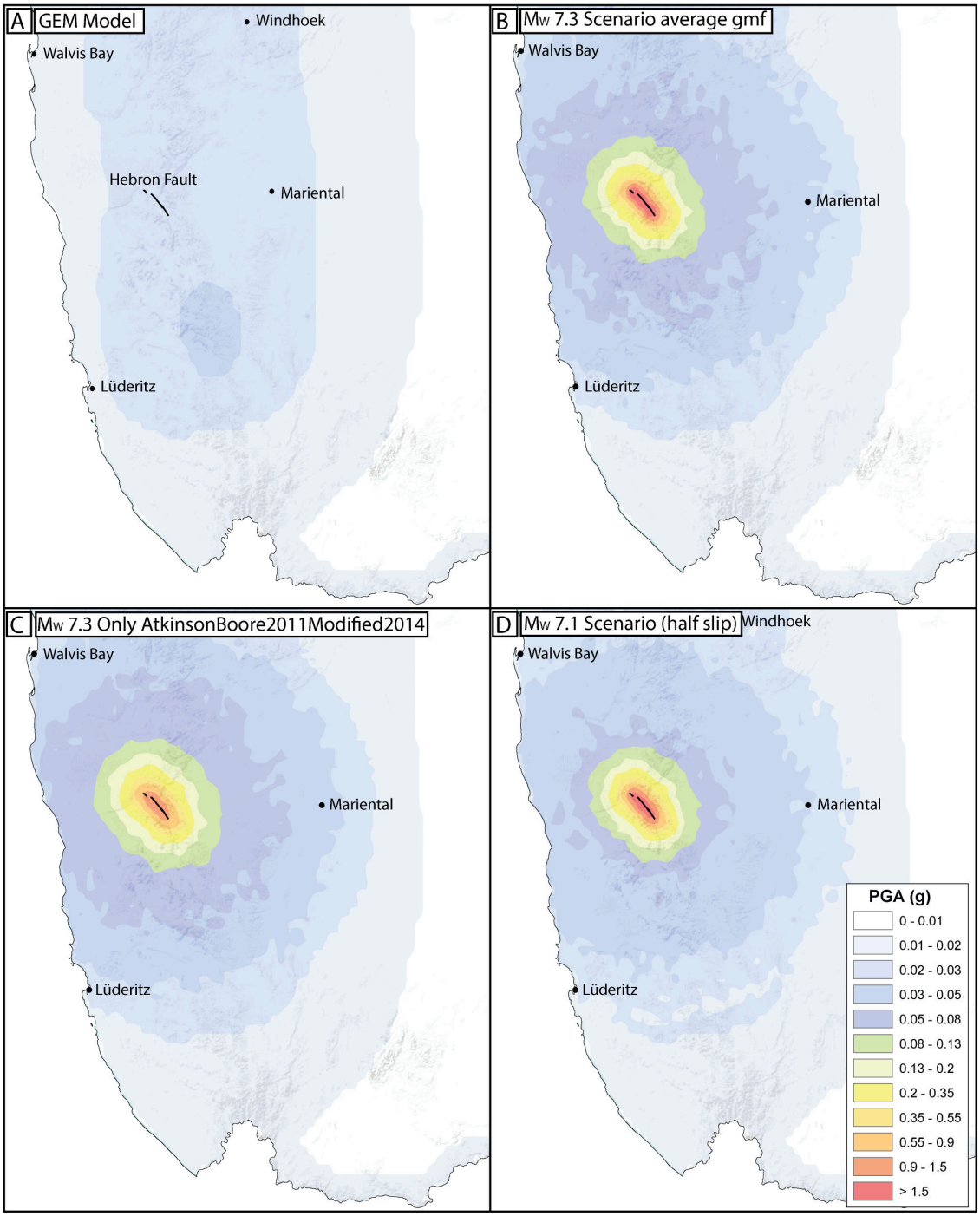

Figure 4.9: (A) GEMs hazard map for southern Namibia, ground motion is displayed as peak ground acceleration in units of g (Poggi et al., 2018).
(B) Average ground motion from 40 realizations of the first scenario, a M_W 7.3 earthquake on the Hebron fault
(C) Average ground motion from 40 realizations for the M_W 7.3 scenario if the only GMPE used was AtkinsonBoore2011Modified2014. Note that the significant difference between B and C is due to the different GMPE logic tree.
(D) Average ground motion from 40 realizations for the second scenario, a M_W 7.1 earthquake on Hebron, the result of half the amount of slip measured on the fault.

from Atkinson and Boore (2011) and PezeshkEtAl2011NEHRPBC from Pezeshk et al. (2011) with a weighting of 0.5 for each of these equations. The difference in ground motion fields between Fig. 4.9 B and C highlights the variability that different GMPEs (and weightings) can have on the ground motion fields produced. The scenarios were run for 40 realizations and the ground motion fields from these realizations were then averaged (Fig. 4.9).

The scenarios described above would produce much more ground motion than is expected for Namibia on the GEM model. This is because the GEM model includes information about the seismic history of that region and thus the probability of that area experiencing shaking exceeding the ground motion on the map within a particular time frame (in the case of GEMs model, this is 50 years.) As the seismic history of Namibia is poorly constrained, and the current seismicity is not well instrumented (Mangongolo and Hutchins, 2008), any PSHA on the area will produce low levels of seismic hazard. As slowly deforming regions do still experience large earthquakes (Abdrakhmatov et al., 2016; Calais et al., 2016), deterministic seismic hazard analyses, such as the scenarios above, can be useful to determine the maximum amount of ground shaking that the area could experience. These DSHA are particularly useful for areas where there are long recurrence intervals, due to low strain rates, and a poor record of seismicity. DSHA thus allows policy makers to be informed about the 'worst-case' scenario (Bommer and Abrahamson, 2006), in order to ensure that critical infrastructure be suitably protected. It should be noted that a DSHA therefore provides a sensible approach to assess the potential hazard, should an earthquake occur. However, DSHA relies on detailed information about the local faults, which isn't always available. Ideally, a combination of PSHA and DSHA should be used (Mosca et al., 2019) which is what most building codes require.

4.7 Future Work

The Hebron fault scarp poses the interesting problem of a potentially large (Mw 7.3) normal earthquake in a stable continental region. The repeat period in areas of slow

deformation such as SW Namibia may be on the order of tens of thousands of years. Thus, due to the relative infrequency of these events, an effort should be made in order to understand why and how they occur. How SCR events differ from their inter-plate counterparts is potentially interesting and pivotal to better understand what causes seismicity in SCRs. There are still several additional studies that can be carried out on the Hebron fault. In particular, Quaternary dating methods could be employed in order to determine when the fault ruptured and potentially find information about multiple rupture events.

Proposals for further work on the Hebron fault include:

- Palaeoseismic trenching. If generations of sediments can be distinguished, this may mean that there have been several earthquake events that formed the scarp. With each new event forming a new sedimentary package on top of the last as a result of pooling in the graben-like structure on the down-thrown block. A potential trench site has been identified and permission has been granted by the land owner.
- Quaternary dating techniques to better constrain the age of the fault
  - Cosmogenic dating. The tops of quartz rich boulders and cobbles exposed on abandoned alluvial fan surfaces were sampled for cosmogenic exposure dating (utilizing ^{10}Be and ^{26}Al isotopes). Samples were taken on both the up-thrown and down-thrown surfaces. As well as from a post-faulting alluvial fan. This should determine an age for surfaces present before the fault (up-thrown and down-thrown surfaces) as well as for a surface that was formed after the faulting (post-faulting alluvial fan). Thus the age of the scarp should fall somewhere between those dates.
  - Samples of calcrete were also taken to be used in U-series dating. We hypothesize that these calcretes were formed before the fault as they are found throughout the older surfaces present. Thus this should provide another age for surfaces before the fault was formed - because these features were formed secondary to the surface itself, they should yield younger ages than the cosmogenic samples.

Conclusions

A DEM of the Hebron Fault was produced from high-resolution, panchromatic WorldView-3 satellite imagery using stereophotogrammetry. Prior to this study, no study of fault scarps has used a DEM wholly comprised of WorldView-3 imagery. The DEM produced was of sufficient quality for detailed geomorphological analysis, with a cell resolution of 0.5 m and an absolute vertical accuracy of 0.27 m (Hu et al., 2016). Additionally, the multi-spectral imagery was used to produce a map of sedimentary packages. This DEM was used to make detailed geomorphological analysis of the fault scarp. The main segments of the fault does not show any lateral offsets, making it a pure dip-slip normal fault. This result is in agreement with that of White et al. (2009). The scarp morphology varies along the length of the fault, which appears to be due to the degree of calcretization. Highly calcretized sections along the fault exhibit a sharp scarp and sections without calcretization are diffuse. In addition, the scarp height is generally higher in calcretized sections as the rock is more resistent to erosion. This, combined with the slip distribution, which follows a clear arc (Fig. 3.19), is indicative that the scarp may have formed as a result of a single earthquake.

While strain rate can be used to infer that multiple earthquakes could have occurred on the fault, this is in part due to an assumption of both the strain rate as well as the reactivation age of the fault. There are more lines of evidence that the scarp was formed in a single event, namely the knickpoint analysis, slip distribution and the fault expression in lithologies of different ages. Thus, the Hebron scarp appears to be formed by a single large normal faulting earthquake within the SCR of Namibia. Future work could include the dating of this event, in order to improve and extend the record of seismicity in the area. This study also demonstrates that DSHA can be useful for areas of low strain rates and poor seismological records.

References

Abdrakhmatov, K. E., Walker, R. T., Campbell, G. E., Carr, A. S., Elliott, A., Hillemann, C., Hollingsworth, J., Landgraf, A., Mackenzie, D., Mukambayev, A., Rizza, M., and Sloan, R. A. (2016). Multisegment rupture in the 11 July 1889 Chilik earthquake (M w 8.0-8.3), Kazakh Tien Shan, interpreted from remote sensing, field survey, and paleoseismic trenching. *Journal of Geophysical Research: Solid Earth*, 121(6):4615–4640.

Ainscoe, E. A., Abdrakhmatov, K. E., Baikulov, S., Carr, A. S., Elliott, A. J., Grützner, C., and Walker, R. T. (2019). Variability in surface rupture between successive earthquakes on the Suusamyr Fault, Kyrgyz Tien Shan: Implications for palaeoseismology. *Geophysical Journal International*, 216(1):703–725.

Anderson, E. S., Thompson, J. A., Crouse, D. A., and Austin, R. E. (2006). Horizontal resolution and data density effects on remotely sensed LIDAR-based DEM. *Geoderma*, 132(3-4):406–415.

Andreoli, M. A. G., Doucouré, M., Van Bever Donker, J., Brandt, D., and Andersen, N. J. B. (1996). Neotectonics of southern Africa–a review. *Africa Geoscience Review*, 3(1):1–16.

Anon (2017). Introduction to Remote sensing. Distortion in aerial photos. . Humboldt State University Course - GSP216.

Atkinson, G. M. and Boore, D. M. (2011). Modifications to existing ground-motion prediction equations in light of new data. *Bulletin of the Seismological Society of America*, 101(3):1121–1135.

Baldridge, A. M., Hook, S. J., Grove, C. I., and Rivera, G. (2009). The ASTER spectral library version 2.0. *Remote Sensing of Environment*, 113(4):711–715.

Baltsavias, E. P. (1999). A comparison between photogrammetry and laser scanning. *ISPRS Journal of Photogrammetry and Remote Sensing*, 54(2-3):83–94.

Barazzetti, L., Roncoroni, F., Brumana, R., and Previtali, M. (2016). Georeferencing accuracy analysis of a single worldview-3 image collected over Milan. *International Archives of the Photogrammetry, Remote Sensing and Spatial Information Sciences - ISPRS Archives*, XLI-B1(July):429–434.

Bi, H., Zheng, W., Ge, W., Zhang, P., Zeng, J., and Yu, J. (2018). Constraining the Distribution of Vertical Slip on the South Heli Shan Fault (Northeastern Tibet) From High-Resolution Topographic Data. *Journal of Geophysical Research: Solid Earth*, 123(3):2484–2501.

Bierman, P. R. and Caffee, M. (2001). Slow rates of rock surface erosion and sediment production across the Namib Desert and Escarpment, Southern Africa. *American Journal of Science*, 301:326–358.

Bird, P., Ben-Avraham, Z., Schubert, G., Andreoli, M., and Viola, G. (2006). Patterns of stress and strain rate in southern Africa. *Journal of Geophysical Research: Solid Earth*, 111(8):1–14.

Bommer, J. J. (2002). Deterministic vs. Probabilistic seismic hazard assessment: An exaggerated and obstructive dichotomy. *Journal of Earthquake Engineering*, 6:43–73.

Bommer, J. J. and Abrahamson, N. A. (2006). Why do modern probabilistic seismic-hazard analyses often lead to increased hazard estimates? *Bulletin of the Seismological Society of America*, 96(6):1967–1977.

Brace, W. F. and Byerlee, J. D. (1966). Stick-slip as a mechanism for earthquakes. *Science*, 153(3739):990–992.

Bray, J. D., Seed, R. B., Cluff, L. S., and Seed, H. B. (1994). Earthquake fault rupture propagation through soil. *Journal of Geotechnical Engineering*, 120(3):543–561.

Burbank, D. and Anderson, R. (2012). *Tectonic geomorphology*. John Wiley & Sons.

Calais, E., Camelbeeck, T., Stein, S., Liu, M., and Craig, T. J. (2016). A new paradigm for large earthquakes in stable continental plate interiors. *Geophysical Research Letters*, 43(20):621–637.

Campbell, G. E., Walker, R. T., Abdrakhmatov, K., Jackson, J., Elliott, J. R., Mackenzie, D., Middleton, T., and Schwenninger, J.-L. (2015). Great earthquakes in low strain rate continental interiors: An example from SE Kazakhstan. *Journal of Geophysical Research: Solid Earth*, 120(8):5507–5534.

Chen, Z., Koschan, A., Chen, C.-H., and Abidi, M. (2014). *Automated Color Misalignment Correction for Close-Range and Long-Range Hyper-Resolution Multi-Line CCD Images*. Springer.

Clark, D., McPherson, A., and Van Dissen, R. (2012). Long-term behaviour of Australian stable continental region (SCR) faults. *Tectonophysics*, 566:1–30.

Cochran, W. J. and Spotila, J. A. (2017). Incipient Evolution of the Eastern California Shear Zone through a Transpressional Zone along the San Andreas Fault in the San Bernardino Mountains, California. In *AGU Fall Meeting Abstracts*.

Cohen, P. A., Bradley, A., Knoll, A. H., Grotzinger, J. P., Jensen, S., Abelson, J., Hand, K., Love, G., Metz, J., McLoughlin, N., Meister, P., Shepard, R., Tice, M., and Wilson, J. P. (2009). Tubular compression fossils from the Ediacaran Nama group, Namibia. *Journal of Paleontology*, 83(1):110–122.

Copley, A., Hollingsworth, J., and Bergman, E. (2012). Constraints on fault and lithosphere rheology from the coseismic slip and postseismic afterslip of the 2006 Mw7.0 Mozambique earthquake. *Journal of Geophysical Research: Solid Earth*, 117(3):1–16.

Copley, A., Mitra, S., Sloan, R. A., Gaonkar, S., and Reynolds, K. (2014). Active faulting in apparently stable peninsular India: Rift inversion and a Holocene-age great earthquake on the Tapti Fault. *Journal of Geophysical Research: Solid Earth*, 119(8):6650–6666.

Cowie, P. A. and Scholz, C. H. (1992). Growth of Faults by Accumulation of Seismic Slip. *Journal of Geophysical Research: Solid Earth*, 97:85–95.

Crone, A. J. and Luza, K. V. (1990). Style and timing of Holocene surface faulting on the Meers fault, southwestern Oklahoma. *Geological Society of America Bulletin*, 102(1):1–17.

Dawson, J., Cummins, P., Tregoning, P., and Leonard, M. (2008). Shallow intraplate earthquakes in Western Australia observed by interferometric synthetic aperture radar. *Journal of Geophysical Research: Solid Earth*, 113(11).

Dubayah, R. O. and Drake, J. B. (2000). Lidar Remote Sensing for Forestry. *Remote Sensing*, 96(6):44–46.

Eglington, B. M. (2006). Evolution of the Namaqua-Natal Belt, southern Africa - A geochronological and isotope geochemical review. *Journal of African Earth Sciences*, 46(1-2):93–111.

Eisenbeiss, H. (2009). UAV Photogrammetry. *ETH Zurich Research Collection*.

ESRI. How Flow Accumulation works - http://desktop.arcgis.com/en/arcmap/10.6/tools/spatial-analyst-toolbox/how-flow-accumulation-works.htm. Date accessed: 2019/05/27.

ESRI. How Flow Direction works - http://desktop.arcgis.com/en/arcmap/10.3/tools/spatial-analyst-toolbox/how-flow-direction-works.htm. Date accessed: 2019/05/27.

Falkingham, P. L. (2011). Acquisition of high resolution three-dimensional models using free, open-source, photogrammetric software. *Palaeontologia electronica*, 15(1):1–15.

Fraser, C. S. and Hanley, H. B. (2005). Bias-compensated RPCs for Sensor Orientation of High-resolution Satellite Imagery. *Photogrammetric Engineering & Remote Sensing*, 71(8):909–915.

Ghosh, S. K. (1981). *History of Photogrammetry*. Laval University, Canada.

Goetz, A. F. H., Rowan, L. C., Goetz, A. F. H., and Rowan, L. C. (1981). Geologic Remote Sensing. *Science*, 211(4484):781–791.

Gorokhovich, Y. and Voustianiouk, A. (2006). Accuracy assessment of the processed SRTM-based elevation data by CGIAR using field data from USA and Thailand

and its relation to the terrain characteristics. *Remote Sensing of Environment*, 104(4):409–415.

Grimm, A. (2007). The Origin of the Term Photogrammetry. *Photogrammetric Week '07*, pages 53–60.

Grützner, C., Walker, R. T., Abdrakhmatov, K. E., Mukambaev, A., Elliott, A. J., and Elliott, J. R. (2017). Active Tectonics Around Almaty and along the Zailisky Alatau Rangefront. *Tectonics*, 36(10):2192–2226.

Hartley, R. and Zisserman, A. (2003). *Multiple view geometry in computer vision*. Cambridge university press.

Hashim, M. and Deilami, K. (2011). Very high resolution optical satellites for DEM generation: A review. *European Journal of Scientific Research*, 49:542–554.

Haugerud, R. A., Harding, D. J., Johnson, S. Y., Harless, J. L., Weaver, C. S., and Sherrod, B. L. (2003). High-Resolution Lidar Topography of the Puget Lowland, Washington —A Bonanza for Earth Science. *GSA Today*, 13(6):4.

Henrik. Focal-length - https://commons.wikimedia.org/wiki/File:Focal-length.svg. Date accessed: 2019/05/27.

Hoal, B. and Heaman, L. (1995). The Sinclair Sequence: U-Pb age constraints from the Awasib Mountain area. *Communications of the Geological Survey of Namibia*, 10:83–91.

Hodge, M. (2018). *Development, deformation style, and seismic hazard of large normal faults*. Phd thesis, Cardiff University.

Höhle, J. (2013). DEM Generation Using a Digital Large Format Frame Camera. *Photogrammetric Engineering & Remote Sensing*, 75(1):87–93.

Hu, F., Gao, X. M., Li, G. Y., and Li, M. (2016). DEM Extraction from Worldview-3 stereo-images and accuracy evaluation. *International Archives of the Photogrammetry, Remote Sensing & Spatial Information Sciences*, 41:327–332.

International Seismological Centre (2016). *On-line Bulletin*. Internatl. Seismol. Cent., Thatcham, United Kingdom.

Jackson, J. and Blenkinsop, T. (1997). The Bilila-Mtakataka fault in Malawi: An active, 100-km, normal fault segment in thick seismogenic crust. 16(1):137–150.

Johnson, K., Nissen, E., Saripalli, S., Arrowsmith, J. R., McGarey, P., Scharer, K., Williams, P., and Blisniuk, K. (2014). Rapid mapping of ultrafine fault zone topography with structure from motion. *Geosphere*, 10(5):969–986.

Johnston, A. C. and Kanter, L. R. (1990). Earthquakes in Stable Continental Crust. *Scientific American*, 262(3):68–75.

Kahle, R. (2017). personal communication.

Kanamori, H. and Brodsky, E. E. (2004). The physics of earthquakes. *Reports on Progress in Physics*, 67(8):1429–1496.

Laussedat, A. (1898). *Recherches sur les instruments, les méthodes et le dessin topographiques: Aperçu historique sur les instruments et les méthodes*, volume 1. Gauthier-Villars.

Lindblom, E., Lund, B., Tryggvason, A., Uski, M., Bödvarsson, R., Juhlin, C., and Roberts, R. (2015). Microearthquakes illuminate the deep structure of the endglacial pärvie fault, northern sweden. *Geophysical Journal International*, 201(3):1704–1716.

Mackenzie, D. and Elliott, A. (2017). Untangling tectonic slip from the potentially misleading effects of landform geometry. *Geosphere*, 13(4):1310–1328.

Maglione, P. (2016). Very high resolution optical satellites: An overview of the most commonly used. *American Journal of Applied Sciences*, 13(1):91–99.

Mallison, H. and Wings, O. (2014). Photogrammetry in Paleontology. *Journal of Paleontological Techniques*, (12):1–3.

Mangongolo, A. and Hutchins, D. (2008). Seismicity of Namibia from 1910 to 2006. *Geology of Namibia Geological Survey of Namibia, Windhoek*, 3:27–1.

Manighetti, I., Campillo, M., Sammis, C., Mai, P., and King, G. (2005). Evidence for self-similar, triangular slip distributions on earthquakes: Implications

for earthquake and fault mechanics. *Journal of Geophysical Research: Solid Earth*, 110(B5).

Manzunzu, B., Midzi, V., Mulabisana, T. F., Zulu, B., Pule, T., Myendeki, S., and Rathod, G. W. (2019). Seismotectonics of South Africa. *Journal of African Earth Sciences*, 149:271–279.

Matsu'ura, R. S. (2017). A short history of Japanese historical seismology: past and the present. *Geoscience Letters*, 4(1):1–15.

Maurer, R. and Oblitas, K. (2001). Gujarat earthquake recovery program assessment report. *Joint Report by the World Bank and the Asian Development Bank To the Governments of Gujarat and India*.

McGill, S. F. and Sieh, K. (1991). Surficial offsets on the central and eastern Garlock Fault associated with prehistoric earthquakes. *Journal of Geophysical Research*, 96(B13):21597–21621.

McGuire, R. K. (1995). Probabilistic seismic hazard analysis and design earthquakes: closing the loop. *Bulletin of the Seismological Society of America*, 85(5):1275–1284.

Methley, B. D. F. (1986). *Computational models in surveying and photogrammetry*. Blackie.

Middleton, T. A., Walker, R. T., Parsons, B., Lei, Q., Zhou, Y., and Ren, Z. (2015). A major , intraplate , normal-faulting earthquake : The 1739 Yinchuan event in northern China. *Journal of Geophysical Research : Solid Earth*, 4:293–320.

Mitchell, P. (2002). *The Archaeology of Southern Africa*. Cambridge University Press.

Molnar, P. (1979). Earthquake recurrence intervals and plate tectonics. *Bulletin of the Seismological Society of America*, 69(1):115–133.

Mosca, I., Baptie, B., Sargeant, S., and Walker, R. T. (2019). Integrating outcomes from probabilistic and deterministic seismic hazard analysis in the Tien Shan. *Bulletin of the Seismological Society of America*, 109(2):688–715.

Over, M., Schilling, A., Neubauer, S., and Zipf, A. (2010). Generating web-based 3D City Models from OpenStreetMap: The current situation in Germany. *Computers, Environment and Urban Systems*, 34(6):496–507.

Partridge, T. C. and Maud, R. R. (1987). Geomorphic evolution of southern Africa since the Mesozoic. *South African Journal of Geology*, 90(2):179–208.

Pezeshk, S., Zandieh, A., and Tavakoli, B. (2011). Hybrid empirical ground-motion prediction equations for Eastern North America using NGA models and updated seismological parameters. *Bulletin of the Seismological Society of America*, 101(4):1859–1870.

Poggi, V., Durrheim, R., Tuluka, G., Weatherill, G., Gee, R., Pagani, M., Nyblade, A., and Delvaux, D. (2018). Hazard Model for Sub-Saharan Africa. Technical report, Global Earthquake Model (GEM).

Poggi, V., Durrheim, R., Tuluka, G. M., Weatherill, G., Gee, R., Pagani, M., Nyblade, A., and Delvaux, D. (2017). Assessing seismic hazard of the East African Rift: a pilot study from GEM and AfricaArray. *Bulletin of Earthquake Engineering*, 15(11):4499–4529.

Raucoules, D., Ristori, B., De Michele, M., and Briole, P. (2010). Surface displacement of the mw 7 machaze earthquake (mozambique): Complementary use of multiband insar and radar amplitude image correlation with elastic modelling. *Remote Sensing of Environment*, 114(10):2211–2218.

Rotevatn, A., Jackson, C. A., Tvedt, A. B., Bell, R. E., and Blækkan, I. (2018). How do normal faults grow? *Journal of Structural Geology*, 125:174–184.

Saria, E., Calais, E., Altamimi, Z., Willis, P., and Farah, H. (2013). A new velocity field for Africa from combined GPS and DORIS space geodetic Solutions: Contribution to the definition of the African reference frame (AFREF). *Journal of Geophysical Research: Solid Earth*, 118(4):1677–1697.

Scholz, C. H. (2019). *The mechanics of earthquakes and faulting*. Cambridge university press.

Scholz, C. H., Aviles, C., and Wesnousky, S. G. (1986). Scaling differences between large interplate and intraplate earthquakes. *Bulletin of the Seismological Society of America*, 76(1):65–70.

Seeber, L., Ekström, G., Jain, S. K., Murty, C., Chandak, N., and Armbruster, J. G. (1996). The 1993 killari earthquake in central india: A new fault in mesozoic basalt flows? *Journal of Geophysical Research: Solid Earth*, 101(B4):8543–8560.

Siart, C., Bubenzer, O., and Eitel, B. (2009). Combining digital elevation data (SRTM/ASTER), high resolution satellite imagery (Quickbird) and GIS for geomorphological mapping: A multi-component case study on Mediterranean karst in Central Crete. *Geomorphology*, 112(1-2):106–121.

Singh, R. P., Bhoi, S., and Sahoo, A. K. (2002). Changes observed in land and ocean after Gujarat earthquake of 26 January 2001 using IRS data. *International Journal of Remote Sensing*, 23(16):3123–3128.

Stein, S., Geller, R. J., and Liu, M. (2012). Why earthquake hazard maps often fail and what to do about it. *Tectonophysics*, 562-563:1–25.

Stevens, V. (2019). personal communication.

Stewart, I. S., Sauber, J., and Rose, J. (2000). Glacio-seismotectonics: ice sheets, crustal deformation and seismicity. *Quaternary Science Reviews*, 19(14-15):1367–1389.

Tadono, T., Ishida, H., Oda, F., Naito, S., Minakawa, K., and Iwamoto, H. (2014). Precise global dem generation by alos prism. *ISPRS Annals of the Photogrammetry, Remote Sensing and Spatial Information Sciences*, 2(4):71.

Talebian, M., Copley, A. C., Fattahi, M., Ghorashi, M., Jackson, J. A., Nazari, H., Sloan, R. A., and Walker, R. T. (2016). Active faulting within a megacity : the geometry and slip rate of the Pardisan thrust in central Tehran , Iran. *Geophysical Journal International Geodynamics and Tectonics*, 207(3):1688–1699.

Tao, C. V. and Hu, Y. (2001). A comprehensive study of the rational function model for photogrammetric processing. *Photogrammetric Engineering and Remote Sensing*, 67(12):1347–1357.

Tsanis, I. K., Seiradakis, K. D., Daliakopoulos, I. N., Grillakis, M. G., and Koutroulis, A. G. (2014). Assessment of GeoEye-1 stereo-pair-generated DEM in flood mapping of an ungauged basin. *Journal of Hydroinformatics*, 16(1):1–18.

Vadman, M. (2019). Mapping of displacements near Parkfield, California. Technical report, National Center for Airbourne Laser Mapping (NCALM), distributed by OpenTopography.

Vanneste, K., Verbeeck, K., Camelbeeck, T., Paulissen, E., Meghraoui, M., Renardy, F., Jongmans, D., and Frechen, M. (2001). Surface-rupturing history of the Bree fault scarp, Roer Valley graben: Evidence for six events since the late Pleistocene. *Journal of Seismology*, 5(3):329–359.

Viola, G., Andreoli, M., Ben-Avraham, Z., Stengel, I., and Reshef, M. (2005). Offshore mud volcanoes and onland faulting in southwestern Africa: Neotectonic implications and constraints on the regional stress field. *Earth and Planetary Science Letters*, 231(1-2):147–160.

Vogelsang, R. (1998). Middle-Stone-Age-Fundstellen in Südwest-Namibia. 11.

Waack, F. G. (1985). *Stereo photography*. Reel 3-D Enterprises, Incorporated.

Walker, R. T., Wegmann, K. W., Bayasgalan, A., Carson, R. J., Elliott, J., Fox, M., Nissen, E., Sloan, R. A., Williams, J. M., and Wright, E. (2017). The Egiin Davaa prehistoric rupture, central Mongolia: A large magnitude normal faulting earthquake on a reactivated fault with little cumulative slip located in a slowly deforming intraplate setting. *Geological Society Special Publication*, 432(1):187–212.

Wallace, R. E. (1968). Notes on Stream Channels Offset by the San Andreas Fault, Southern Coast Ranges, California. *Conference on Geologic Problems of the San Andreas Fault System*.

Wells, D. L. and Coppersmith, K. J. (1994). Empirical relationships among magnitude, rupture length, rupture width, rupture area and surface displacements. *Bulletin of the Seismological Society of America*, 84(4):974–1002.

Westoby, M. J., Brasington, J., Glasser, N. F., Hambrey, M. J., and Reynolds, J. M. (2012). 'Structure-from-Motion' photogrammetry: A low-cost, effective tool for geoscience applications. *Geomorphology*, 179:300–314.

White, S., Stollhofen, H., Stanistreet, I. G., and Lorenz, V. (2009). Pleistocene to Recent rejuvenation of the Hebron Fault, SW Namibia. *Geological Society, London, Special Publications*, 316(1):293–317.

Wolf, P. R., Dewitt, B. A., and Wilkinson, B. E. (2000). *Elements of Photogrammetry: with applications in GIS*, volume 3. McGraw-Hill New York.

Wood, H. O. and Neumann, F. (1931). Modified Mercalli Intensity Scale of 1931. *Bulletin of the Seismological Society of America*, 21(4):277–283.

Zhang, P., Slemmons, D. B., and Mao, F. (1991). Geometric pattern, rupture termination and fault segmentation of the Dixie Valley-Pleasant Valley active normal fault system, Nevada, U.S.A. *Journal of Structural Geology*, 13(2):165–176.

Zhou, Y., Elliott, J. R., Parsons, B., and Walker, R. T. (2015). The 2013 Balochistan earthquake: An extraordinary or completely ordinary event? *Geophysical Research Letters*, 42(15):6236–6243.

Zielke, O., Ramón Arrowsmith, J., Ludwig, L. G., and Akçiz, S. O. (2010). Slip in the 1857 and earlier large earthquakes along the Carrizo Plain, San Andreas Fault. *Science*, 327(5969):1119–1122.

Zink, M., Bachmann, M., Bräutigam, B., Fritz, T., Hajnsek, I., Krieger, G., Moreira, A., and Wessel, B. (2014). TanDEM-X: The new global DEM takes shape. *IEEE Geoscience and Remote Sensing Magazine*, 2(2):8–23.

Worldview-3 Specifications

DATA SHEET

DigitalGlobe™

WorldView-3

Introducing WorldView-3, the first multi-payload, super-spectral, high-resolution commercial satellite. Operating at an expected altitude of 617 km, WorldView-3 provides 31 cm panchromatic resolution, 1.24 m multispectral resolution, 3.7 m short-wave infrared resolution, and 30 m CAVIS resolution. WorldView-3 has an average revisit time of <1 day and is capable of collecting up to 680,000 km² per day, further enhancing the DigitalGlobe collection capacity for more rapid and reliable collection. Launching in 2014, the WorldView-3 system will allow DigitalGlobe to further expand its imagery product offerings.

Features

- Very high-resolution*
  - Panchromatic 31 cm
  - Visible & near-infrared 1.24 m
  - Short-wave infrared 3.7 m
  - CAVIS 30 m

  *Will be resampled for commercial distribution
- The most spectral diversity commercially available
  - Panchromatic band
  - 4 standard VNIR colors: blue, green, red, near-IR1
  - 4 added VNIR colors: coastal, yellow, red edge, and near-IR2
  - 8 SWIR bands: Penetrates haze, fog, smog, dust, and smoke
  - 12 CAVIS bands: Maps clouds, ice and snow, corrects for aerosol and water vapor
- Industry-leading geolocation accuracy
- High capacity in various collection modes
- Bi-directional scanning
- Rapid retargeting using Control Moment Gyros (>2x faster than any competitor)
- Direct Access tasking from and image transmission to customer sites
- Daily revisits

Benefits

- Simultaneous, high resolution, super-spectral imagery
- Large area mono and stereoscopic collection eliminates temporal variations
- Precision geo-location possible without ground control points
- Global capacity of 680,000 km² per day
- New and enhanced applications, including:
  - Mapping
  - Land Classifications
  - Disaster Preparedness/Response
  - Feature Extraction/Change Detection
  - Soil/Vegetative Analysis
  - Geology: Oil & Gas, Mining
  - Environmental Monitoring
  - Bathymetry/Coastal Applications
  - Identification of Man-made Materials
- Superior Haze Penetration

WorldView-3 artist rendering

DATA SHEET

DIGITALGLOBE CONSTELLATION » WORLDVIEW-3

DigitalGlobe™

Design and specifications

Orbit	Altitude: 617 km Type: SunSync, 10:30 am descending Node Period: 97 min.
Life	Spec Mission Life: 7.25 years Estimated Service Life: 10 to 12 years
Spacecraft Size, Mass and Power	Size: 5.7 m (18.7 ft) tall x 2.5 m (8 ft) across 7.1 m (23 ft) across deployed solar arrays Mass: 2800 kg (6200 lbs) Power: 3.1 kW solar array, 100 Ahr battery
Sensor Bands	Panchromatic: 450 - 800 nm 8 Multispectral: Coastal: 400 - 450 nm — Red: 630 - 690 nm Blue: 450 - 510 nm — Red Edge: 705 - 745 nm Green: 510 - 580 nm — Near-IR1: 770 - 895 nm Yellow: 585 - 625 nm — Near-IR2: 860 - 1040 nm 8 SWIR Bands: SWIR-1: 1195 - 1225 nm — SWIR-5: 2145 - 2185 nm SWIR-2: 1550 - 1590 nm — SWIR-6: 2185 - 2225 nm SWIR-3: 1640 - 1680 nm — SWIR-7: 2235 - 2285 nm SWIR-4: 1710 - 1750 nm — SWIR-8: 2295 - 2365 nm 12 CAVIS Bands: Desert Clouds: 405 - 420 nm — Water-3: 930 - 965 nm Aerosol-1: 459 - 509 nm — NDVI-SWIR: 1220 - 1252 nm Green: 525 - 585 nm — Cirrus: 1365 - 1405 nm Aerosol-2: 635 - 685 nm — Snow: 1620 - 1680 nm Water-1: 845 - 885 nm — Aerosol-1: 2105 - 2245 nm Water-2: 897 - 927 nm — Aerosol-2: 2105 - 2245 nm
Sensor Resolution (or GSD, Ground Sample Distance; off-nadir is geometric mean)	Panchromatic Nadir: 0.31 m 20° Off-Nadir: 0.34 m Multispectral Nadir: 1.24 m 20° Off-Nadir: 1.38 m SWIR Nadir: 3.70 m 20° Off-Nadir: 4.10 m CAVIS Nadir: 30.00 m
Dynamic Range	11-bits per pixel Pan and MS; 14-bits per pixel SWIR
Swath Width	At nadir: 13.1 km
Attitude Determination and Control	Type: 3-axis Stabilized Actuators: Control Moment Gyros (CMGs) Sensors: Star trackers, precision IRU, GPS
Pointing Accuracy and Knowledge	Accuracy: <500 m at image start/stop Knowledge: Supports geolocation accuracy below
Retargeting Agility	Time to Slew 200 km: 12 sec
Onboard Storage	2199 Gb solid state with EDAC
Communications	Image & Ancillary Data: 800 and 1200 Mbps X-band Housekeeping: 4, 16, 32, or 64 kbps real time, 524 kbps stored, X-band Command: 2 or 64 kbps S-band
Max Contiguous Area Collected in a Single Pass (30° off-nadir angle)	Mono: 66.5 km x 112 km (5 strips) Stereo: 26.6 km x 112 km (2 pairs)
Revisit Frequency (at 40°N Latitude)	1 m GSD: <1.0 day 4.5 days at 20° off-nadir or less
Geolocation Accuracy (CE90)	Predicted <3.5 m CE90 without ground control
Capacity	680,000 km² per day

Collection scenarios

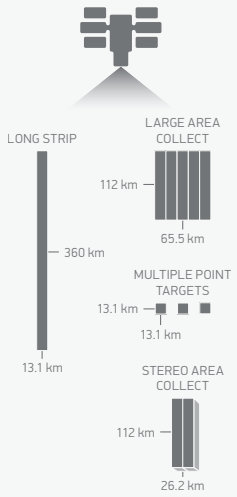

Sensor bands

- Panchromatic
- Multispectral
- 4 additional multispectral bands
- 8 SWIR bands
- 12 CAVIS bands

DS-WV3 05/14

Corporate (U.S.) +1.303.684.4561 or +1.800.496.1225 | London +44.20.8899.6801 | Singapore +65.6389.4851

Knickpoint Analysis Results

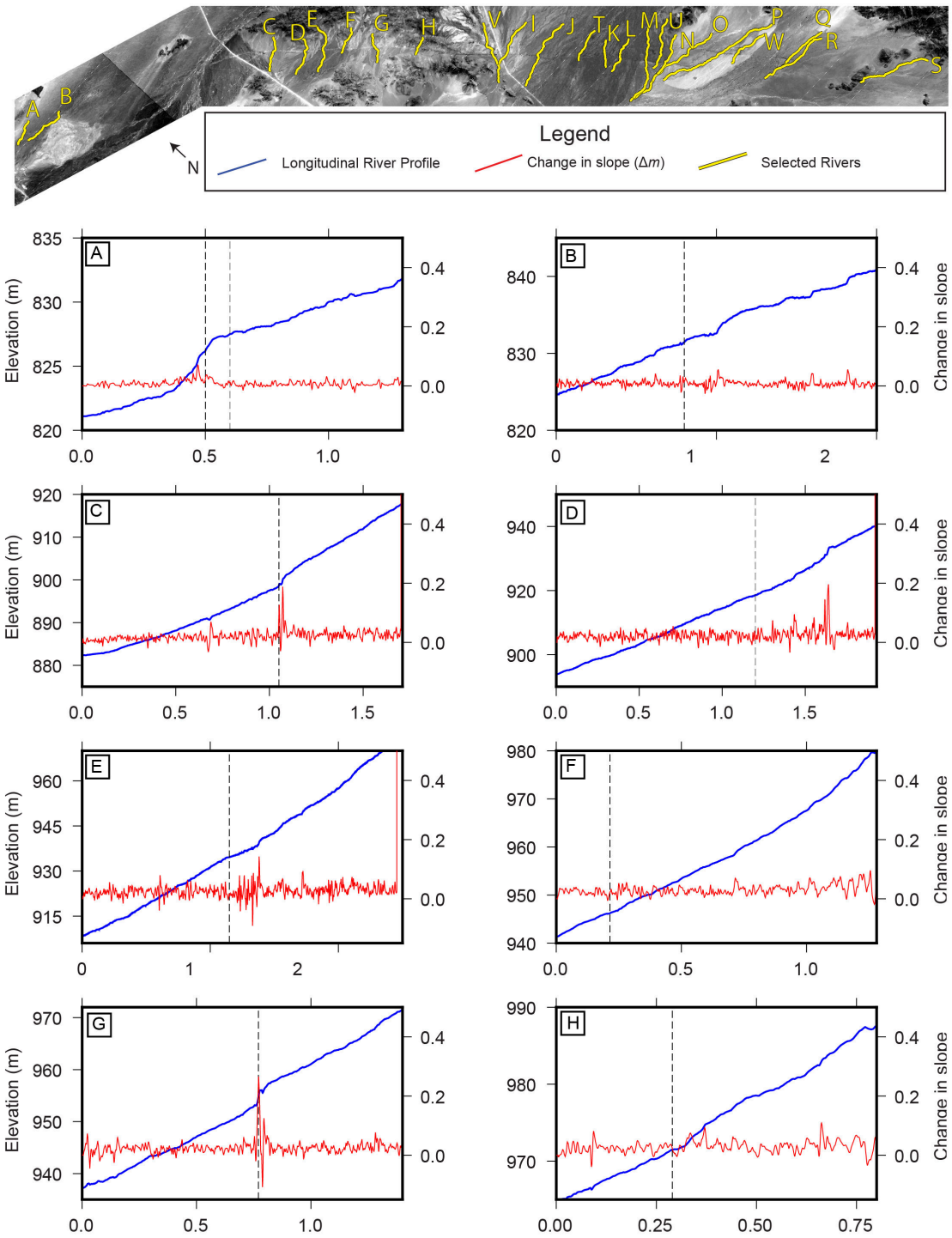

H

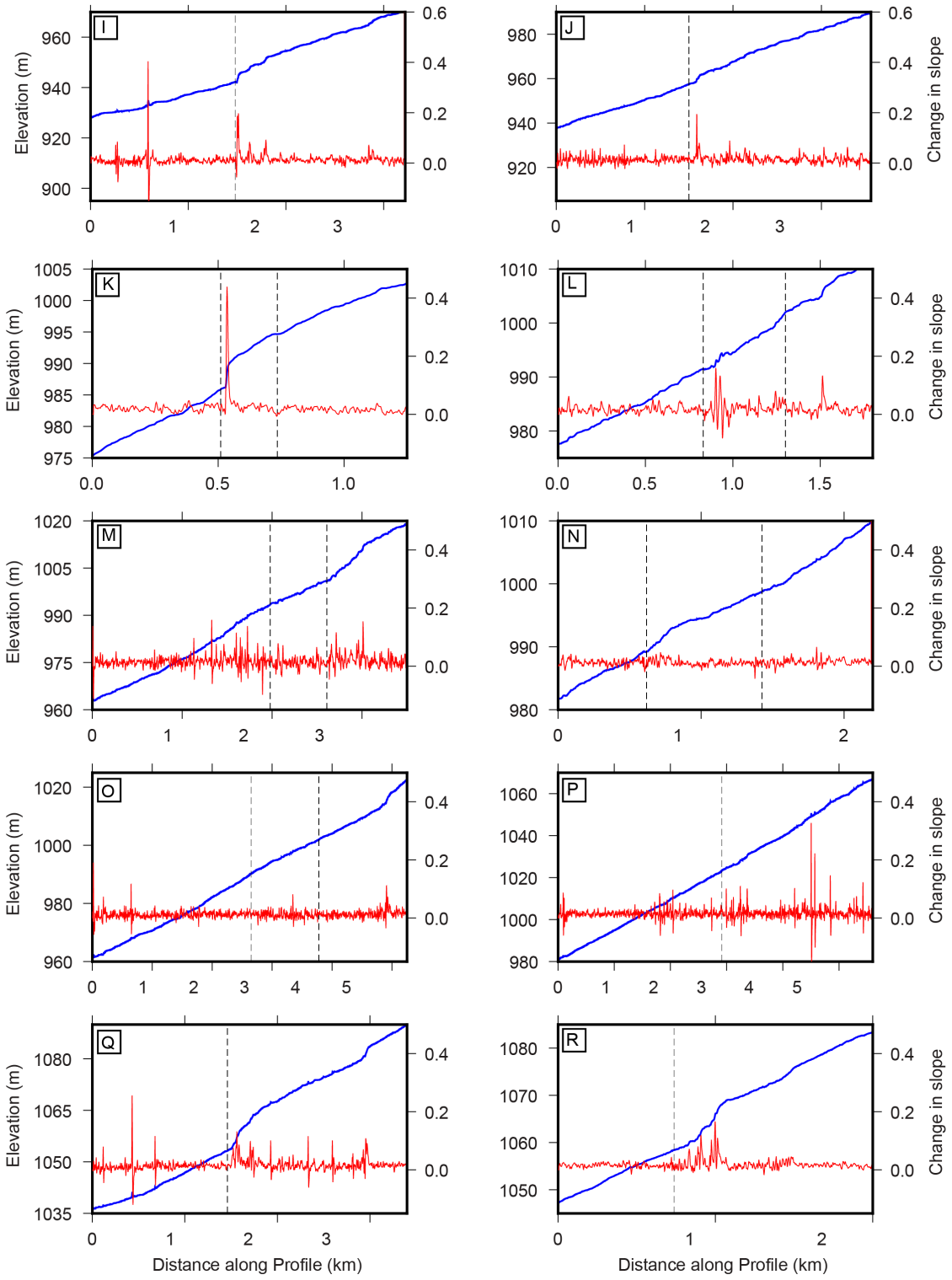
I
J
K
L
M
N
O
P
Q
R
Elevation (m)
Change in slope
Distance along Profile (km)

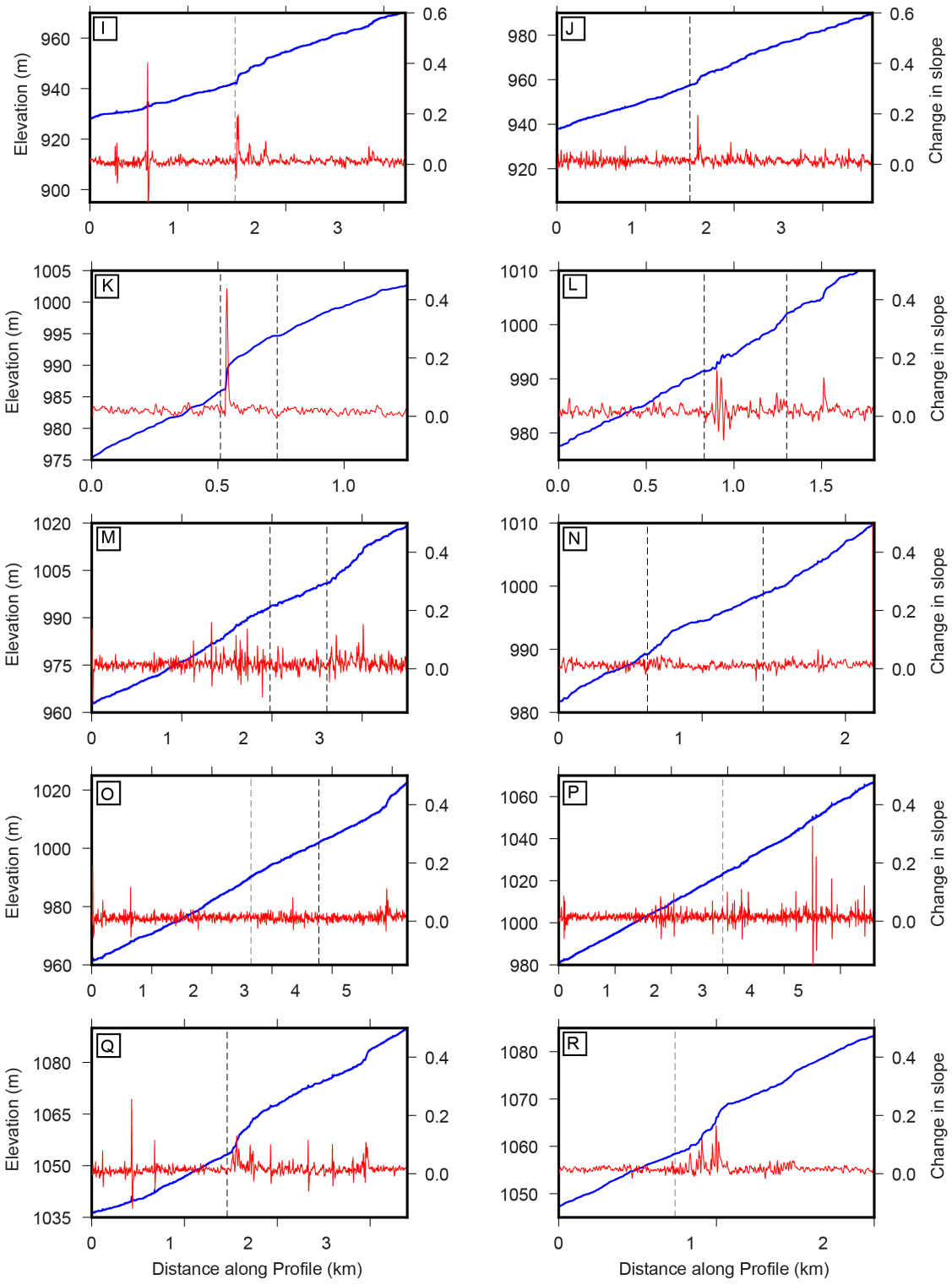
I
J
K
L
M
N
O
P
Q
R
Elevation (m)
Change in slope
Distance along Profile (km)

Matlab code: cross_section function

```
function [vert_off, moving_mean, dist_along_fault] = cross_section(filename,
    profile_spacing)
% Function CROSS_SECTION requires a file input in the form of a table of X (
    horizontal dist)
% and Z (elevation) values in columns - preferably from a .xlsx, .csv, .txt or .dat
    file.
%
%The function plots cross sections for the table into individual figures
% It also calculates a linear regression using least squares and
% plots the associated line of best fit on the same figure.

% NOTE: ensure that the coloumns in the file are in the format: X,Z - this can be
    repeated any
% number of times with additional columns. Both units should be the same (ie: m)
% NB: x data should go from the lower side of the fault (ie x min) to the higher
tic;
T = readtable(filename);                %   Creating a table from a file
A = table2array(T);                     %   Converting to an array
vert_off = [];
spacing = profile_spacing;
% Splitting the data into two, representing planes below (lower) and
% above (upper) of the fault plane
col = size(A,2);
z = 1;                                  % setting up x to change the figure number
    and generate new figures
for c = 1:2:col
    n = size(A,1);
    lower = [];
    upper = [];
    Ax = rmmissing(A(1:end,c));                     % reading coloumns from array
```

```
26      Ay = rmmissing(A(1:end,c+1));
27      MaxX = max(Ax);
28      s = size(Ax);
29      for ii = 1:s
30          if Ax(ii) <= 0.33*MaxX && Ax(ii) >= 0.1*MaxX
31              lower = [lower; A(ii,:)];
32          elseif Ax(ii) >= 0.66*MaxX && Ax(ii) <= 0.9*MaxX
33              upper = [upper; A(ii,:)];
34              %end
35          end
36      end
37
38      % Linear Regression
39      % Lower Plane
40      N = size(lower,1);                  % Determine how many numbers
41      Xl = [ ones(N,1) lower(:,c) ];      % Fit to f(x) = m*x + c
42      al = (Xl.'*Xl)\(Xl.'*lower(:,c+1));
43      cl = al(1);                         % Y intercept
44      ml = al(2);                         % Gradient
45      xl = linspace(min(Ax),0.5*MaxX,100);     % Calculate line of best fit
46      fl = ml*xl + cl;
47      % Upper Plane
48      M = size(upper,1);                  % Determine how many numbers
49      Xu = [ ones(M,1) upper(:,c) ];      % Fit to f(x) = m*x + c
50      au = (Xu.'*Xu)\(Xu.'*upper(:,c+1));
51      cu = au(1);                         % Y intercept
52      mu = au(2);                         % Gradient
53      xu = linspace(0.5*MaxX,max(Ax),100);
54      fu = mu*xu + cu;
55
56      % Find and remove outliers
57          % Upper plane
58      for aa = size(upper,1)
59          if upper(aa,2) > (mu*upper(aa,1) + cu + 1) % Change value after cu to adjust
    outlier
60              upper(aa,:) = [];
61          end
62      end
63      for aa = size(upper,1)
```

```
64      if upper(aa,2) > (mu*upper(aa,1) + cu + 0.5) % Change value after cu to
    adjust outlier
65          upper(aa,:) = [];
66      end
67  end
68  for aa = size(upper,1)
69      if upper(aa,2) > (mu*upper(aa,1) + cu + 0.1) % Change value after cu to
    adjust outlier
70          upper(aa,:) = [];
71      end
72  end
73      % Lower plane
74  for aa = size(lower,1)
75      if lower(aa,2) > (ml*lower(aa,1) + cl + 1) % Change value after cu to adjust
    outlier
76          lower(aa,:) = [];
77      end
78  end
79  for aa = size(lower,1)
80      if lower(aa,2) > (ml*lower(aa,1) + cl + 0.5) % Change value after cu to
    adjust outlier
81          lower(aa,:) = [];
82      end
83  end
84  for aa = size(lower,1)
85      if lower(aa,2) > (ml*lower(aa,1) + cl + 0.1) % Change value after cu to
    adjust outlier
86          lower(aa,:) = [];
87      end
88  end
89
90  % Recalculate the linear model without outliers
91  fu250 = mu*0.5*MaxX + cu;
92  fl250 = ml*0.5*MaxX + cl;
93      % Upper
94  M = size(upper,1);                  %Determine how many numbers
95  Xu = [ ones(M,1) upper(:,c) ];      %Fit to f(x) = m*x + c
96  au = (Xu.'*Xu)\(Xu.'*upper(:,c+1));
97  cu = au(1);                         % Y intercept
```

```
98  mu = au(2);                                % Gradient
99  xu = linspace(0.5*MaxX,max(Ax),100);
100   if mu < 0 % resets negative top surfaces to a 0.1 degree slope
101       mu = 0.0017;
102       cu = (fu250 - mu*0.5*MaxX)- 0.5*MaxX*tand(0.1); % assuming cross section is
    500m
103   end
104 fu = mu*xu + cu;
105     % Lower
106 N = size(lower,1);                          % Determine how many numbers
107 Xl = [ ones(N,1) lower(:,c) ];              % Fit to f(x) = m*x + c
108 al = (Xl.'*Xl)\(Xl.'*lower(:,c+1));
109 cl = al(1);                                % Y intercept
110 ml = al(2);                                % Gradient
111 xl = linspace(min(Ax),0.5*MaxX,100);       % Calculate line of best fit
112  if ml < 0
113      ml = 0.0017;
114      cl = (fl250 - ml*0.5*MaxX) - 0.5*MaxX*tand(0.1) ;
115  end
116
117 fl = ml*xl + cl;
118
119 % Calculate the vertical offset
120 fu250 = mu*0.5*MaxX + cu;
121 fl250 = ml*0.5*MaxX + cl;
122 vert_off = [ vert_off fu250 - fl250 ];
123 moving_mean = movmean(vert_off,5);          % Change the number after the offset
    to change the moving mean window
124 dist_along_fault = [0:(spacing/1000):(spacing/1000)*(length(vert_off)-1)];
125
126 % Plot the results
127 figure (z)
128 plot(Ax,Ay,'-b',xl,fl,'-r',xu,fu,'-r')
129 axis normal
130 xlabel('Horizontal Distance (m)');
131 ylabel('Elevation (m)');
132 legend('Surface','Lower Plane','Upper Plane');
133 z = z +1;
134
```

```
135
136 end
137 toc
138 end
```

Cross section plane fitting results

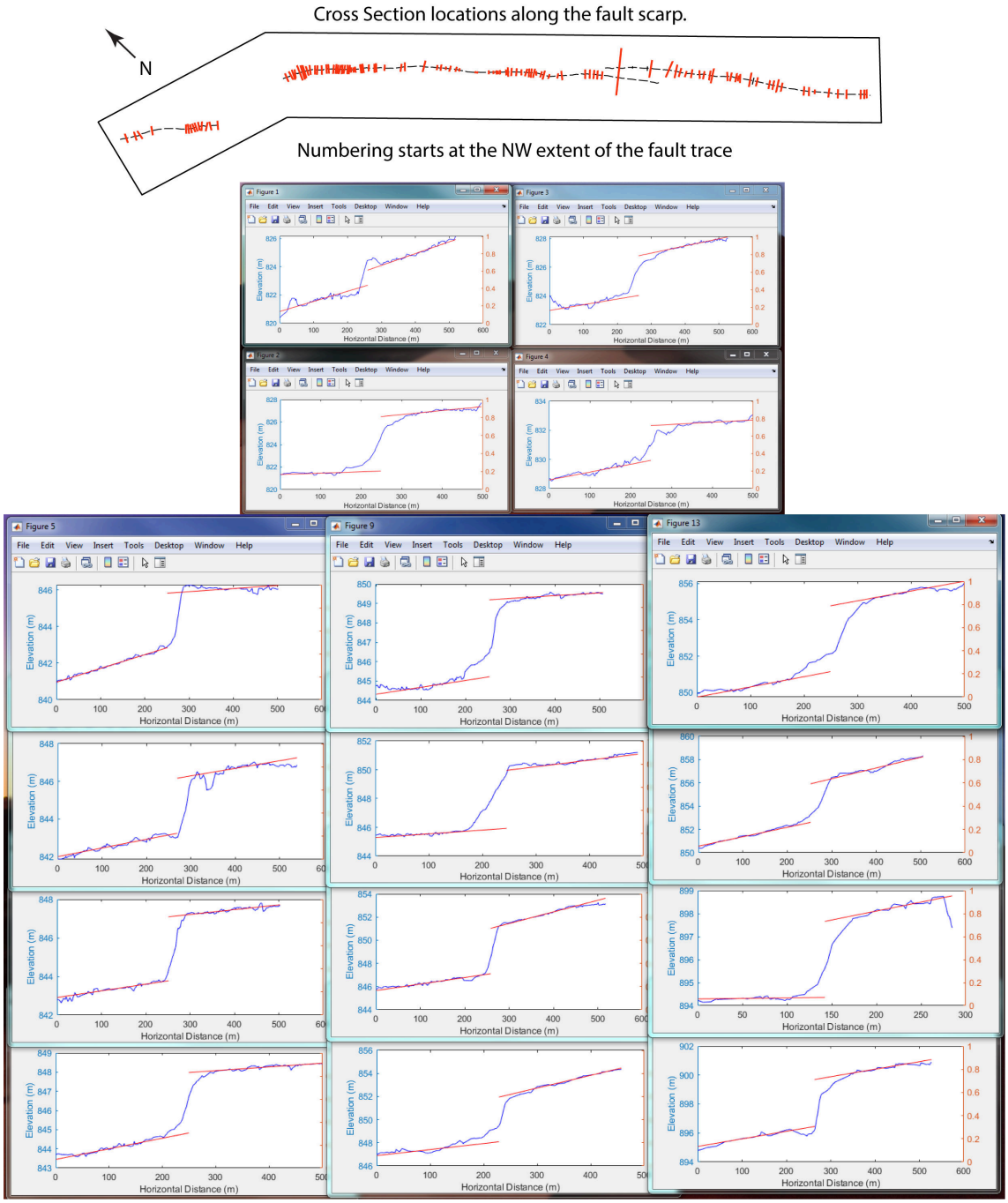

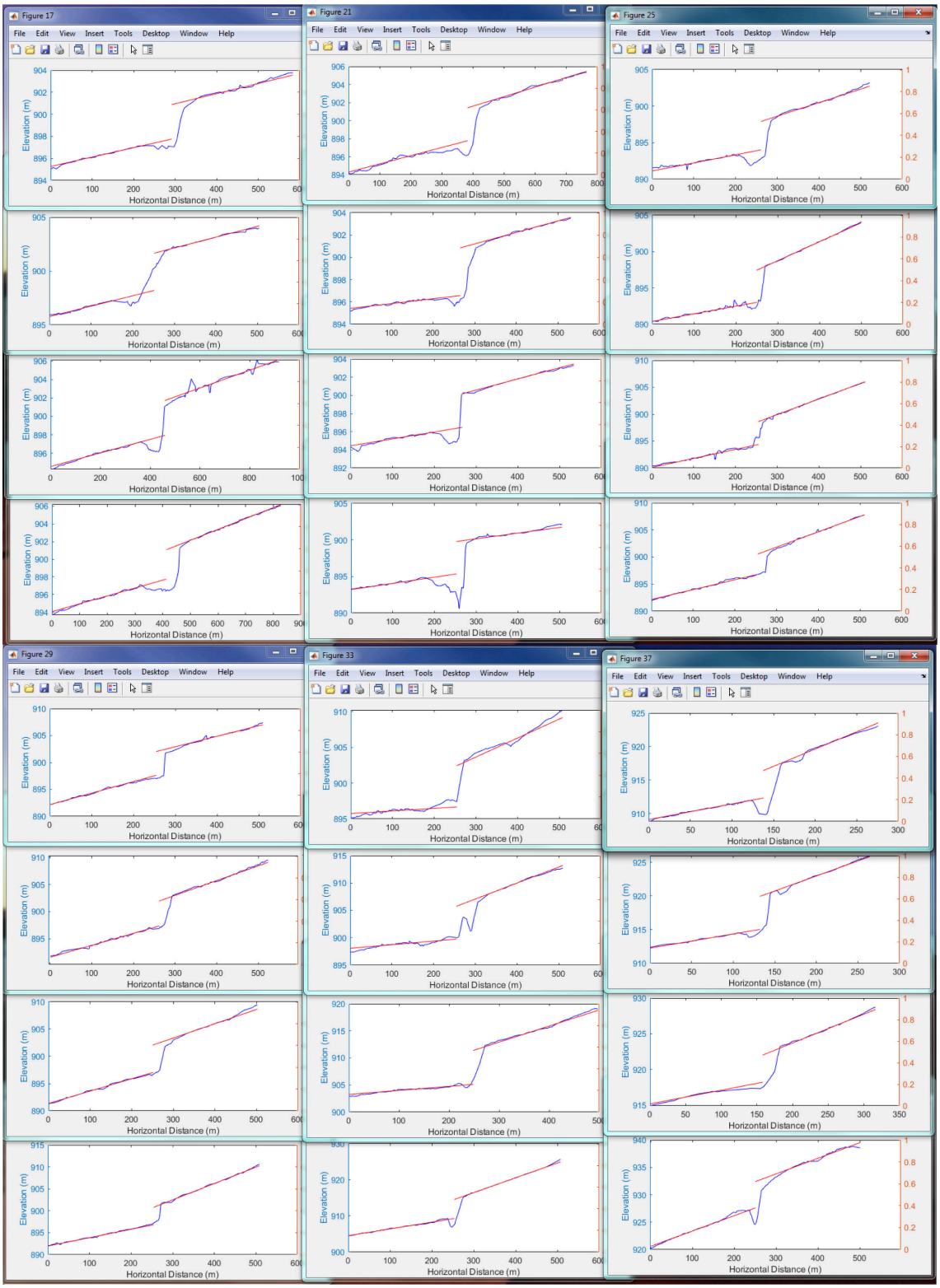
Figure 17
Figure 21
Figure 25
Figure 29
Figure 33
Figure 37
File Edit View Insert Tools Desktop Window Help
Elevation (m)
Horizontal Distance (m)

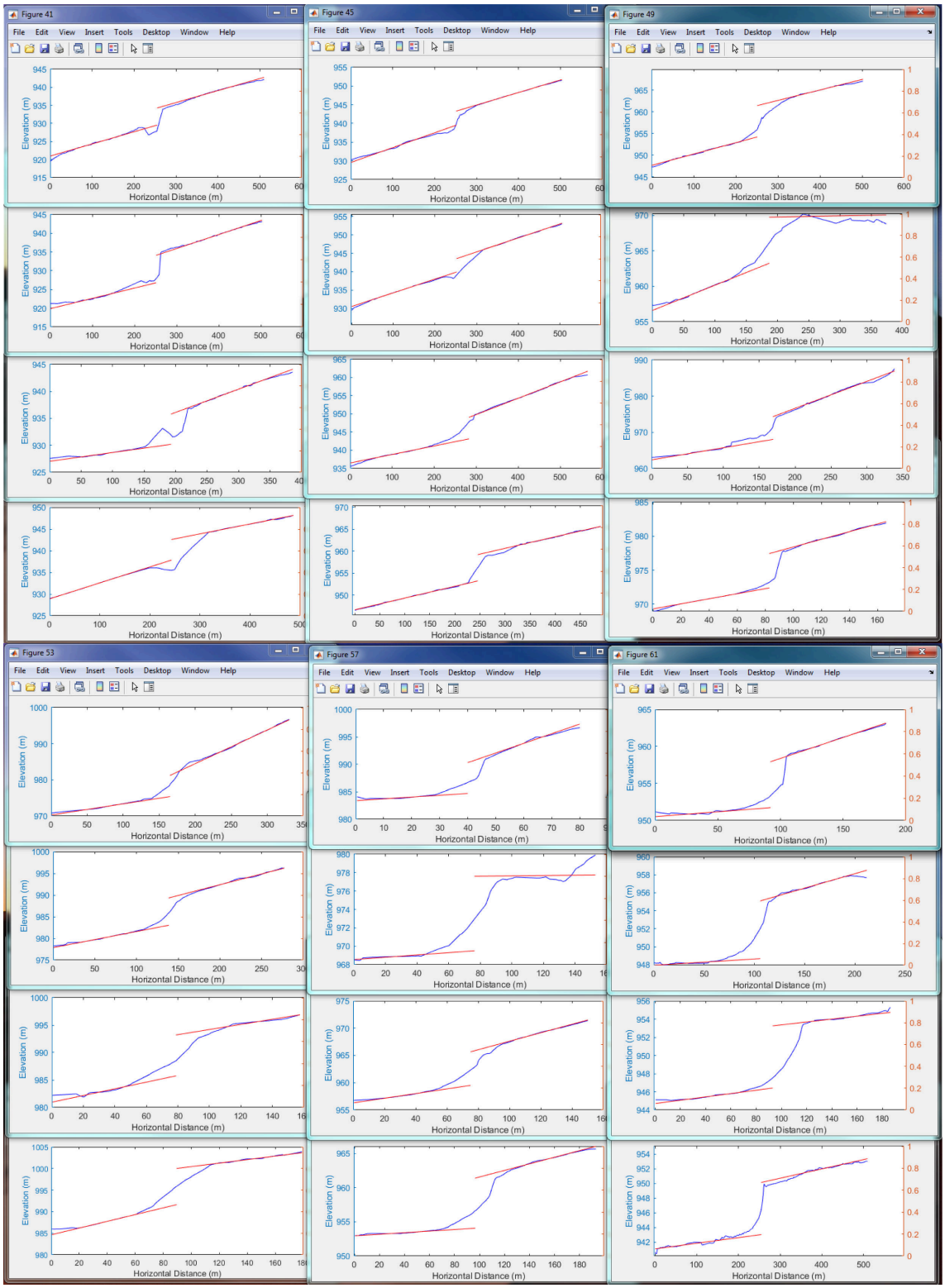
Figure 41
Figure 45
Figure 49
Figure 53
Figure 57
Figure 61
File Edit View Insert Tools Desktop Window Help
Elevation (m)
Horizontal Distance (m)

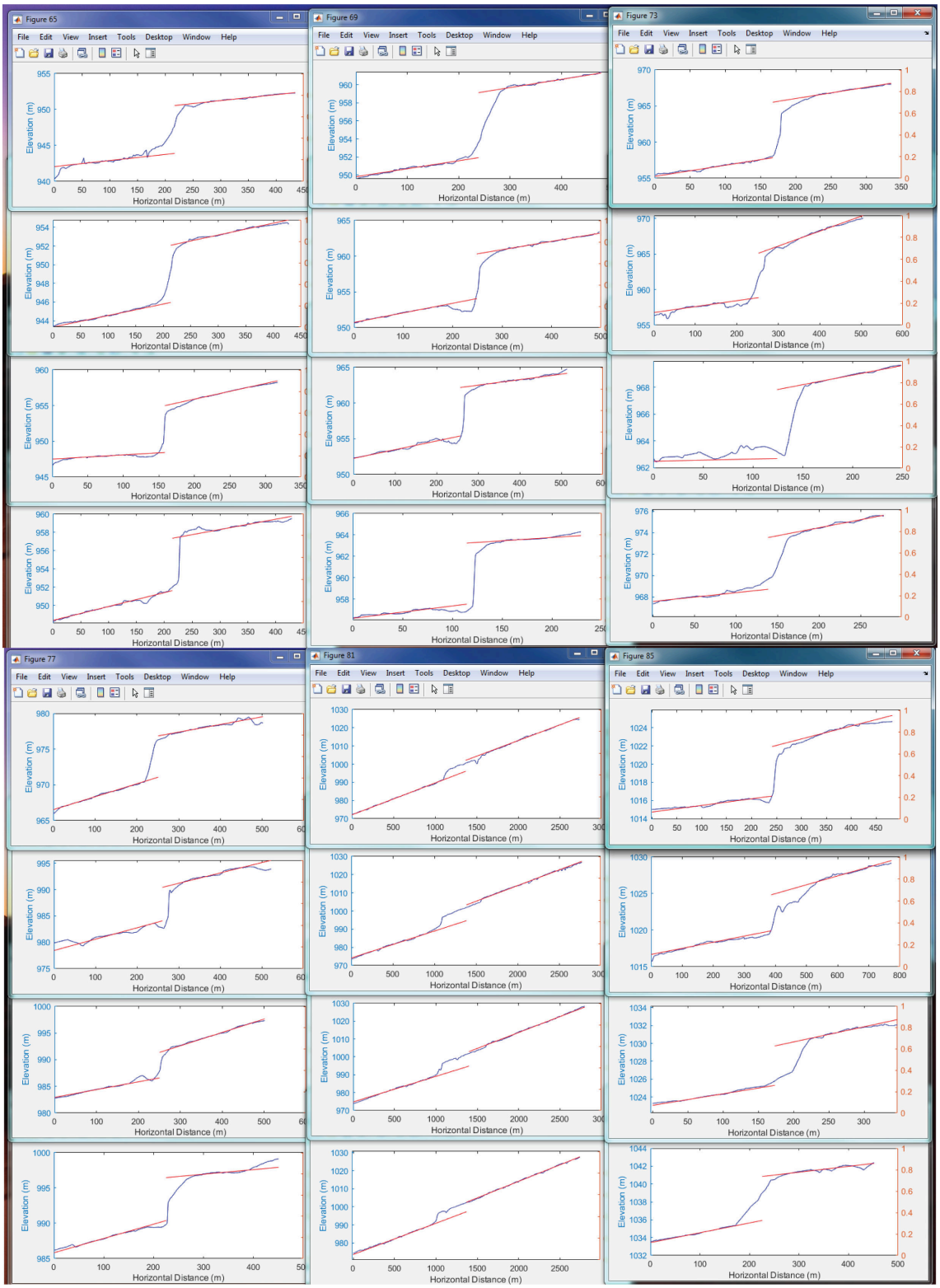
Figure 65
Figure 69
Figure 73
Figure 77
Figure 81
Figure 85
File Edit View Insert Tools Desktop Window Help
Elevation (m)
Horizontal Distance (m)

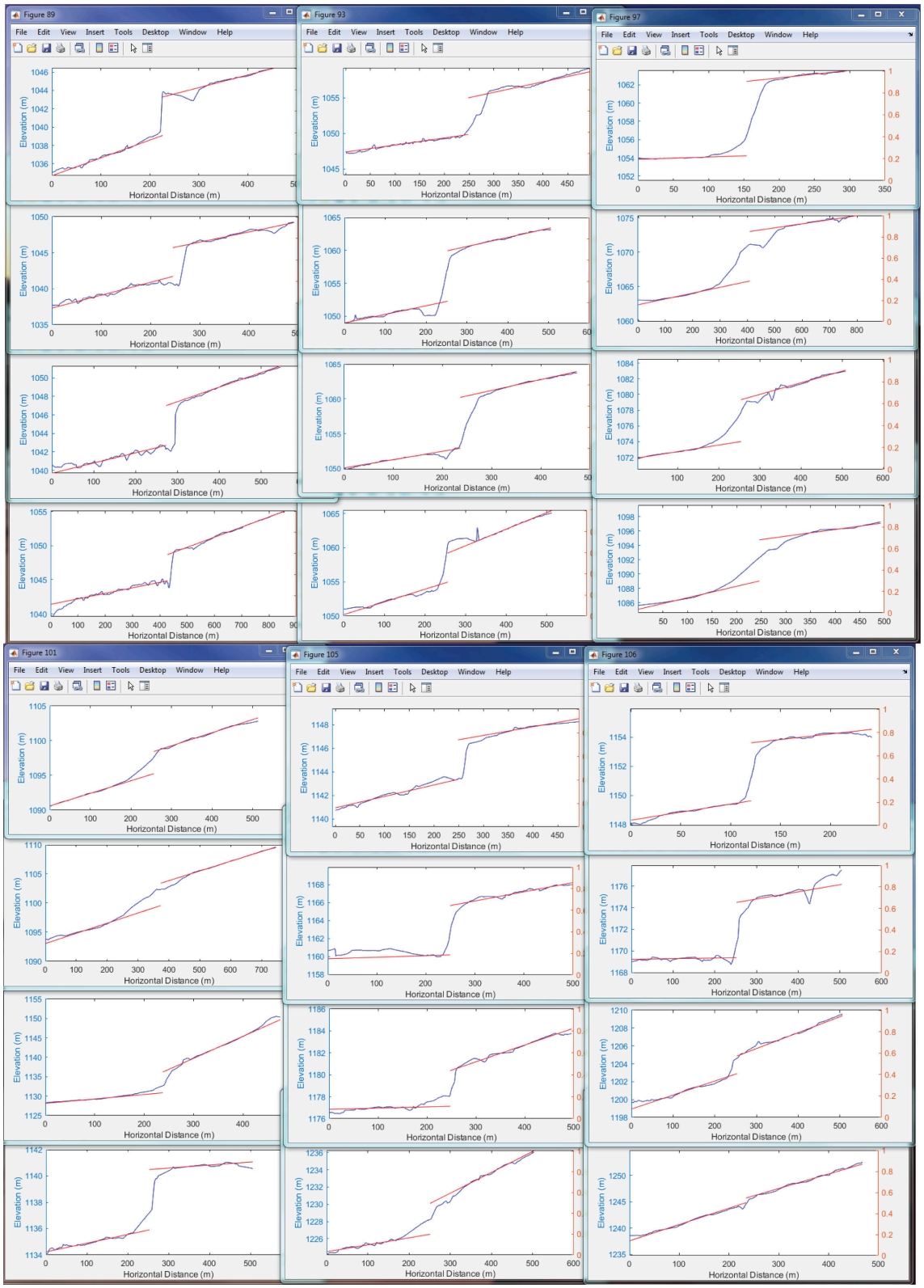
Figure 89
Figure 93
Figure 97
Figure 101
Figure 105
Figure 106
File Edit View Insert Tools Desktop Window Help
Elevation (m)
Horizontal Distance (m)

Compilation of slip-to-length ratios

Table E.1: Compilation of slip-to-length ratios

Name	Location	Tectonic Setting	Type	Length (km)	Slip (m)		Reference
					Max	Mean	
Abant	Turkey	Interplate	RL	40	1.65	0.55	Wells and Coppersmith (1994)
Alasehir Valley	Turkey	Interplate	N	32	0.82	0.54	Wells and Coppersmith (1994)
Almyros	Greece	Interplate	N	5	0.2		Wells and Coppersmith (1994)
Ancash	Peru	Interplate	N	21	3.5		Wells and Coppersmith (1994)
Armenia	USSR	Interplate	R - RL	25	2		Wells and Coppersmith (1994)
Assam	India	SCR	R	110	25		Campbell et al. (2015)
Avezzano	Italy	Interplate	N	20	2		Wells and Coppersmith (1994)
Bhuj	India	SCR	R	30	10		Campbell et al. (2015)
Bingol	Turkey	Interplate	LL	38	0.6	0.25	Wells and Coppersmith (1994)
Bob-Tangol	Iran	Interplate	RL	12	0.3	0.12	Wells and Coppersmith (1994)
Bollnas	Sweden	SCR	N	17		4.35	Stevens (2019)
Bolu	Turkey	Interplate	RL	180	3.6	1.80	Wells and Coppersmith (1994)
Borah Peak	USA, Idaho	Interplate	N - LL	34	2.7	0.80	Wells and Coppersmith (1994)
Borrego Mtn	USA, CA	Interplate	RL	31	0.38	0.18	Wells and Coppersmith (1994)
Brawley	USA, CA	Interplate	RL	10	0.2		Wells and Coppersmith (1994)
Bree	Belgium	SCR	N	10	3	0.50	Vanneste et al. (2001)

Burtrask	Sweden	SCR	N	48		9.61	Stevens (2019)
Burtrask-Bastutrask	Sweden	SCR		60	10		Stewart et al. (2000)
Cadoux	Australia	Interplate	R	15	1.5	0.50	Wells and Coppersmith (1994)
Caldiran	Turkey	Interplate	RL	55	3.5	2.05	Wells and Coppersmith (1994)
Canakkale	Turkey	Interplate	RL	58	4.35	2.10	Wells and Coppersmith (1994)
Cedar Mtn	USA, Nevada	Interplate	RL	61	2		Wells and Coppersmith (1994)
Chalfant Valley	USA, CA	Interplate	RL	16	0.11		Wells and Coppersmith (1994)
Changma	China	Interplate	R - LL	148	4	2.00	Wells and Coppersmith (1994)
Chenoua	Algeria	Interplate	R	4	0.13		Wells and Coppersmith (1994)
Constantine	Algeria	Interplate	LL	4	0.12	0.10	Wells and Coppersmith (1994)
Corinth	Greece	Interplate	N	19	1.5	0.60	Wells and Coppersmith (1994)
Corinth	Greece	Interplate	N	13	1.1	0.60	Wells and Coppersmith (1994)
Coyote Lake	USA, CA	Interplate	RL	14	0.15		Wells and Coppersmith (1994)
Cuzco	Peru	Interplate	N	3	0.1		Wells and Coppersmith (1994)
Damxung	China	Interplate	RL	90	12	8.00	Wells and Coppersmith (1994)
Daofu	China	Interplate	LL	44	1.5		Wells and Coppersmith (1994)
Dasht-e-bayaz	Iran	Interplate	LL	80	5.2	2.30	Wells and Coppersmith (1994)
Dhamer	North Yemen	Interplate	N	15	0.03		Wells and Coppersmith (1994)
Dixie Valley	USA, Nevada	Interplate	RL - N	45	3.8	2.10	Wells and Coppersmith (1994)
Edgecumbe	New Zealand	Interplate	N	18	2.9	1.70	Wells and Coppersmith (1994)
Egiin Davaa	Mongolia	SCR	N	80		8.00	WAL15
El Asnam	Algeria	Interplate	R	31	6.5	1.54	Wells and Coppersmith (1994)

El Centro	USA, CA	Interplate	RL	31	0.8	0.18	Wells and Coppersmith (1994)
Elmore Ranch	USA, CA	Interplate	LL	10	0.23	0.20	Wells and Coppersmith (1994)
Erbaa	Turkey	Interplate	RL - N	47	2	0.66	Wells and Coppersmith (1994)
Erzihean	Turkey	Interplate	RL	360	7.5	1.85	Wells and Coppersmith (1994)
Erzincan	Turkey	Interplate	RL	30	0.2		Wells and Coppersmith (1994)
Eureka Valley	USA, CA	Interplate	N	4	0.02		Wells and Coppersmith (1994)
Fairbiew Peak	USA, Nevada	Interplate	RL - N	57	4.1	2.80	Wells and Coppersmith (1994)
Fort Sage Mtns	USA, CA	Interplate	N	9	0.2		Wells and Coppersmith (1994)
Fort Tejon	USA, CA	Interplate	RL	297	9.4	6.40	Wells and Coppersmith (1994)
Galway Lake	USA, CA	Interplate	RL	7	0.02		Wells and Coppersmith (1994)
Gediz	Turkey	Interplate	N	41	2.8	0.86	Wells and Coppersmith (1994)
Glasgow	New Zealand	Interplate	R - LL	2	0.52		Wells and Coppersmith (1994)
Gobi-Altai	Mongolia	Interplate	LL	236	9.4	6.54	Wells and Coppersmith (1994)
Golbaf	Iran	Interplate	R - RL	15	0.11	0.06	Wells and Coppersmith (1994)
Greenville	USA, CA	Interplate	RL	6	0.03		Wells and Coppersmith (1994)
Haicheng	China	Interplate	LL	6	0.55		Wells and Coppersmith (1994)
Hawkes Bay	New Zealand	Interplate	R - RL	15	4.6		Wells and Coppersmith (1994)
Hayward	USA, CA	Interplate	RL	48	0.9		Wells and Coppersmith (1994)
Hebgen Lake	USA, MT	Interplate	N	27	6.1	2.14	Wells and Coppersmith (1994)

Hebron	Namibia	SCR	N	45	8	4.50	This study
Homestead Valley	USA, CA	Interplate	RL	4	0.1	0.05	Wells and Coppersmith (1994)
Huayta-pallana	Peru	Interplate	R - LL	16	1.2		Wells and Coppersmith (1994)
Imperial Valley	USA, CA	Interplate	RL	60	5.9	1.50	Wells and Coppersmith (1994)
Ipak	Iran	Interplate	R	99	0.8		Wells and Coppersmith (1994)
Ismunden-Lillsjohogen	Sweden	SCR	N	18		4.26	Stevens (2019)
Isovaara-Riikonkumpu	Sweden	SCR	N	49		1.68	Stevens (2019)
Izu-Oki	Japan	Interplate	RL - R	6	0.48		Wells and Coppersmith (1994)
Izu-Oshima	Japan	Interplate	RL	3	1		Wells and Coppersmith (1994)
Kalamata	Greece	Interplate	N	15	0.18	0.15	Wells and Coppersmith (1994)
Kalannie	Australia	SCR	R	1		0.45	Dawson et al. (2008)
Kanatan-ning	Australia	SCR	R	1	0.256	0.22	Dawson et al. (2008)
Kansu	China	Interplate	LL	220	10	7.25	Wells and Coppersmith (1994)
Kastamonu	Turkey	Interplate	RL	280	1.9	0.57	Wells and Coppersmith (1994)
Kehetuohai	China	Interplate	RL	180	14.6	7.38	Wells and Coppersmith (1994)
Kern County	USA, CA	Interplate	R - LL	57	3	0.60	Wells and Coppersmith (1994)
Killari	India	SCR	R	1	0.7		Seeber et al. (1996)
Koli	Iran	Interplate	LL - R	65	3.9	1.20	Wells and Coppersmith (1994)
Kurizan	Iran	Interplate	RL - R	17	1.1		Wells and Coppersmith (1994)
Laikipia	Kenya	Interplate	N	31	3.3		Wells and Coppersmith (1994)
Lainio	Sweden	SCR	N	54		10.30	Stevens (2019)
Lainio-Suijavaara	Sweden	SCR	R	55	30		Stewart et al. (2000)
Laisvall	Sweden	SCR	N	14		4.16	Stevens (2019)

Lancang-Gengma	China	Interplate	RL	35	1.5	0.70	Wells and Coppersmith (1994)
Landers	USA, CA	Interplate	RL	71	6	2.95	Wells and Coppersmith (1994)
Lansjarv	Sweden	SCR	R	50	22		Stewart et al. (2000)
Lansjarv	Sweden	SCR	N	37		6.80	Stevens (2019)
Lansjarv-NS2	Sweden	SCR	N	66		6.33	Stevens (2019)
Lepsy	Kazakhstan	SCR	R - RL	120	14	8.00	Campbell et al. (2015)
Lice	Turkey	Interplate	R	26	0.63	0.50	Wells and Coppersmith (1994)
Lituya Bay	USA, Alaska	Interplate	RL	200	6.6		Wells and Coppersmith (1994)
Luhuo	China	Interplate	LL	89	3.6		Wells and Coppersmith (1994)
Luzon	Phillipines	Interplate	LL	120	6.2		Wells and Coppersmith (1994)
Machaze	Mozambique	SCR	N	35	2		Raucoules et al. (2010)
Managua	Nicaragua	Interplate	LL	6	0.67		Wells and Coppersmith (1994)
Marryat Creek	Australia	Interplate	R - LL	13	1.3	0.50	Wells and Coppersmith (1994)
Meckering	Australia	Interplate	R - RL	36	3.5	0.90	Wells and Coppersmith (1994)
Meers	USA, OK	SCR	LL	32	5.4	3.00	Crone and Luza (1990)
Merasjarvi	Sweden	SCR	N	36		8.81	Stevens (2019)
Merasjarvi-Lainio	Sweden	SCR	N	116		9.07	Stevens (2019)
Mogod	Mongolia	Interplate	RL	40	1.3		Wells and Coppersmith (1994)
Motagua	Guatemala	Interplate	LL	235	3.4	2.60	Wells and Coppersmith (1994)
Mudurna Valley	Turkey	Interplate	RL	80	2.6	1.63	Wells and Coppersmith (1994)
NF1	Sweden	SCR	N	6		1.25	Stevens (2019)
NF2 NF3 NF4	Sweden	SCR	N	20		1.38	Stevens (2019)
Nobi	Japan	Interplate	LL	80	8	5.04	Wells and Coppersmith (1994)

Nordmann-vik	Norway	SCR	N	3	1		Stewart et al. (2000)
North Izu	Japan	Interplate	LL -R	35	3.8	2.90	Wells and Coppersmith (1994)
NS1a NS1b	Sweden	SCR	N	14		2.54	Stevens (2019)
Oroville	USA, CA	Interplate	N - RL	4	0.06		Wells and Coppersmith (1994)
Owens Valley	USA, CA	Interplate	RL - N	108	11	6.00	Wells and Coppersmith (1994)
Paatsikka-joki Palojarvi	Sweden	SCR	N	16		2.77	Stevens (2019)
Papazili	Bulgaria	Interplate	N	50	3.5		Wells and Coppersmith (1994)
Paria-huanca	Peru	Interplate	R	6	0.4		Wells and Coppersmith (1994)
Parkfield	USA, CA	Interplate	RL	39	0.2		Wells and Coppersmith (1994)
Parvie	Sweden	SCR	R	155	15	5.00	Lindblom et al. (2015)
Parvie	Sweden	SCR	R	155	15	5.00	Lindblom et al. (2015)
Parvie1	Sweden	SCR	N	154		5.89	Stevens (2019)
Parvie3	Sweden	SCR	N	74		4.84	Stevens (2019)
Pasinier	Turkey	Interplate	LL - R	12	1.2		Wells and Coppersmith (1994)
Pasmajarvi Ruoko-vaara	Sweden	SCR	N	14		4.68	Stevens (2019)
Pasmajarvi Ruoko-vaara - NF	Sweden	SCR	N	31		3.48	Stevens (2019)
Pirttimys	Sweden	SCR	R	18	2		Stewart et al. (2000)
Pitaycachi	Mexico	Interplate	N	75	4.5	1.90	Wells and Coppersmith (1994)

Pleasant Valley	USA, Nevada	Interplate	N	62	5.8	2.00	Wells and Coppersmith (1994)
Popayan	Colombia	Interplate	SS/ N	1	0.01		Wells and Coppersmith (1994)
Qir-Karzin	Iran	Interplate	R	20	0.1		Wells and Coppersmith (1994)
Rainbow Mountains	USA, Nevada	Interplate	N	18	0.31	0.25	Wells and Coppersmith (1994)
Rikuu-/Senya	Japan	Interplate	R	40	4.4	2.59	Wells and Coppersmith (1994)
Rojnoret	Sweden	SCR	N	64		3.75	Stevens (2019)
Rudbar-Tarom	Iran	Interplate	R - LL	80	0.95		Wells and Coppersmith (1994)
Ruostejarvi	Sweden	SCR	N	4		3.83	Stevens (2019)
Salmas	Iran	Interplate	N - RL	30	6.4		Wells and Coppersmith (1994)
San Fernando	USA, CA	Interplate	R - LL	16	2.5	1.50	Wells and Coppersmith (1994)
San Francisco	USA, CA	Interplate	RL	432	6.1	3.30	Wells and Coppersmith (1994)
San Miguel	Mexico	Interplate	RL -R	22	0.9	0.50	Wells and Coppersmith (1994)
Sevetti	Sweden	SCR	N	12		9.20	Stevens (2019)
Sikano	Japan	Interplate	RL	5	1.5	0.50	Wells and Coppersmith (1994)
Sireh	Iran	Interplate	R - RL	65	0.5	0.16	Wells and Coppersmith (1994)
Sjaunja - NS1c NS1d	Sweden	SCR	N	61		1.86	Stevens (2019)
Skopje	Yugoslavia	Interplate	LL - N	6	0.1		Wells and Coppersmith (1994)
Sorsele	Sweden	SCR	N	56		2.52	Stevens (2019)
South Apennines	Italy	Interplate	N	38	1.15	0.64	Wells and Coppersmith (1994)

Stillwater	USA, Nevada	Interplate	N	34	0.76	0.45	Wells and Coppersmith (1994)
Stouragurra	Norway	SCR	R	80	7		Stewart et al. (2000)
Suasseelka	Finland	SCR	R	48	5		Stewart et al. (2000)
Suasselka	Sweden	SCR	N	76		1.59	Stevens (2019)
Suors-apakka	Sweden	SCR	N	18		2.61	Stevens (2019)
Superstition Hills	USA, CA	Interplate	RL	3	0.05		Wells and Coppersmith (1994)
Superstition Hills	USA, CA	Interplate	RL	27	0.9	0.54	Wells and Coppersmith (1994)
Tabas-e-Golshan	Iran	Interplate	R	85	3	1.50	Wells and Coppersmith (1994)
Tainan	Taiwan	Interplate	RL	12	2.1		Wells and Coppersmith (1994)
Tango	Japan	Interplate	LL - R	14	3		Wells and Coppersmith (1994)
Tangshan	China	Interplate	RL	10	3		Wells and Coppersmith (1994)
Tapti	India	SCR	R	45	14		Copley et al. (2014)
Tennant Creek	Australia	Interplate	R	10	1.3	0.63	Wells and Coppersmith (1994)
Tennant Creek	Australia	Interplate	R	16	1.9	0.93	Wells and Coppersmith (1994)
Tennant Creek	Australia	Interplate	R - LL	7	1.17	0.60	Wells and Coppersmith (1994)
Thessaloniki	Greece	Interplate	N	19	0.22	0.08	Wells and Coppersmith (1994)
Tonghai	China	Interplate	RL	48	2.7	2.10	Wells and Coppersmith (1994)
Ungava	Canada	SCR	R	10	2	0.80	Wells and Coppersmith (1994)
Ustukran	Turkey	Interplate	RL	9	0.3		Wells and Coppersmith (1994)
Vaalajarvi	Sweden	SCR	N	8		2.28	Stevens (2019)
Varto	Turkey	Interplate	RL	30	0.4	0.15	Wells and Coppersmith (1994)
Venejarvi	Sweden	SCR	N	18		4.52	Stevens (2019)
Wuqai	China	Interplate	R	15	1.55		Wells and Coppersmith (1994)

Yuli-Juisu	Taiwan	Interplate	LL - R	43	2.1	Wells and Coppersmith (1994)